In-cell NMR Spectroscopy in Mammalian Cells

Inaugural-Dissertation
to obtain the academic degree
Doctor rerum naturalium (Dr. rer. nat.)

Submitted to the Department of Biology, Chemistry and Pharmacy
of Freie Universität Berlin

by

Beata Bekei
from Budapest, Hungary

03. 2013

07.2008 – 03.2013

Leibniz-Institut für Molekulare Pharmakologie

Dr. Philipp Selenko, In-cell NMR research group

1st Reviewer: Professor Hartmut Oschkinat

2nd Reviewer: Professor Dr. Erich Wanker

Date of defence:
26.09.2013

Summary

The significance of *in vivo* protein studies is widely appreciated. Whereas *in vivo* protein behaviors inside cells are influenced by many unique physical parameters such as macromolecular crowding and intracellular viscosity, they are also affected by a plethora of biological activities[1-3] that often vary greatly in different cell types. *In-cell* NMR spectroscopy is an invaluable biophysical tool for residue-specific, structural and functional investigations of isotope-labeled proteins inside native environments of cells[4] and, as such, a preferred tool for studying intracellular proteins behaviors. Despite the great potential of *in-cell* NMR applications, the method is most commonly used for prokaryotic *in-cell* NMR measurements in *E.coli* cells[5-7], while *in-cell* NMR studies in eukaryotic cells are have been limited by the sparse availability of suitable cellular model systems[8-10].

The primary goal of this thesis was to extend the general applicability of eukaryotic *in-cell* NMR measurements to also include mammalian cells and to develop a generic protocol for the efficient delivery of isotope-labeled proteins into mammalian cells. In 2009, hence in the course of this project, two protein transduction techniques, the application of cell penetrating peptide (CPP)[11] carriers for intracellular protein delivery, and of protein transduction methods via action of pore-forming bacterial toxins such as Streptolysin O (SLO)[12, 13] had been reported for *in-cell* NMR experiments in mammalian cells. While these two methods were being reported, I had already performed a great deal of comparative studies to evaluate the individual advantages and disadvantages of both techniques. These are described in the first parts of the thesis. In parallel, I had developed an entirely novel approach to deliver proteins in mammalian cells for *in-cell* NMR purposes: protein electroporation (EP). This method proved to be superior to CPP-, and toxin-mediate delivery protocols, as outlined in the first half of the thesis. Transduction efficiencies, cell viabilities and intracellular distributions of two model proteins, human alpha Synuclein (αSyn) and the B1 domain of Protein G (GB1) were comparatively analyzed in different mammalian cell types and found to be generally higher using the EP-mediated delivery approach.

Results demonstrate that low transduction efficiencies, high cell line dependences and vesicular-like intracellular distributions strongly limited the suitability

of CPP-mediated protein delivery attempts. Although SLO- and EP-procedures yielded comparable transduction efficiencies at low applied protein concentrations, EP clearly outperformed the SLO approach at higher protein concentrations, because it enabled the linear delivery of increasing concentrations of exogenous proteins, with high correlations in intracellular cellular protein levels.

In the second part of the thesis, I provide a first time description of the structural, dynamic and functional details of a human amyloid protein, αSyn and its isoforms beta- and gamma-synuclein inside different mammalian cells, as determined by high-resolution *in-cell* NMR experiments. αSyn, a small (14.5 kDa) intrinsically disordered neuronal protein is known to accumulate into cytosolic filamentous inclusions of dopaminergic neuronal cells[14] in the course of neurodegenerative disorders termed synucleinopathies[15]. High-resolution *in-cell* NMR studies were performed to provide novel insights into the native *in vivo* properties of this protein, especially in relation to its physiological and pathological properties, such as intracellular aggregation[16, 17], membrane association[18] and post-translation modification[19]. The choice of mammalian cells models included disease-unrelated (i.e. HeLa and A2780 cells) and disease-related dopaminergic neuronal cell lines (i.e. B65 and SK-N-SH cells). Because dopaminergic neurons of the *substantia nigra* (SN) are particularly affected in Parkinson's disease patients[20], a SN-derived rat cell line, i.e. RCSN3 cells[21] was additionally employed in this study.

I verified the suitability of EP routines to deliver isotope-labeled α-, β-, γSyn into cultured mammalian cells. Despite low effective NMR concentrations in the physiological range of αSyn (3.5-12 μM), rendering these *in-cell* NMR experiments highly technically challenging, *in-cell* NMR data were of excellent quality and enabled me to derive residue-resolved structural and biochemical information about this protein and its two isoforms. High-resolution 2D ^{1}H-^{15}N SOFAST-HMQC spectra of the Synuclein protein family revealed monomeric appearances in five different mammalian cell lines, with no indications for significant conformational change, such as amphipatic helical conversions[18], or aggregations into beta-sheet rich, high molecular weight oligomers, or amyloid fibrils[22, 23]. Despite their disordered and monomeric characteristics, similar but not identical site-selective line broadening effects were observed, which affected the first ten N-terminal residues in α-, as well as β-, and

γSyn. In addition to these, high degrees of site-selective line broadening of the N-terminus of αSyn, residue-resolved 2D T2 relaxation measurements indicated very fast relaxation behaviors of residues 30 to 45 and 118 to 130. Interestingly, no changes in relaxation properties were detected for the rather hydrophobic and aggregation prone NAC region of αSyn, with the exception of residues 93-95 that were specifically affected in RCSN3 cells only. The majority of these broadened signals were recovered in cell extract samples after lysis, with the exception of the *substantia nigra*-derived RCSN3 cell model. In this cell line, several protein peaks remained highly broadened even after lysis, which suggested that specific and/or unspecific but highly cell type-selective interactions are present in these cells. N-terminal acetylation, a constitutive post-translational modification in mammals, was uniformly detected in αSyn and its isoforms[24] in all tested cell lines. Phosphorylation of Ser129 of αSyn phosphorylation was observed at very low levels in Western blotting, but not by *in-cell* NMR measurements[25, 26]. A tight regulation of the phosphorylation status of αSyn was further revealed in PLK3 kinase over-expressing cells and cell lysates.

In conclusion, in this thesis I established a novel technique for the delivery of isotope-labeled proteins such as αSyn into mammalian cells, for the purpose of enabling advanced *in-cell* NMR studies in cells of higher organisms. αSyn NMR data obtained in cultured neurons and other cell types demonstrated that this protein, and its two isoforms remained intrinsically disordered and monomeric in all tested cell types. The excellent spectral qualities of synuclein *in-cell* NMR specimens obtained under healthy physiological conditions, hold great promises for future *in-cell* NMR studies under pathogenic conditions related to Parkinson's disease and the development of cell-based *in-cell* NMR models for investigating the intracellular aggregation behaviors of this-, and other proteins[27-29].

Zusammenfassung

Die Wichtigkeit von *in vivo* Studien wird weithin hoch eingeschätzt. Während das Verhalten der Proteine innerhalb der Zellen durch viele einzigartige physische Parameter wie makromolekulare Häufung und intrazellulare Zähflüssigkeit beeinflusst wird, wird es auch von einer großen Zahl von biologischen Aktivitäten[1-3] beeinträchtigt, die oft sehr zwischen Zelltypen variieren. Intrazellulare NMR Spektroskopie ist ein sehr wertvolles biophysisches Rückstand- spezifisches Tool für strukturale und funktionale Untersuchungen von Isotop-markierten Proteinen in der ursprünglichen Umgebung der Zellen[4] und damit ein bevorzugtes Werkzeug für die Untersuchung der intrazellulären Verhaltensweisen der Proteine. Trotz der potentiell großen Einsatzmöglichkeiten von *in-cell* NMR wird die Methode hauptsächlich für prokaryotische *in-cell* NMR-Messungen in E.coli-Zellen[5-7] benutzt. Allerdings sind die Möglichkeiten von *in-cell* NMR-Messungen in eukaryotischen Zellen wegen der wenigen verfügbaren geeigneten Zellmodell-Systeme begrenzt[8-10]

Als Primärziel meiner These wollte ich die Einsetzbarkeit der eukariotischen *in-cell* NMR-Messungen auf die Säugetier-Zellen erweitern und ein Generisches Protokoll für die effiziente Lieferung Isotop-markierter Proteine in die Säugetier-Zellen entwickeln. Im Jahr 2009 wurden zwei Proteintransduktionsmethoden für *in-cell* NMR-Untersuchungen in Säugetier-Zellen veröffentlicht: die Verwendung von Zellpenetrierenden Peptid-Trägern für intrazelluläre Proteinlieferung (CPP)[11] und Proteintransduktion durch Poren bildende bakterielle Toxine: Streptolysin O (SLO)[12, 13]. In der Zwischenzeit habe ich viele Vergleichsstudien durchgeführt, die die Vorteile und Nachteile dieser, im ersten Teil meiner Doktorarbeit dargestellten Methoden evaluieren. Nun habe ich einen neuartigen Ansatz für Proteinlieferung in die Säugetier-Zellen entwickelt: die Protein-Elektroporation (EP). Diese Methode erwies sich als den in der ersten Hälfte der These beschriebenen CPP- und Toxin-vermittelten Lieferungsprotokollen überlegen. Die Transduktionseffizienz, Zelllebensfähgkeit und intrazelluläre Verteilung der zwei Modellproteine des menschlichen alpha Synuclein (αSyn) und der B1-Domäne des Protein G (GB1) wurden in verschiedenen Säugetier-Zellen analysiert und erwiesen sich im Allgemeinen als höher, wenn der EP- vermittelte

Lieferansatz gewählt wurde.

Die Ergebnisse zeigen, dass niedrige Transduktionseffizienzen, hohe Zelllinienabhängigkeiten und vesikular-ähnliche intrazelluläre Verteilungen die Anwendbarkeit von CPP-vermittelten Proteinlieferversuchen stark einschränken. Obwohl SLO- und EP- Prozeduren vergleichbare Transduktionseffizienzen bei niedrigen Proteinkonzentrationen ergaben, war die EP- Methode bei höheren Proteinkonzentrationen eindeutig besser als der SLO- Ansatz, weil sie die lineare Lieferung vom immer höheren Konzentrationen von exogenen Proteinen ermöglichte, und dies bei hohen Korrelationen in intrazellularen Proteinniveaus.

Im zweiten Teil der These liefere ich eine erstmalige Beschreibung der strukturellen, dynamischen und funktionellen Details eines humanen Amyloidproteins, αSyn, und seiner Isoformen Beta- und Gamma-Synuklein in verschiedenen Säugetier-Zellen, so wie sie durch hochresolutions *in-cell* NMR-Experimente festgestellt werden. αSyn, ein kleines (14.5 kDa) intrinsisch desorganisiertes neuronales Protein ist dafür bekannt, dass es sich im Verlaufe von Synukleinpathie[14] genannten neurodegenerativen Krankheiten in zytosolische, filamentöse Inklusionen dopaminergischer Neuronenzellen[15] sammelt. Hochresolutions *in cell* NMR-Studien wurden durchgeführt, um neue Einsichten in die angeborenen *in vivo* Eigenschaften dieses Proteins zu erlauben, insbesondere mit Hinblick auf seine physiologischen und pathologischen Eigenschaften, so wie intrazellulare Aggregation[16, 17], membrane Assoziation[18] und Post-translations Veränderungen[19]. Die Auswahl von Säugetier-Zell-modellen umfasste sowohl Krankheitsunberührte (i.e. HeLA und A2780-Zellen) als auch Krankheitsberührte dopaminergische neuronale Zelllinien (i.e. B65 und SK-N-SH-Zellen). Weil dopaminergische Neuronen der *substantia nigra* (SN) in Parkinsonpatienten besonders betroffen sind[20], wurde eine SN-abgeleitete Rattenzelllinie, i.e. RCSN3-Zellen[21], zusätzlich in diese Studie aufgenommen.

Ich habe die Anwendbarkeit der EP-Routinen für die Lieferung Isotop-markierter α-, β- und γSyn in Säugetier-Zellen-kulturen überprüft. Trotz niedriger effektiver NMR-Konzentrationen im physiologischen Spektrum von αSyn (3.5-12 μM), was diese intrazellularen NMR-Experimente zu einer hohen technischen Herausforderung machte, waren die intrazellularen NMR-Daten von hervorragender Qualität und erlaubten mir die

Ableitung von Residuum-geklärten strukturellen und biochemischen Informationen über dieses Protein und seine zwei Isoformen.

Hochresolutions 2D ^{1}H-^{15}N SOFAST-HMQC-Spektren der Synukleinproteinfamlie zeigten monomerische Erscheinungen in fünf verschiedenen Säugetier-Zell-linien, mit keinerlei Anzeichen bedeutender konformationeller Veränderung, wie z.B. amphobatische helikale Konversionen[18] oder Aggregationen in Beta-Blatt-reiche, hochmolekulargewichtige Oligomere oder Amyloidfibrile[22, 23]. Trotz ihrer desorganisierten und monomerischen Charakteristika wurden ähnliche aber nicht identische ortsspezische Erweiterungseffekte beobachtet, die die ersten zehn N-Terminalresiduen in α- als auch β- und γSyn betrafen. Außer dieser in hohem Grade ortsspezifischen Linienerweiterung des N-Terminus des αSyns zeigten Residuum-geklärte 2D T2-entspannte Messungen sehr schnelle Entspannungsverhalten der Residuen 30 bis 45 und 118 bis 130. Interessanterweise wurden keine Veränderungen in den Entspannungseigenschaften der eher hydrophoben und Sammlungsgeneigten NAC-Region des αSyns entdeckt, mit Ausnahme der Residuen 93-95, die nur in den RCSN3-Zellen spezifisch betroffen waren. Die Mehrzahl dieser erweiterten Signale wurde in Zellextraktstichproben nach *lysis* zurück gewonnen, mit Ausnahme des *substantia nigra*-abgeleiteten RCSN3-Modells. In dieser Zelllinie blieben einige Proteinspitzen sogar nach *lysis* stark erweitert, was nahe legt, dass spezifische oder unspezifische, aber hochgradig Zelltypbedingte Interaktionen in diesen Zellen stattfinden. N-Terminal Acetylation, eine konstitutive Post-Translationale Veränderung in Säugetieren wurde überall in αSyn und seinen Isoformen in allen getesteten Zelllinien entdeckt. Phosphorylation der Ser129 einer αSyn-Phosphorylation wurde in sehr geringem Ausmaß in Western blotting, aber nicht in intrazellularen NMR-Messungen entdeckt[25, 26]. Eine strenge Regulierung des Phosphorisierungsstatus der αSyn wurde des Weiteren in PLK-Kinäse-überexpressiven Zellen und Zelllysaten entdeckt.

Zusammenfassend kann man sagen, dass ich in dieser These eine neue Technik für die Lieferung Isotop-gekennzeichneter Proteine so wie αSyn in Säugetier-Zelle etabliere, zum Zweck der Durchführung fortgeschrittener *in cell* NMR-Studien in Zellen höherer Organismen. Die αSyn- NMR-Daten, die in Neuronenkulturen und anderen Zelltypen gewonnen wurden, zeigen, dass dieses Protein und seine beiden Isoformen in allen getesteten Zelltypen intrinsisch desorganisiert und monomerisch blieben. Die

ausgezeichneten spektralen Qualitäten der Synuklein- *in cell* NMR-Stichproben, die unter gesunden physiologischen Bedingungen erhalten wurden, zeigen hohes Potential für zukünftige intrazellulare NMR-Studien unter pathogenischen Bedingungen wie bei der Parkinsonschen Krankheit und die Entwicklung Zellbasierter, intrazellularer NMR-Modelle zur Untersuchung des Aggregationsverhaltens dieser und anderer Proteine[27-29].

1. Introduction

1.1 *In-cell* NMR spectroscopy

In-cell NMR spectroscopy is a relatively new application of solution state NMR spectroscopy that provides atomic resolution information about the structural and dynamic properties of proteins inside live cells[4, 30] and, therefore, within a highly crowded, viscous and complex, but physiologically relevant biological environment ***(Figure 1)***[31, 32]. *In-cell* NMR experiments require isotope labeling of proteins that are to be detected in the unlabeled environment of these cells and a dedicated delivery method to target these isotope-labeled proteins into the cells that are to be studied. Isotope labeling is typically achieved during recombinant protein production in prokaryotic expression hosts such as *E.coli*[33, 34], which offers the additional advantage that proteins are being made in a 'naked' form, without any post-translational protein modifications that typically decorate all polypeptides in higher eukaryotic cellular environments. Once delivered into a eukaryotic cell, these post-translational protein modifications, such as phosphorylation, acetylation, glycosylation etc. are rapidly established by endogenous cellular enzymes, which can be directly followed by time-resolved *in-cell* NMR experiments[35-38].

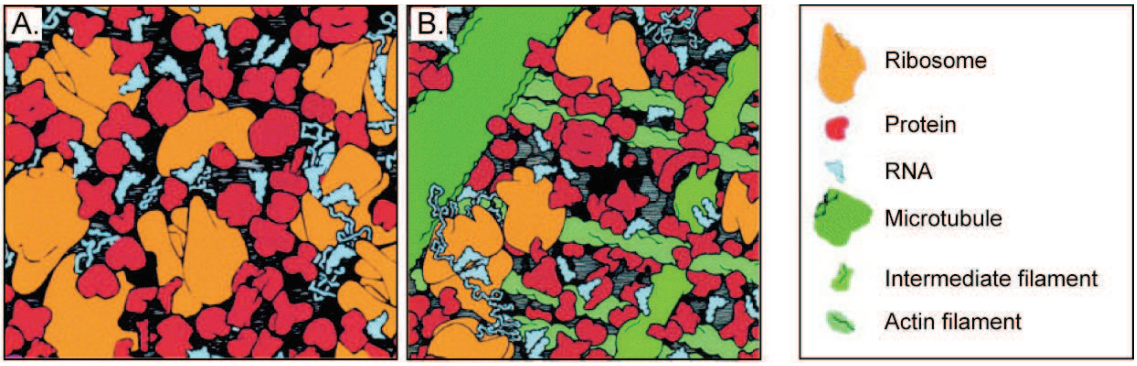

Figure 1: Illustration of the highly complex intracellular environment of prokaryotes (A) and eukaryotes (B). Reproduced from [39].

Three factors typically determine the applicability of *in-cell* NMR methods: First, relatively high concentrations of the isotope-labeled proteins need to be present inside the cells that are to be studied[40]. Second, these cells ought to be viable during the course of the *in-cell* NMR measurements and, third, there must not be any leakage of protein out of these cells[41, 42].

To date, only a few methods for delivering isotope-labeled proteins into eukaryotic cells are available. Protein delivery into *Xenopus laevis* oocytes by microinjection has been the first technique to successfully generate a eukaryotic *in-cell* NMR sample. Microinjection provides several advantages, such as high reproducibility, well-defined injection concentrations, absence of background signals and the fact that injection can be automated for rapid delivery procedures. However, protein delivery by microinjection is limited to large cells, with intracellular volumes in the µl range, such as *Xenopus laevis* oocytes[9, 43, 44]. About, 100-200 injected oocytes are needed for one *in-cell* NMR sample ***(Figure 2)***. In other eukaryotic cellular model systems, such as mammalian cells, sample preparation by microinjection is technically impracticable because millions of cells would need to be manipulated. For the preparation of mammalian *in-cell* NMR samples, a different protein delivery method ought to be available that targets millions of cells in parallel, ensures high reproducibility, high intracellular sample deposition and high cell viability. To date, two protein transduction techniques for the generation of mammalian *in-cell* NMR samples have been described[11, 12] (***Figure 2***). I introduce them in the following chapter.

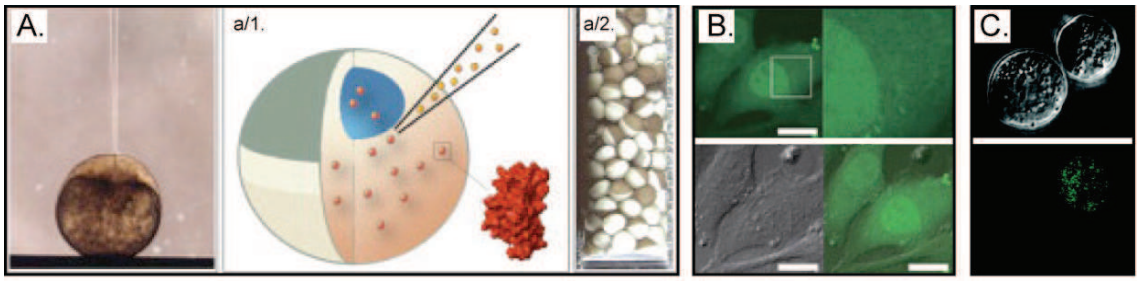

Figure 2: Eukaryotic *in-cell* NMR samples.
A) Protein delivery into *Xenopus laevis* oocytes by microinjection. **a/1)** Schematic depiction of the oocyte injection process. The isotope-labeled protein is shown in red. **a/2**) Injected oocytes are collected in the NMR tube for *in-cell* NMR measurements. Reproduced from [43]. **B)** Cell Penetrating Peptide-mediated protein delivery. Microscopy of transduced and Alexa488-labeled Ub-3A-Tat protein in HeLa cells. Reproduced from [11]. **C)** Streptolysin O-mediated protein delivery of FITC-labeled Tβ4 protein into 293F cells. Reproduced from [12].

1.2 Delivery techniques for mammalian *in-cell* NMR

1.2.1 Cell Penetrating Peptide (CPP) - mediated protein delivery

Intracellular protein delivery for the generation of mammalian *in-cell* NMR samples by action of *Cell Penetrating Peptide*s (CPPs) has been introduced in 2009 by Inomata *et al.*[11].

CPPs (10 to 30 amino acids) are derived from viral, insect or mammalian proteins[45, 46] that are often highly positively-charged and lysine/arginine rich. Polyarginine (R8)[47, 48], the Tat peptide[49], penetratin[50], pVEC[51], VP22[52] are the most well-studied and commonly used CPPs. Not only do they have the capacity to translocate through the plasma membrane, but also to act as carrier moieties onto which cargo molecules can be attached that are then 'delivered' into cells. Therefore, CPPs are widely used for the intracellular transport of a variety of cargos, such as proteins, peptides, oligonucleotides, siRNAs or drugs[53-55]. CPP-mediated cargo delivery occurs in three main steps: First, binding of the CPP-moiety to the plasma membrane. Second, entry of the CPP-cargo construct into cells. Third, release of the CPP-cargo construct in the cytoplasm. In addition, intracellular separation of the CPP-moiety from the cargo-protein is often desired.

Although several internalization pathways for CPP-cargo constructs have been suggested[56-61] the exact uptake mechanism(s) is still under debate. For low molecular weight cargos, direct translocation through the plasma membrane and/or endocytosis routes have been discussed, whereas high molecular weight cargos are thought to be internalized via a dedicated endocytosis pathway termed macropinocytosis[58, 62]. Often, CPP translocation properties additionally depend on temperature[63] and the local concentrations of the penetrating peptides[64, 65]. Some reports suggest that CPPs enter cells via mechanisms that are similar to retrograde delivery processes such as the ones that bacterial toxins use to enter cells. These transport mechanisms may involve the Golgi apparatus and the ER, and include a final release step into the cytosol[66]. However, for cationic CPPs, the prevalent notion suggests that endocytosis pathways initiate by the association of CPPs with extracellular membranes, specifically through electrostatic interactions with negatively-charged cell surface glycosaminoglycans[57, 67-69]. It is further thought that many of the uncertainties in the field arise due to microscopy artifacts that may result from different cell fixation routines[70]. To promote the release of CPP-cargo constructs from endosomal transport vesicles, a number of approaches have been described ***(Table 1)***.

Because CPPs have strong tendencies to interact with biological membranes[11], intracellular separation of CPP and protein moieties is strongly desired as unspecific lipid-binding strongly distorts the physiological relevance of experimental outcomes[59]. To avoid this, endosomal or cytoplasmic CPP cleavage reactions by proteolytic cellular enzymes are often employed (***Table 1***). Other means to ensure cytoplasmic removal of

CPP moieties are to use covalent *in vitro* coupling reactions to fuse CPPs onto cargos via oxidative disulfide linkers[11]. Such chemical linkages are readily reduced in the intracellular environments of live cells, which results in the separation of the CPP-, from the protein cargo-moiety. As another advantage, CPPs that are to be coupled via such procedures can be produced in large quantities by solid-phase peptide synthesis (SPPS). Chemical synthesis enables further additions of fluorescence labels, or affinity purification tags.

Function	Molecule	Mechanism	Reference
Facilitate CPP uptake	Saponin	Plant toxin. A monomeric ribosome-inactivating protein that promotes internalization.	*48*
	Pyrenebutyrate	Negatively charged counter-anion with high hydrophobicity. Induces direct translocation through the cell membrane.	*71*
Endosomal cleavage	Cathepsin B site	Member of the peptidase PI family. Lysosomal cysteine protease. Acts as both endopeptidase and carboxypeptidase.	*72*
	Pro-protein convertase eg: Furin site	Furin is a calcium-dependent serin endoprotease. It cleaves at paired basic amino acid processing sites. Furin is found enriched in the Golgi apparatus, endosomes and plasma membrane.	*73*
Endosomal release	Melittin	Bee venom. Spontaneously integrates into lipid membranes.	*74*
	N-terminus of the influenza virus hemagglutinin protein (HA-tag)	pH sensitive fusogenic peptide, that destabilizes lipid membranes at low pH	*75*
	Diptheria Toxin T-domain (DT-tag)	Diphtheria toxin T domain translocates the catalytic C domain across endosomal membranes in response to acidification.	*76*
	Chloroquine	Lysosomotropic agent. Accumulates in protonated forms in endocytic compartments, where it acts against the endosomal proton pump and induces lysis.	*77*
Cytoplasmic cleavage	Endogenous ubiquitin-specific C-terminal protease	Ubiquitin-specific C-terminal protease	*11*
	Disulfide bound reduction	Automatic intracellular reduction, mainly by glutathione	

Table 1: Addition to CPP-mediated protein delivery tools.

A well-known CPP, derived from the HIV-1 virus, Tat-HIV (residues 47-YGRKKRRQRRR-57) was exploited to deliver a ^{15}N isotope-labeled ubiquitin derivative and the protein G B1 domain into HeLa cells for the purpose of generating the first *in-cell* NMR sample in human cells[11], which entails incubation of the targeted cells with the CPP-cargo construct[78] ***(Figure 3)***.

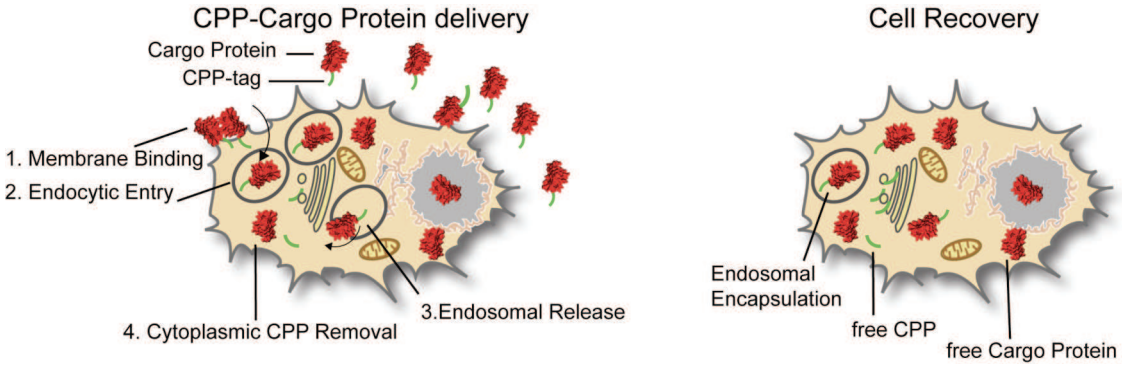

Figure 3: CPP-mediated protein delivery
In-cell NMR sample preparation routine via the CPP-mediated protein delivery approach.

CPP-mediated protein delivery approaches have to overcome three experimental obstacles. First, the uptake efficiencies of CPP-cargo constructs are highly dependent on the choice of the CPP sequence and on the combination of CPP/cargo proteins. Membrane compositions of targeted host cells additionally affect the individual uptake efficiencies[79-81] and these properties need to be considered when devising a CPP-mediated delivery experiment. Second, even if optimal combinations of CPP/cargo sequences have been found for a particular cell line that is to be targeted, efficient release from endocytotic vesicles has to be achieved[75]. For *in-cell* NMR measurements that aim at studying the cytoplasmic properties of an intracellular protein, entrapment in endosomal vesicles must be avoided and cytoplasmic release should be quantitatively accomplished. Third, cytoplasmic separation of the CPP- and cargo-moieties should be achieved in a straightforward manner. Engineered proteolytic cleavage sites may however affect the structural properties of the resulting non-native proteins and lead to artifacts.

1.2.2 Streptolysin O (SLO) - mediated protein delivery

An alternative approach for intracellular protein delivery has recently been suggested for the generation of mammalian *in-cell* NMR samples by means of pore-forming toxins (PFTs)[12]. Although bacterial PFTs are the best studied and characterized cytolytic toxins [82, 83], pore forming toxins are also produced in a variety of poisonous species, such as insects[84], reptiles[85] and marine invertebrates[86]. PFT mediated protein delivery exploits the cell permeating properties of protein/peptide toxins that are secreted by the pathogen[87]. These toxins associate with plasma-membranes of targeted host cells, generally via specific transmembrane receptors, to form non-selective transmembrane pores that contain a hydrophilic inner- and a hydrophobic outer-surface[88]. These pores are used to deliver isotope-labeled proteins by passive diffusion along a protein concentration gradient that exists between the inside and the outside of the targeted cells. PFTs are categorized according to their tertiary protein structures into which they fold upon plasma membrane insertion[83, 89]. Colicins from *E.coli*, the translocation domain of Diptheria toxin, or the mammalian anti-apoptotic protein Bcl2 are examples of alpha-pore forming toxins. Members of his family fold into layered structures of alpha-helices. Partial unfolding of the toxin is triggered by low pH, or other mechanisms, which typically induce the formation of a hydrophobic helical hairpin that spontaneously inserts into the lipid membrane. Beta-pore-forming toxins exhibit multiple beta-sheet structures that cross the membrane[90]. Upon multimerization, each toxin monomer adopts an amphipathic beta-hairpin that docks into other monomers to form amphipathic beta-barrels. These beta-barrels have hydrophilic cavities and hydrophobic outer surfaces that promote membrane insertion[91, 92]. Different members of this toxin family recognize different cell surface receptors, such as cholesterol, gangliosides or GPI (glycosylphosphatidylinositol)-anchored proteins[93]. The choice of toxin to be employed for protein delivery may depend on which cell surface receptors are present on the targeted host cells and on the size of the pore that is required to deliver the desired protein. Toxins that form large pores, with diameters of 300 to 450 Å, usually belong to the class of cholesterol-dependent cytolysins. Toxins that form small pores, with diameters ranging from 15 to 30 Å typically belong to a family of peptides that interact with GPI-anchored proteins[94, 95].

Streptolysin O (SLO) was previously used to deliver the ^{15}N isotope-labeled Tβ4 protein into 293F cells for *in-cell* NMR applications[12]. SLO is a member of the

cholesterol-dependent, βeta-pore forming toxin family that is produced by *Streptococcus pyogenes*[93]. SLO is a oxygen-labile, sulfhydryl-activatable toxin that spontaneously loses activity in the presence of atmospheric oxygen, while it regains activity upon reduction of its single cysteine residue[96]. Cholesterol concentrations and distributions in the host membranes play a major role in the SLO binding process and therefore influence transduction efficiencies[97]. SLO toxins form homo-oligomeric, amphipathic pores with diameters between 25-50 nm. These pores extend well into the host membranes and lead to severe bi-directional cellular leakage[93]. They do, in essence, provide an open passage between the intracellular and extracellular compartment, through which molecules can move in a concentration gradient-dependent manner[91]. At high toxin concentrations, irreversible membrane damage leads to cell death by lysis. At sub-cytolytic concentrations, toxin-treated cells recover from such injuries through a series of homeostatic response processes that quickly reseal the perforated membranes[98]. Upon mild SLO exposure for example, cellular recovery is accomplished in less than one hour and via mechanisms that also involve cell-surface patching with membranes from intracellular organelles such as lysosomes, endosomes and in some instances the Golgi apparatus[99]. Membrane recovery can be enhanced by extracellular Ca^{2+}-treatment, triggering the arachidonic acid cascade that helps membrane resealing[100]. The preparation of *in-cell* NMR samples by SLO-mediated protein delivery is a three-step procedure. It involves, firstly, membrane perforation of the targeted host cells, by incubating cells with defined amounts of toxin. Second, cargo delivery by addition of isotope-labeled protein to the toxin incubation mixture and thirdly, membrane resealing by Ca^{2+}- treatment, which also results in endocytotic clearance of the toxin complexes (***Figure 4***)[101].

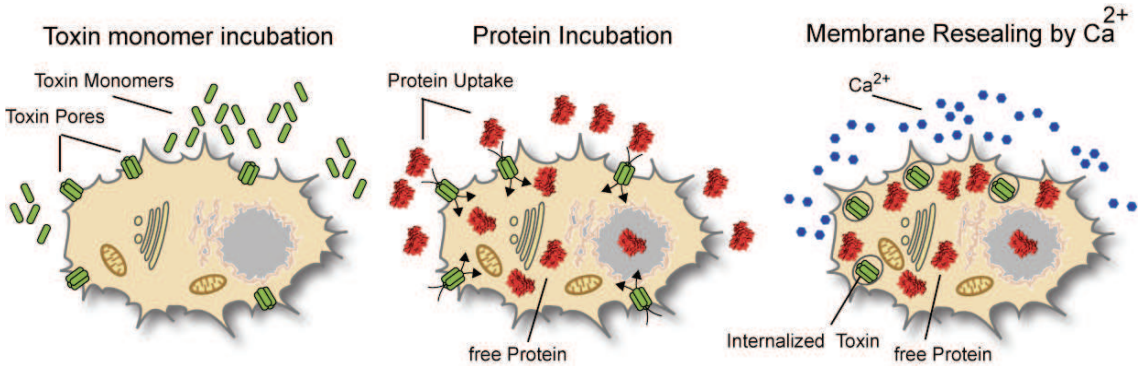

Figure 4: SLO-mediated protein delivery
In-cell NMR sample preparation routine via the SLO-mediated protein delivery approach.

Treatment of mammalian cells with even small amounts of a pore-forming toxins like SLO does, however, bear some risks and may limit the applicability for *in-cell* NMR purposes[102]. Among the drawbacks of this technique, cellular responses to cytoplasmic membrane damage may activate different signaling pathways, which in turn lead to altered cellular response behaviors[88]. PFTs have been found to induce p38 MAP kinase, which contributes to the reestablishment of intracellular ATP levels, but also signals oncogenic tranformations[103, 104]. Because of plasma membrane damage, a decrease in intracellular potassium may act as a potent activator of the inflammasome, a 'danger-sensing' protein complex that is involved in caspase 1 activation[105]. Finally, various toxins were found to have an effect on epigenetic reprogramming of targeted host cells via de-phosphorylation and de-acetylation of various sites on the histone H3 protein[106]. These effects may interfere with the intracellular characteristics of the delivered protein and may not represent the truly physiological state of the cell.

1.2.3 Protein electroporation (EP) - mediated delivery

I have outlined several drawbacks of existing protocols to deliver isotope-labeled proteins into mammalian cells for the purpose of generating suitable *in-cell* NMR samples. If one were to design an ideal method for intracellular sample delivery into mammalian cells, what needed this method to be able to do? First, it ought to be generally applicable to many different cell lines and proteins, and therefore, the uptake mechanism should preferably not require specific cell-surface receptor interactions of the protein that is to be delivered into these cells. Second, the method should be suitable to transduce 'native' proteins, without requirements for engineered protein tags, targeting sequences, or other chemical extensions that are necessary for cellular protein uptake. Such extensions and modifications will ultimately distort the structural and functional features of the protein. Third, the method should not require any treatment of cells with toxic compounds, which decrease cell viability and signal the activation of damage response pathways.

I therefore investigated the suitability of yet a third delivery approach: protein electroporation (EP). EP fulfills many of the requirements stated above and also represents a simple and fast method that can successfully be performed by inexperienced users. Furthermore EP has been optimized over many years for the intracellular delivery of DNA and RNA, with a wealth of literature to draw expertise

from for protein delivery purposes[107]. Electroporation, or electro-permeabilization methods temporarily increase the permeability of plasma membranes by exposing them to short pulses of high voltage. The first successful intracellular EP delivery of DNA molecules into mammalian cells has been reported for mouse lyoma cells in 1982[108]. Since then, EP-mediated delivery schemes for a wide range of molecules into cultured cells, tissues and organs have been developed and routine laboratory procedures for plasmid DNA or siRNA delivery have been established. Even peptide and protein EP delivery efforts have been reported[109-112]. Due to its widespread application, several technical devices for EP transduction protocols are available and some of them have been specifically developed for mammalian cells. Voltage pulse profiles and duration schemes have been optimized for different standard laboratory cell lines and defined buffer solutions for EP applications are available. In addition, EP mediated delivery of different biomolecular components is not restricted to immortalized, secondary cell lines, but can also be used with primary cells and embryonic stem cells[113, 114].

The molecular mechanisms of the actual EP process can be summarized as a 5-step procedure that is largely determined by the applied extracellular electric field[115]. Upon an EP pulse, the increase of the electrical field is referred to as the *induction* step (Step 1), which is followed by an *expansion* step (Step 2) that is maintained by what is called the 'overcritical electric field'. Following this expansion step and after the duration of the pulse, the electric field decreases and *stabilization* is achieved (Step 3) followed by membrane *resealing* (Step 4). The EP procedure is terminated by the so-called *memory effect* (Step 5). As a starting point, every cell has a resting trans-membrane potential difference ($\Delta\Psi 0$) between the extracellular and intracellular milieu, which arises due to the different ion-compositions of both environments. This potential difference is metabolically maintained and cell type-dependent[116]. $\Delta\Psi 0$ ranges between -85 mV for heart cells to -4.5 mV for red blood cells[116], where the potential of the outside environment is assumed to equal zero. During the *induction* step, the increase of the external electric field initiates a change in the transmembrane potential difference $\Delta\Psi i$. This change can be calculated by $\mathbf{\Delta\Psi i = f \times g(\lambda) \times r \times E \times \cos\varphi(M)}$, where: **f** is the shape factor of the cell, $\mathbf{g(\lambda)}$ is the conductivity of the membrane, the EP buffer and the cytoplasm, **E** is the strength of the electric field intensity and **r** is the cell radius (assumed to be spherical). φ is the angle between the direction of the membrane normal at position **M** and the direction of the electric field ***(Figure 5)***[117].

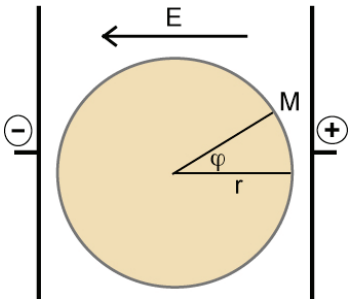

Figure 5: Increase of the transmembrane potential difference (ΔΨi) by the application of an external electric field.

Importantly, this equation tells us that the induced trans-membrane potential is not uniform over the entire cell surface, but position dependent[117]. The side of the cell that faces the anode is hyperpolarized, whereas the side that faces the cathode is depolarized. These theoretical predictions were experimentally verified with a number of voltage-sensitive fluorescent probes[118, 119]. *Induction* is followed by the *expansion* step, which describes the time period during which the external electric field exceeds the 'critical electrical value' and membrane permeabilization occurs[120]. This value has been found to be in the ~200-300 mV range[121, 122]. To reach it, an electric field 0.1-2 kV/cm lasting a minimum of a few microseconds is required, the exact number of which depends on the targeted cell type[120, 123]. Larger cells were found to be more sensitive to lower field strengths, whereas smaller cells required stronger pulses[122].

How is membrane permeabilization achieved on the molecular level? Permeabilization is due to pore formation on the lipid membrane, initiated by the reduction of the electrostatic energy of the system. Current pore models describe the formation of hydrophilic pores, where lipid head groups are assumed to line the pore interiors. These head groups tend to repel each other due to steric and electrostatic interactions[124, 125]. Penetration of water into the hydrophobic core of the lipid bilayer had been demonstrated by molecular dynamic (MD) simulations of a DMPC (dimyristoyl-phosphatidylcholine) bilayer system that was modeled by Tarek *et al.*[126]**(*Figure 6*)**. The induced hydrophobic core is eventually filled with water from either side of the lipid bilayer, which expands towards the opposite side of lipid surface. At later stages, polar lipid head groups migrate into the interior of the bilayer to stabilize the created pores[126].

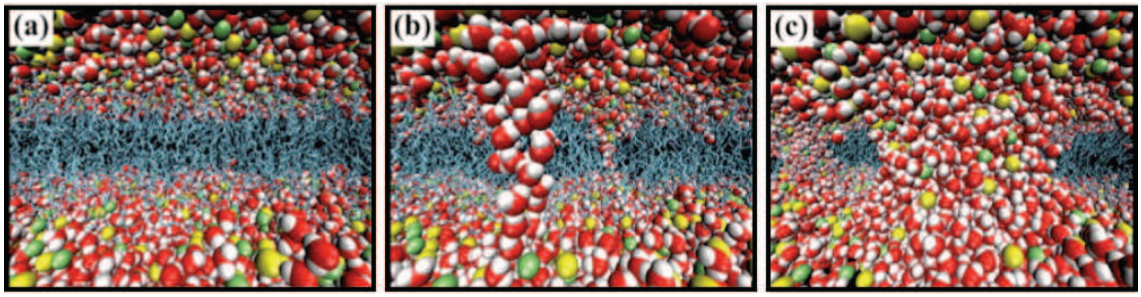

Figure 6: Molecular dynamic (MD) simulations of DMPC bilayers after electroporation[126].
(a) The lipid bilayer in equilibrium. (b) Initial stage of the electroporation process. The bilayer is exposed to a transverse electric field. (c) In later stages, water protrudes into the intramembrane space, stabilized by lipid head-groups that migrated into the interior of the lipid bilayer. (Representation of water molecules with O: red, H: white; lipid phosphate: yellow; nitrogen (green). Lipid acyl-chains are shown as sticks (blue).)

Pore densities in the case of single-cell electroporations were estimated to be on the order of 10^9 pores per cm^2 of membrane surface, where the majority of the pores (>97%) displayed small diameters, ~1 nm in size[127]. Experimentally only large post-electroporation pores were detected on red blood cells that had been pulsed under hypo-osmotic conditions[128]. Transient pore formation can be controlled by either the duration of the EP pulse and the respective electrical field strength, or by changes in pulse numbers[129]. Molecular transport during and after the pulse is an important and well-studied area of the electroporation process. Small molecule transport is primarily driven by electrophoresis and/or electro-osmosis, whereas the direct intracellular transport of large molecules such as DNA is mainly triggered by electrophoresis[130]. Molecular interactions, size and surface charge of the transported molecules may play additional roles in the respective uptake efficiencies. DNA delivery has been postulated to also involve steps during which electrostatic interactions between the transported molecules and destabilized cell membranes are present[131]. In addition, DNA transport via interactions with the microtubule network[132] and other endocytotic pathways[133] have been reported. After the EP process, cell membranes have been shown to remain leaky for small, polar components of the cell and these measured flow rates were identified to being influenced by the temperature of the system[129]. Leakage of proteins and other macromolecules, however, proved to be virtually absent due the small sizes of these pores. Indeed, no significant changes in the steady-state levels of three endogenous proteins, gp135, E-cadherin, and the Na^+-K^+-ATPase were reported after nucleofection[134].

Once the external electric field is switched off, or decreased below the critical permeabilizing threshold, *stabilization* and *resealing* take place. Both phenomena were shown to be highly temperature dependent and influenced by the degree of membrane reorganization[118, 129]. The involvements of both membrane proteins and the cytoskeleton have been suggested to contribute to the stabilization and resealing process. Electroporation of adherent cells revealed that the electric pulse interfered with the organization of actin or tubulin filaments inside treated cells, but it did not result in the immediate or subsequent degradation of actin or tubulin monomers. Microtubule and microfilament networks were able to recover within 1 to 2 hours after the electroporation procedure[135].

In-cell NMR sample preparation by protein electroporation is a one step process and EP-induced pores rapidly reseal once the electric field has been switched off (***Figure 7***).

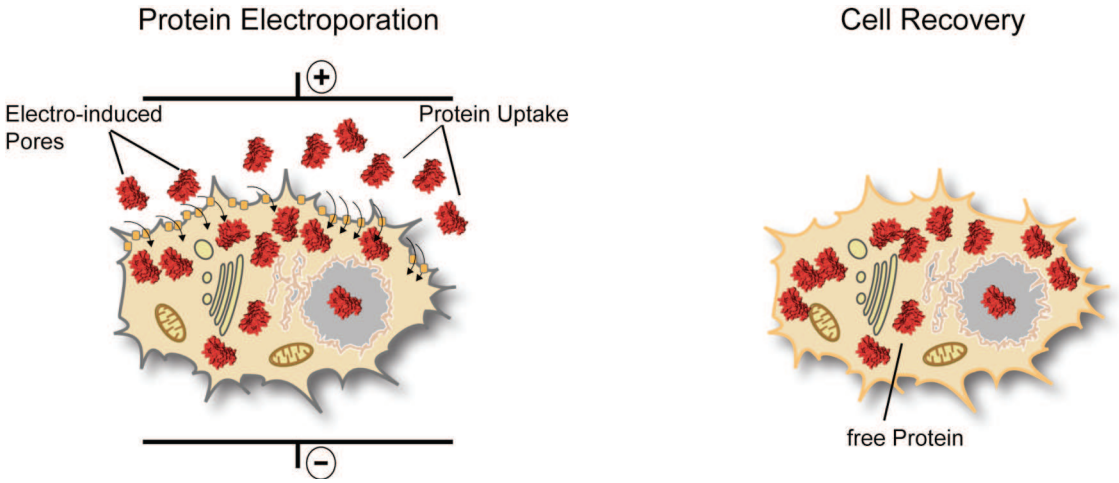

Figure 7: Protein electroporation
In-cell NMR sample preparation routine via the EP-mediated protein delivery approach.

Finally, the m*emory effect* is considered the last step of the electroporation process. Despite the fact that cells recover easily and show normal behavior after the EP procedure, changes in the intracellular cytoskeleton network may remain, thus limiting certain applications of the technique. Increased metabolic activity[136] and the induction of eukaryotic translation initiation factor 2 (eIF2α) phosphorylation have been reported to occur up to 2 hours after the EP procedure[137].

1.3 Proteins models

Although *in-cell* NMR is a powerful technique to study protein structures and dynamics at atomic resolution inside cells, the ability to detect NMR protein signals in the first place is highly influenced by the nature of the protein that is to be studied in relation to its biological activity in the intracellular environment. High intracellular viscosity and macromolecular crowding influence global and local protein motions, which is reflected by characteristic changes in longitudinal and transverse protein relaxation rates (R1, R2)[138]. Higher R2 values are characteristics for fold-, as well as intrinsically disordered -proteins in viscous environments, which can lead to severe line broadening and complete loss of NMR resonance signals[4, 139]. Li *et al*. showed that globular proteins are even more sensitive to intracellular viscosity than intrinsically disordered ones (IDP) and thus that the relaxation properties of IDPs are more suitable for *in-cell* NMR investigations[139-141]. In addition to their dynamic properties, the size of the protein that is be studied by *in-cell* NMR is another factor that could limit the suitability of this type of approach[9].

1.3.1 Folded model protein: GB1

GB1 is the B1 immunoglobulin-binding domain of *staphylococcal* protein G. This small, 7 kDa globular protein domain consists of a four-stranded β-sheet that is packed against a single alpha-helix. GB1 is widely used as a model globular protein domain in many different NMR studies, including *in-cell* NMR applications[43, 142]. Prokaryotic *in-cell* NMR studies revealed that at intracellular concentrations of ~ 1.5 mM GB1 yield detectable NMR resonance signals inside live *E.coli* cells[5] and in eukaryotic *Xenopus laevis* oocytes, at intracellular concentrations of 50-500 μM[43].

1.3.2 IDP model protein: αSynuclein

Intrinsically disordered proteins (IDPs), or intrinsically disordered protein regions (IDRs) lack defined secondary and/or tertiary structure in their native states[143]. IDPs can nevertheless exhibit defined short-, or long-range intramolecular contacts, which often result in non-extended, globular overall structural organizations[144, 145] that are sometimes linked to specific IDP functions[146, 147]. Changes in these native states correlate with human pathologies, in particular with many aggregation disorders and

amyloid diseases[148-150] ***(Figure 8)***. Conformational changes in disordered proteins and protein regions can additionally be induced by lipid binding[151], interaction with protein partners[152, 153], post-translational protein modifications, or aggregation itself[154]. Such structural changes, can be easily followed by *in-cell* NMR spectroscopy[155]. In this study, a disease-related, intrinsically disordered protein, human αSyn and the two *Synuclein* isoforms, βSyn and γSyn were chosen as model proteins for initial *in-cell* NMR investigations in mammalian cells.

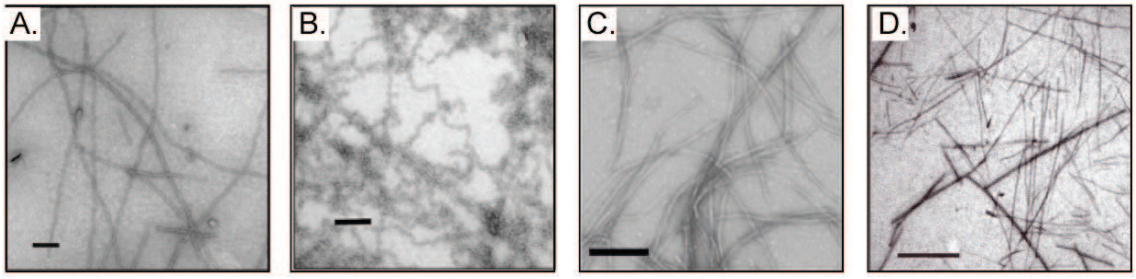

Figure 8: Electron micrographs of negative-stain amyloid fibrils
A) Turkey lysozyme fibrils, scale bar 200 nm [156], B) human alpha lactalbumin fibrils, scale bar 200nm [156], C) Fibrils of the amyloid B peptide (aa1-40), scale bar 200nm [157], D) Prion protein fibrils, scale bar 500 nm [158].

1.3.2.1 Physiological roles of αSyn

Synucleins (Syn) are small intrinsically disordered proteins (αSyn 140aa, βSyn 137aa and γSyn 127aa) that occur throughout the brain in many neural cells. Whereas α-, and βSyn are predominantly present in neuronal cells of the central nervous system (CNS)[159-162], γSyn is found in various cancer cell types of the peripheral nervous system, in motor neurons and in sensory neurons[163]. αSyn, the main focus of this study, is predominantly found in the *substantia nigra pars compacta*, the hippocampus, the thalamus and the amygdala of the CNS ***(Figure 9)***. Low levels of the protein were also found in several other organs, including the pancreas, kidney, skeletal muscles, the liver, lung, placenta and the heart[164, 165]. Significant amounts of αSyn were also isolated from red blood cells[166]. In neuronal cells, αSyn accumulates at pre-synaptic terminals, however it was also found in the neuronal stroma and nucleus[167, 168]. Furthermore, αSyn contains a hypothetical mitochondrial targeting sequence at its N-terminus and was shown to accumulate in the inner mitochondrial membrane of dopaminergic primary

neurons[169] in transgenic mice[170] and to co-localize with outer mitochondrial membranes in cultured neural cells[171].

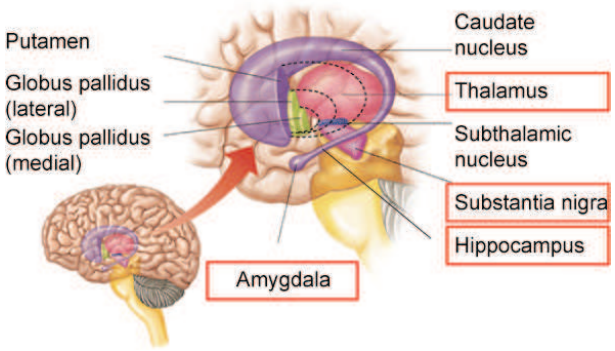

Figure 9: High αSyn levels in the CNS.
αSynuclein is found in the thalamus, the *substantia nigra*, the hippocampus and the amygdala, highlighted with red boxes.

Physiological functions of αSyn are still under debate. Due to its localization, several reports have implicated a biological role at synaptic terminals. αSyn has been shown to stabilize cholesterol and sphingomyelin containing vesicles and to impair their fusogenic properties *in vitro*[172]. *In vivo* studies confirmed, that αSyn overexpression decreased the release of the neurotransmitter dopamine, presumably by interfering with readily recycling pools of synaptic vesicles at pre-synaptic terminals[173, 174]. Direct binding of the C-terminus of αSyn to synaptobrevin-2 (Syb2) has been reported and αSyn has been suggested to promote the assembly of the SNARE complex, together with another neuronal protein, the cysteine-string protein α (CSPα). Both proteins act as chaperons in maintaining proper SNARE assembly and disassembly[175, 176] (***Figure 10***).

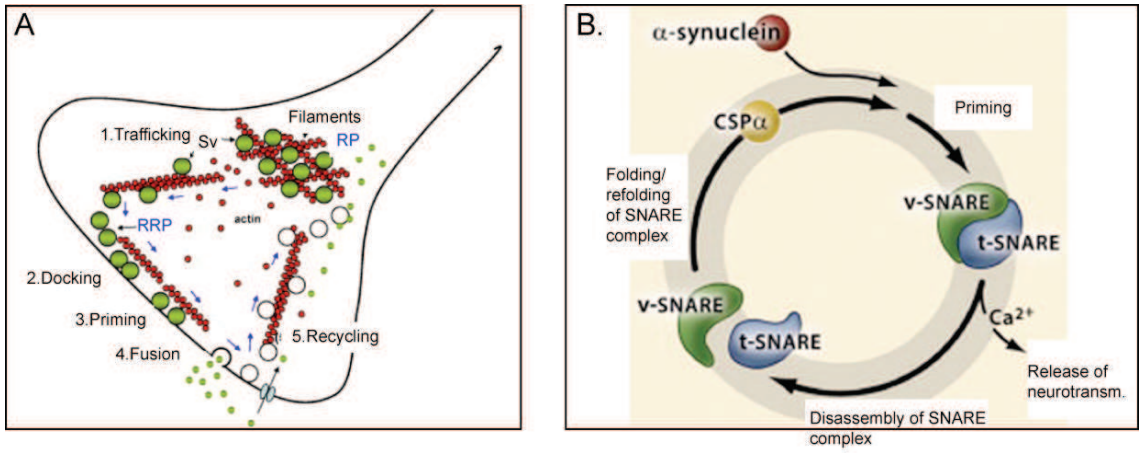

Figure 10: Biological roles of αSyn
A) Possible functions of αSyn in the regulation of synaptic vesicle cycling[174]. αSyn may interfere with the docking, priming and fusion of synaptic vesicles (SVs), interact with actin filaments (red) and influence the recycling of the dopamine neurotransmitter (green). RP and RRP stand for "reserve" and

"readily releasable VS pool" respectively. B) Chaperon activities of αSyn and of the cysteine-string protein α (CSPα) in the assembly of the synaptic SNARE complex[176]. Following conformational changes (priming) of the SNARE complex and subsequent Ca^{2+}-influx, SVs fuse with the plasma membrane and release dopamine into the synaptic cleft. Following this, the SNARE complex is disassembled.

1.3.2.2 Structural characteristics

αSyn, βSyn and γSyn share a highly conserved N-terminal region that mediates binding to lipid membranes via the formation of an extended alpha-helical structure[151, 177-179]. C-termini of *Synuclein* family members are less well conserved. The primary amino acid sequence of γSyn is shorter and it has the least conserved and least negatively charged C-terminus[164, 165]. A multiple sequence alignment of the different *Synuclein* isoforms is shown in ***Figure 11***.

αSyn	MDVFMKGLSK	AKEGVVAAAE	KTKQGVAEAA	GKTKEGVLYV	GSKTKEGVVH	50
βSyn	MDVFMKGLS**M**	AKEGVVAAAE	KTKQGV**T**EAA	**E**KTKEGVLYV	GSKT**R**EGVV**Q**	50
γSyn	MDVF**K** KG**F**S**I**	AKEGVV**G**A**V**E	KTKQGV**T**EAA	**E**KTKEGV**M**YV	GSKTKE**N**VV**Q**	50
αSyn	GVATVAEKTK	EQVTNVGGAV	VTGVTAVAQK	TVEGAGSIAA	ATGFVKKDQL	100
βSyn	GVA**S**VAEKTK	EQ**ASHL**GGAV	**FS**G - - - - - - -	- - - - AG**N**IAA	ATG**L**VK**REE F**	89
γSyn	**S**V**TS**VAEKTK	EQ**ANA**V**SE**AV	V**SS**V**NT**VA**T**K	TVE**EA**E**N**IA**V**	**TS**G**V**V**R**K**ED**L	100
αSyn	GKNE - - - - - E	GAPQEGILED	MPVDPDNEAY	EMPSEEGYQD	YEPEA	140
βSyn	PTDL KPEEVA	**QEAA**E**EP**L**IE**	**PLME**P**EG**E**S**Y	E**D**P**PQ**E**E**YQ**E**	YEPEA	134
γSyn	RPSAPQQEG-	- - - - - - - - - -	- - - **VASK**E -**K**	E**EVA**EE**AQSG**	**GD**	127

Figure 11: Multiple sequence alignment of α-, β- and γSyn
Gray boxes indicate the conserved lipid-binding region. Letters in bold indicate differences in amino acid compositions.

αSyn contains three functionally distinct domains. The N-terminal, lipid-binding region (aa1-60) that includes the well-conserved, imperfect KTKEGV repeats[179, 180] (***Figure 12, A)***, the middle domain (aa61-95), which also contains the non-amyloid beta-component (NAC) region (aa85-95), which constitutes the hydrophobic region of the protein that is strictly required for aggregate formation[181] and absent in βSyn[182] and the C-terminal region spanning amino acids 96-140, which is highly acidic, thought to block spontaneous fibril formation and to comprise αSyn's chaperon activity[183]. Despite the intrinsically unfolded state of the protein, αSyn has been shown to adopt a compact overall shape in solution, which is caused by transient long-range contacts of different sites within the protein[184, 185] (***Figure 12, B)***. The most important intramolecular contacts are established by residues of the C-terminus with parts of the hydrophobic NAC region[185]. The C-terminus also interacts with the first 20 residues of αSyn. These interactions exert a stabilizing effect on the protein and inhibit

spontaneous aggregation[184]. βSyn and γSyn adopt more extended conformations, due to the lack of long-range contacts within these proteins[186].

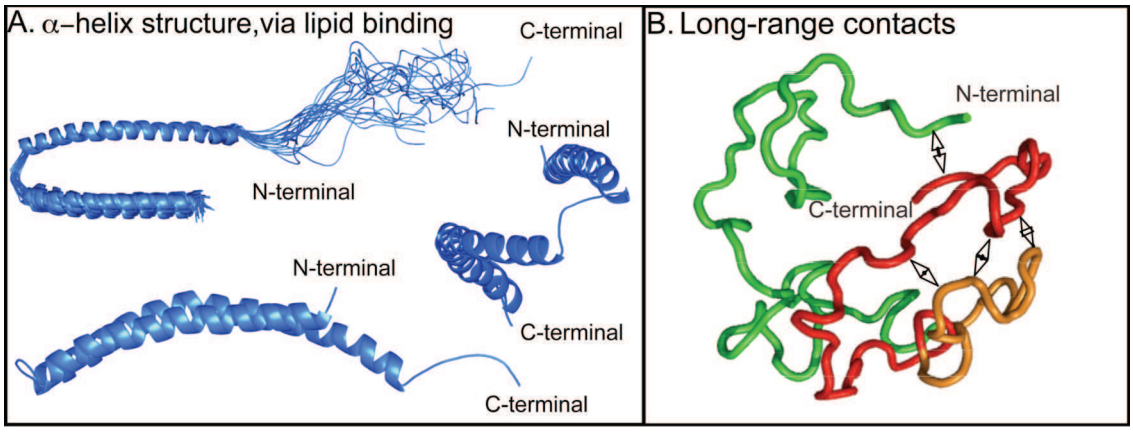

Figure 12: Structural properties of αSyn
A) Different alpha-helical structures of micelle-bound αSyn as determined by solution-state NMR spectroscopy[187]. B) Transient long-range contacts between the N (green) -, and C (red) -termini, and C-terminus and the NAC region (orange) of αSyn[184].

1.3.2.3 Disease relevance

Structural differences of the *Synuclein* proteins correlate with different propensities for aggregation. αSyn and disease-related, familial point mutants that cause early onset Parkinson's disease (PD) are highly prone to aggregate into amyloid fibrils[188,189,190] (***Figure 13, A***) under a variety of *in vitro* conditions[191]. Fibrillation occurs via structural reorganizations of the monomeric forms of αSyn into highly structured, beta-rich fibrils[189] that eventually precipitate to form cytoplasmic inclusions (***Figure 13, B***) in neuronal and glia cells[192, 193]. These inclusions, also termed Lewy bodies are pathological hallmarks of PD and other synucleinopathies[15], such as dementia with Lewy bodies (DLB) and multiple system atrophy (MSA)[194, 195]. PD is the second most common neurodegenerative disease. It is caused by selective cell death of dopaminergic neurons of the *subtantia nigra pars compacta (SNpc)* in the midbrain[20]. The *subtantia nigra* is a darkly pigmented area of the midbrain that is reduced in size in PD patients (***Figure 13, C***). The exact mechanisms of cell death in this particular brain region are subject to many investigations[196] and it appears that cell death is particularly promoted by the formation of prefibrillar αSyn oligomers[197, 198] rather than by the presence of mature amyloid fibrils[199]. Toxic effects are believed to be exerted by the lipid binding capacities of these prefibrillar species[200, 201] (***Figure 13, D***) and their tendencies to form membranes pores[202] (***Figure 13, E***).

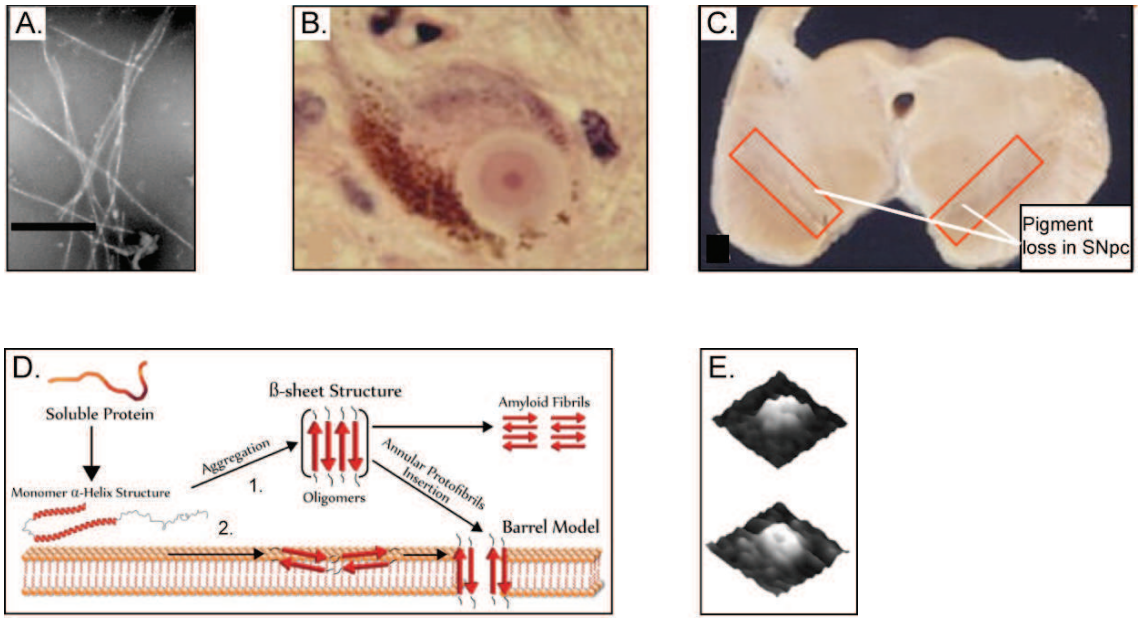

Figure 13: Pathological roles of αSyn
A) Transmission electron microscopy (TEM) images of αSyn fibrils, scale bar 160 nm [191]. B) Lewy bodies of the *SNpc*, stained with haematoxylin[203]. C) Loss of dopaminergic neurons in the *SNpc* in PD brains[203] D) αSyn aggregation and pore formation model. Enrichment of β-sheet-containing fibrils in the extracellular space (1) or at the plasma membrane (2). These species are thought to induce the formation of pores or channels[201]. E) High-resolution atomic force microscopy images of pore-like structures of αSyn[202].

Aggregation of monomeric αSyn is promoted by the crowded environment of the intracellular space[204]. In turn, aggregation kinetics are influenced by several factors, such as oxidative stress[205-207], enhanced levels of intracellular Ca[208], serum deprivation[209], or certain post-translational modifications[19]. Moreover, the aggregation process itself proved to be nucleation dependent[210] and can be seeded with catalytic amounts of prefibrillar species[211], or even mature fibrils[212]. Additionally, both monomeric and aggregated forms of αSyn can be secreted from cells by exocytosis[213, 214], as well as taken up by surrounding cells via endocytotic mechanisms[215]. These observations may provide an explanation of how the pathology might spread throughout the nervous system in a manner that is similar to prion diseases[216]. Despite a wealth of information about αSyn, only little is known about β- and γSyn. Both proteins were never detected in Lewy bodies[217] and fail to aggregate *in vitro*[218]. These findings are in line with the notion that βSyn does not posses a sequence-conserved hydrophobic NAC region[148]. Interestingly, overexpression of βSyn has been shown to impair Lewy body formation in transgenic mice that also overexpress

αSyn[219], which suggests a possible protective role for βSyn in the course of αSyn aggregation[218].

1.3.2.4 Post-translational modifications of αSyn

As mentioned before, post-translational modifications can also modulate the aggregation propensities of αSyn. In Lewy bodies, αSyn is found to be either phosphorylated, ubiquitinated or acetylated[220]. αSyn contains multiple phosphorylation sites (Ser87, Ser129 and Tyr125, Tyr133, Tyr135 reviewed in Oueslati *et al.*[221]). Ser129 is considered to constitute the main αSyn phosphorylation site, possibly modified by the CK1, CK2, or PLK1-3 protein kinases[25, 222]. Interestingly, most of αSyn that is present in Lewy bodies of PD patients (>90%)[223], or in monkey[224], or rat[225] PD models is phosphorylated at Ser129. In contrast, only 4% of soluble endogenous αSyn has been found to be phosphorylated in healthy individuals[223]. Similar to Ser129 phosphorylation, modification of Ser87 residue has been identified to be present in Lewy bodies of DLB patients, where phosphorylation has been shown to block fibrillation *in vivo*[226].

Ubiquitinated forms of αSyn have been found to a lesser extent and these modifications primarily occurred within the N-terminus of the protein at Lys12, Lys21, and Lys23[227]. N-terminal acetylation of αSyn is the only PTM that has been identified in both the soluble and insoluble brain fractions of PD patients[220, 228]. N-terminal acetylation occurs on the first methionine residue and be catalyzed *in vitro* by action of the N-acetyltransferase B (NaB)[229]. Acetylation has been shown to increase the alpha-helical propensities of αSyn, without obvious effects on its aggregation properties[230]. Based on the more alpha-helical nature of the N-terminus of αSyn, a two-fold higher affinity to lipid membranes has been reported[230]. However, recent *in vivo* studies suggested that N-terminal acetylation did not change subcellular localization, or the overall membrane binding affinity of αSyn inside intact cells[24].

In summary, αSyn, an aggregation prone intrinsically disordered protein constitutes the prime target of this study. Although the physiological functions of αSyn are poorly understood, it is causally implicated in cell death in several neurodegenerative diseases where it forms insoluble deposits and amyloid fibrils. *In-cell* NMR spectroscopy is an excellent tool to follow the structural and functional

changes that accompany the process of amyloid formation in the crowded intracellular environments of intact neuronal cells. Structural changes of the monomeric protein can be followed upon lipid binding, post-translational protein modifications or other intracellular events that lead to aggregation, in a time resolved manner and at atomic resolution.

1.4 Cellular models to study αSyn aggregation by *in-cell* NMR

Five different mammalian cells types have been selected to study intracellular αSyn by *in-cell* NMR spectroscopy. These include non disease-related cells of non-neuronal origins and disease-related neuronal cells. A2780 cells from ovaries and HeLa cervical cancer cells have been chosen as non disease-related cellular models. Cells of functional relevance to PD are the dopaminergic neuronal cells SK-N-SH[231], B65[232] and RCSN3[21, 233, 234]. RCSN3 cells are most directly relevant to PD because they are derived from *substantia nigra* neurons (***Figure 14***).

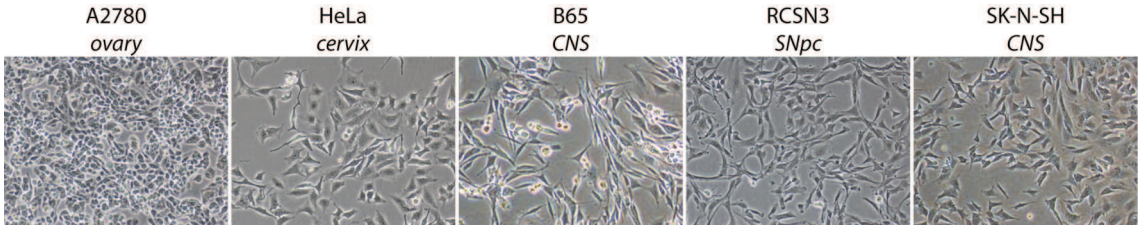

Figure 14: Non-neuronal and dopaminergic neuronal cell lines used in this *in-cell* NMR study (CNS: central nervous system, *SNpc*: *substantia nigra*, *pars compacta*)

2. Results

In the first part of this section, I discuss the three different methods to introduce isotope-labeled proteins into the cytosol of mammalian cells in a comparative manner. In the second part, the most suitable protein delivery method is exploited to study the structural and dynamic features of PD-related αSyn and the other *Synuclein* isoforms by high-resolution *in-cell* NMR spectroscopy.

2.1 Part 1: Protein transduction methods

2.1.1 Cell and protein models

Two previously published methods for intracellular protein delivery that employ either *Cell Penetrating Peptide*s (CPPs), or Streptolysin O-mediated protein delivery, as well as a protein electroporation (EP) were analyzed for their suitability to transduce NMR-active, isotope-labeled proteins into mammalian cells. Human embryonic kidney HEK293 (HEK) cells, human cervical cancer cells (HeLa), rat neuroblastoma cells (RCSN3) and mouse neuroblastoma cells (Neuro2a) were initially used in these comparative studies. The folded protein G B1 domain (GB1, ~7 kDa) and disordered human αSynuclein (αSyn, ~14 kDa) were selected as the target cargo proteins for intracellular sample delivery. His-tagged green fluorescent protein (hGFP), the heat shock protein Hsp12, a peptide corresponding to the N-terminal tail region of histone H3 (aa1-33), the N-terminal transactivation domain (NTAD) of human p53 (aa1-64) and a model CKII kinase substrate peptide were additionally used to establish the general validity of the obtained results.

2.1.2 Data analysis

For all protein transduction techniques, three parameters were analyzed by dual channel flow cytometry: The % of cell death, the % of cells that had taken up the target proteins and the levels of protein uptake in protein positive cells, as measured by the median fluorescence intensity (MFI). To measure cellular viability and the extent of cell death, treated cells were incubated with a late apoptotic marker 7-amino-actinomycin D (AAD7). AAD7 intercalates with double-stranded nucleic acids and is

not taken up by viable cells. Disintegration of cell membranes upon cell death leads to AAD7 influx and DNA staining, which is registered in the flow cytometer. Protein uptake was measured by the detection of a fluorescein signal that was either present as part of the CPP moiety covalently coupled to the cargo proteins, or, as in the case of SLO- and EP-mediated protein delivery, by detection of Atto488 fluorescence. This dye was directly attached to the tested cargo proteins via a lysine side-chain coupling reaction. Treated cells were sorted in the flow cytometer and counted based on their fluorescence signals, either as AAD7 positive, dead cells, or as protein positive live cells. Average cell death was determined by the number of cells that stained positive for AAD7, whereas protein uptake efficiencies were established by the number of AAD7 negative cells that contained the delivered protein(s). The median fluorescent intensity values (MFI) of protein uptake were used to semi-quantitatively evaluate initial intracellular protein concentrations inside the viable cells. Small-scale experiments were performed first on 1-2 million cell batches, of which 3000-5000 cells were counted and analyzed by flow cytometry. Bar graphs in the following figures show mean results of three parallel experiments. Error bars represent standard deviations. Intracellular protein distributions were analyzed by live cell imaging using confocal microscopy.

2.1.2.1 Covalent coupling of cargo proteins to the Tat CPP - peptide

To generate covalently linked CPP-cargo constructs[235,236], coupling of the CPP moiety to the cargo protein was achieved via an oxidative disulfide reaction. Because coupling efficiencies are influenced by the position of the CPP tag, CPP-acceptor cysteines were introduced at both the N- and C-terminal ends of the cargo proteins (i.e. GB1 and αSyn). Cysteine-containing αSyn was generated by restriction free cloning. Cysteine-containing GB1 was available in the Selenko laboratory. The Tat-HIV (referred to as Tat from now on) CPP was produced by solid phase peptide synthesis (SPPS) in the laboratory of Dirk Schwarzer (FMP, Berlin). CPP peptides were synthesized to contain an additional N-terminal S-3-nitro-2-pyridinesulphenyl group for optimal coupling and a C-terminal fluorescein tag for facile detection by SDS-PAGE (see below), flow cytometry and fluorescence microscopy **(*Figure 15*)**.

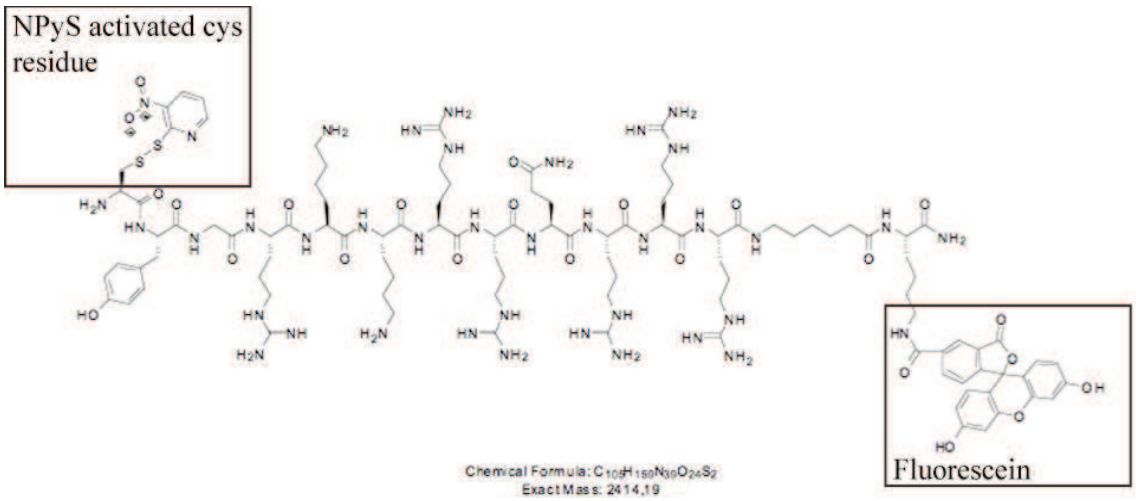

Figure 15: 3-nitro-2-pyridinesulphenyl-activated and fluorescein-tagged Tat-HIV (aa47-57) for CPP-mediated protein delivery.

N- and C-terminal disulfide coupling was performed *in vitro* with a 2-4 molar excess of the Tat CPP and cysteine-containing GB1, or αSyn. Coupling reactions were performed at room temperature for 10 and 30 min and for 1 h of incubation time. Average coupling efficiencies were 40% for both αSynTat and TatαSyn ***(Figure 16, A)***, and 30% for GB1Tat and TatGB1 ***(Figure 16, B)*** for the 1 h coupling reactions at room temperature. A greater excess of Tat peptides led to increased CPP-dimer formation and did not increase overall coupling efficiencies. However, higher amounts of unspecific side products were observed at these CPP concentrations (data not shown). Successful coupling was identified by DTT treatment and SDS-PAGE ***(Figure 16, A)***. No significant differences were observed in the coupling reactions that fused the CPP moieties to the N-, or C-termini of the target proteins. Separation of non-reacted Tat peptides was achieved by ion exchange chromatography, dialysis and size exclusion chromatography on PD G-25 columns. Best separation of monomeric and dimeric Tat peptides, however, was achieved by large-scale size-exclusion chromatography (SEC). For unknown reasons, separating the non-reacted CPP Tat peptides from the other components of in reaction mixtures proved more efficient in the C-terminal coupling reactions yielding αSynTat products ***(Figure 16, A)***. Because mixtures of the TatαSyn reaction still contained high levels of non-reacted CPP molecules, even after SEC, subsequent uptake experiments were primarily performed with αSynTat constructs. As outlined below, solutions of free Tat peptides promoted cell death and were therefore avoided ***(Figure 17)***. Cysteine-containing GB1 showed increased dimer formation, but uncoupled Tat peptides were completely removed by SEC. Due to the lower overall

yields of TatGB1 ***(Figure 16, B)***, CPP-mediated uptake experiments were primarily performed with GB1Tat constructs.

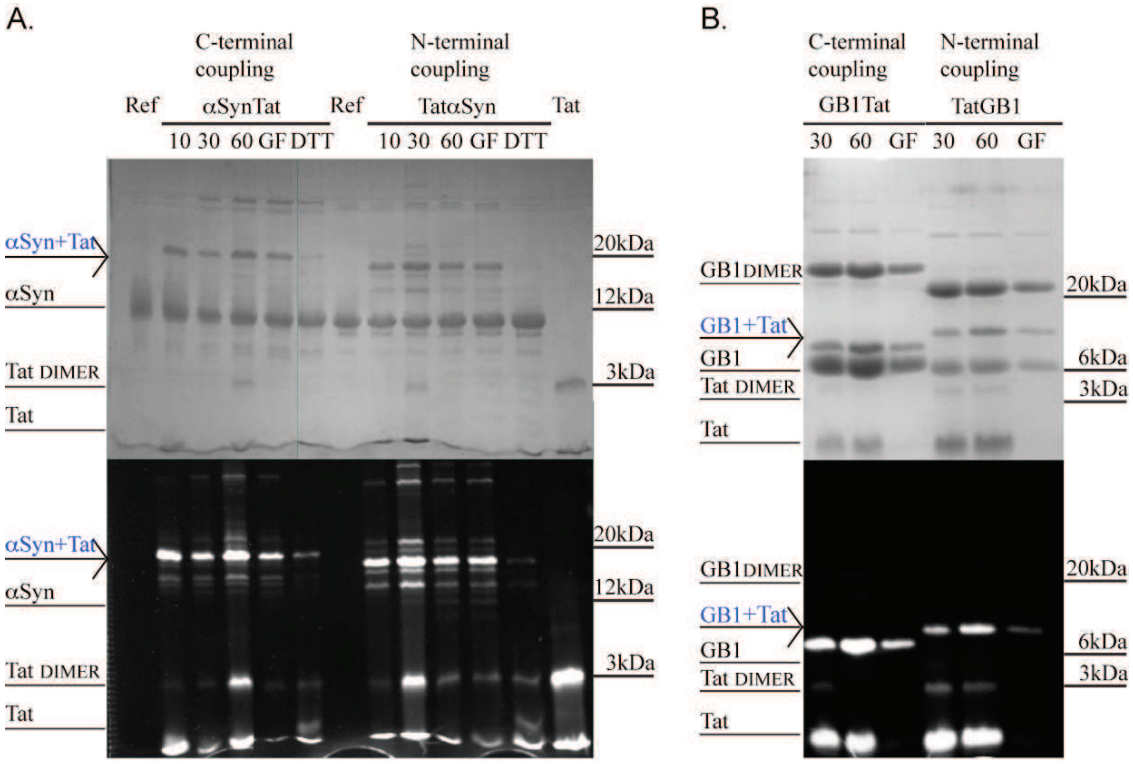

Figure 16: Disulfide coupling of C-, and N-terminal cysteine containing cargo proteins αSyn (A)/ GB1 (B) and the Tat CPP peptide
(Top) Coomassie stained SDS-PAGE (non reducing). (Bottom) SDS-PAGE under UV illumination. The CPP moiety is detected based on its fluorescein tag. Successfully coupled products are shown in blue.

2.1.2.2 Cellular toxicity of non-reacted Tat peptides

To assess possible toxic effects of non-reacted Tat molecules, free peptides were dissolved in PBS buffer at different concentrations (5, 10 and 50 µM) and added to HeLa, HEK and RCSN3 cells for 1 h at room temperature. Mock treated cells were used as controls. Presence of the free Tat peptide significantly decreased overall cell viability (30-55 %) on all tested cell lines, even at the lowest concentration ***(Figure 17)***. This increase in cell death stressed the importance of separating non-reacted Tat peptides in the coupling mixtures before adding these solutions to cell cultures for protein delivery.

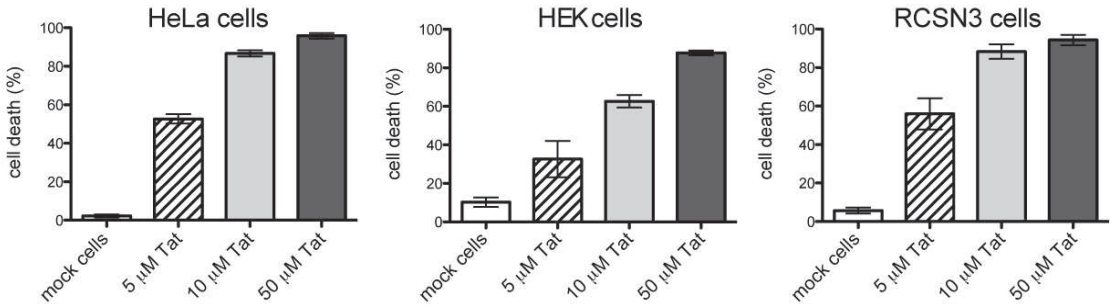

Figure 17: Toxicity of the uncoupled Tat peptide
Toxic effects of free Tat peptide at different concentrations (5, 10 and 50 µM) tested on HeLa, HEK and RCSN3 cells. Cell death of mock treated cells were determined in the absence of the Tat peptide. Cell death was assessed by flow cytometry by detection of the viability marker AAD7. Graphs indicate mean values (n = 3) with standard deviations. Significantly decreased cell viability of all the tested cell lines was observed even at the lowest tested Tat concentrations (5 µM).

2.1.2.3 Protein uptake and cell death using the CPP method

After these initial experiments, covalently coupled αSynTat and GB1Tat constructs were employed in uptake experiments on HeLa, HEK and RCSN3 cells, where the CPP-cargo constructs were dissolved in PBS at 50 µM concentrations. Cells incubated with these constructs showed significantly lower toxicity. Cell death varied between ~10-25 % ***(Figure 18)*** whereas the free Tat peptide induced ~30-55 % of cell death, as shown before, even at the lowest tested concentration ***(Figure 17)***. This confirmed that even though free CPPs displayed high cytotoxicity, this effect was reduced when CPPs were coupled onto proteins[237]. Toxicity differences between the different cell lines were negligible, while protein uptake efficiencies were cell line dependent. Uptake efficiencies in HeLa and RCSN3 cells were relatively low (~22-40 %). In contrast, HEK cells showed good transduction efficiencies (~60-65%). No substantial differences were observed between αSynTat and GB1Tat constructs in any of the three cell lines ***(Figure 18)***.

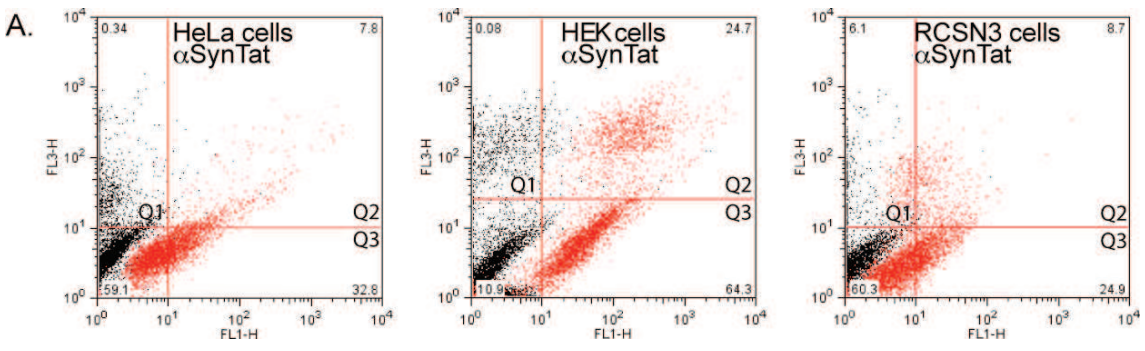

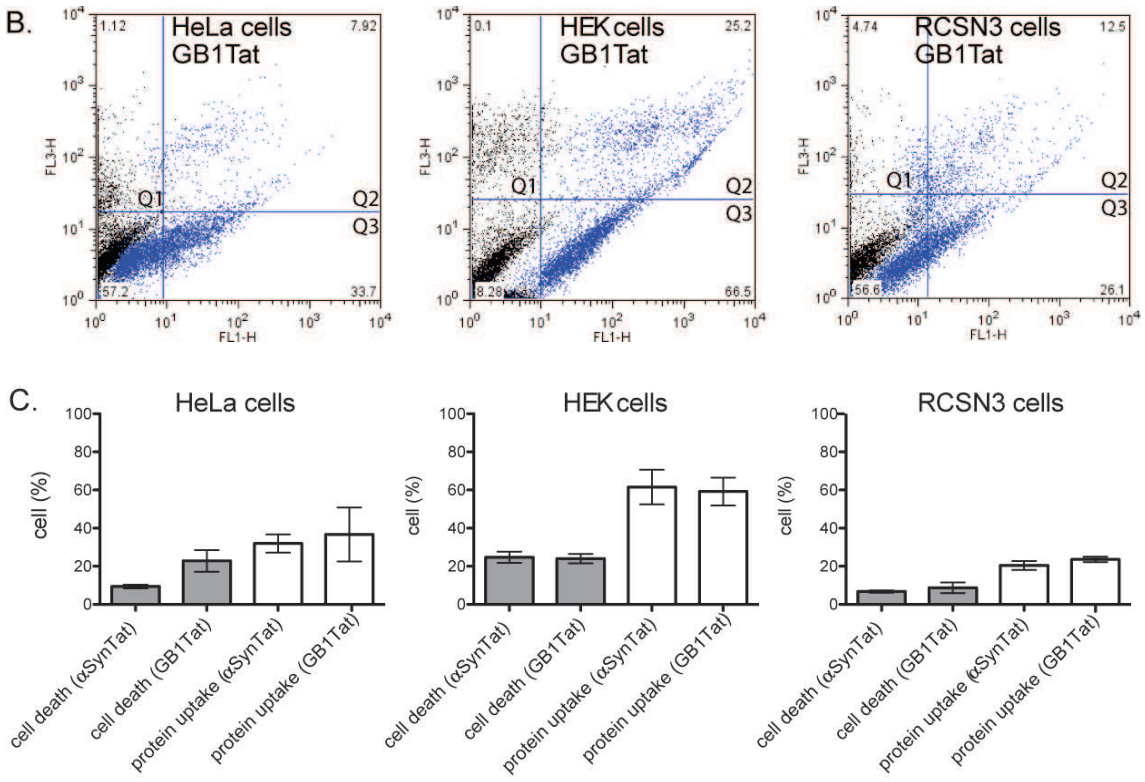

Figure 18: CPP-mediated delivery of αSynTat and GB1Tat into different cells
(A), (B) Flow cytometry dual channel analysis of mock (black), αSynTat (red) and GB1Tat (blue) treated cells. Analysis was performed by detection of AAD7 (cell viability) and the fluorescein tagged Tat peptide. (C) Cell death and protein uptake of αSynTat and GB1Tat. Graphs show mean values (n = 3) with SDs. 10-25 % cell death was detected among the different cell lines. Protein uptake showed high cell-line dependence. No significant differences between the CPP-cargo constructs within a certain cell line were observed.

2.1.2.4 CPP - mediated delivery with pyrenebutyrate pre-incubation

Among cationic CPPs, such as the Tat peptide, endocytosis is the proposed uptake mechanism[65]. Pyrenebutyrate (PA) has been reported to generally increase CPP-mediated protein uptake by promoting a non-endosomal, direct cargo transduction mechanism[238]. HeLa and Neuro2a cells were treated with 50 µM αSynTat, with, or without a 10 minute pre-incubation step with 50 µM of PA at 37° C. In cases where PA was added, the drug was also present at the same concentration during the CPP-cargo incubation step. In contrast to published results, I found that overall protein uptake efficiencies (Q3) decreased by ~5-9 % with PA pre-incubation, for both tested cell lines ***(Figure 19)***.

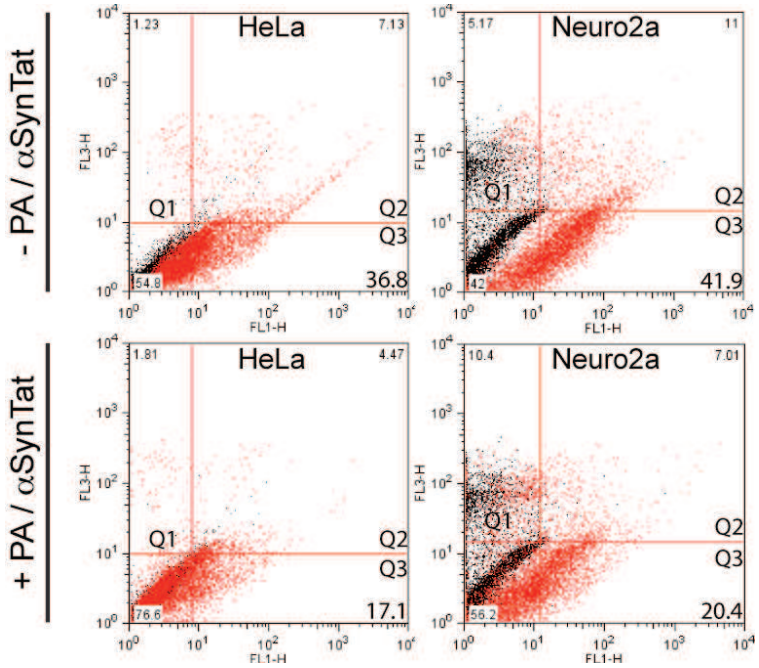

Figure 19: CPP-mediated protein delivery with PA pre-incubation
Dual channel flow cytometry analysis of αSynTat delivery into HeLa and Neuro2a cells without (top) or with (bottom) pyrenebutyrate treatment. Mock treated cells in the absence of the αSynTat construct are shown on black. Overall Protein uptake was lower in PA treated cells (Q3).

2.1.2.5 Intracellular concentration and distribution of CPP - delivered αSyn

Median fluorescence intensity (MFI) values of protein uptake were determined to semi-quantitatively assess intracellular protein concentrations. 50 µM αSynTat was added to HeLa, Neuro2a and RCSN3 cells and cells were also analyzed by live-cell confocal imaging. Cells were imaged within 1 h after CPP-cargo incubation. MFI values were comparable for HeLa and HEK cell lines (20-35 MFI), but lower for RCSN3 cells (15 MFI) (***Figure 20***). Live-cell imaging analysis revealed a punctuated intracellular distribution of αSynTat in HeLa and Neuro2a cells and the presence of bright aggregate-like structures in RCSN3 cells ***(Figure 20)***.

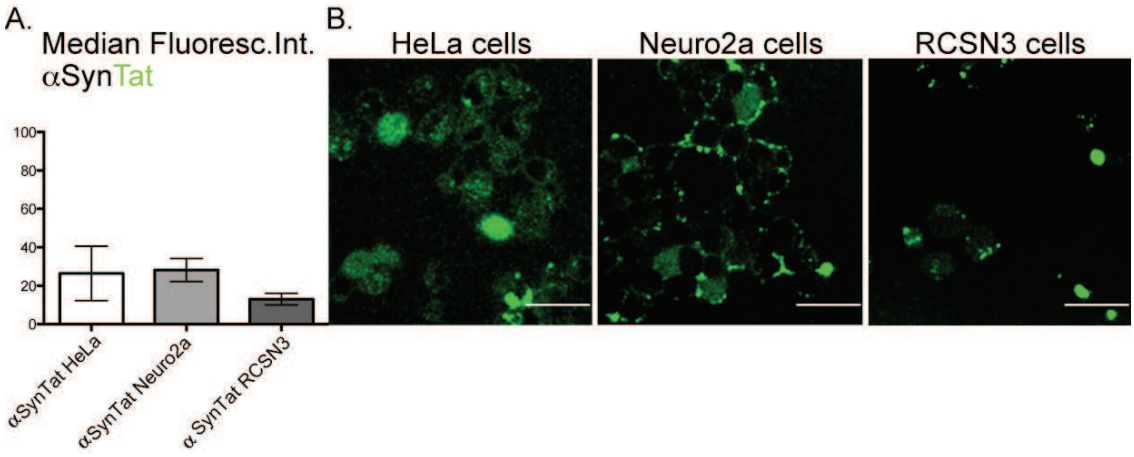

Figure 20: Intracellular concentration and distribution of αSynTat
(A) 50 µM of αSynTat were applied for CPP-mediated uptake experiments. MFI values of protein uptake are shown as bar graphs with SDs (n = 3). Fluorescence intensities were comparable for HeLa and Neuro2a cells, but lower for RCSN3 cells. (B) Live-cell confocal imaging of intracellular αSynTat distributions. Fluorescence microscopy revealed a dotted distribution of αSynTat in HeLa and Neuro2a cells, and aggregate-like structures in RCSN3 cells. Scale bar = 50 µm.

2.1.3 Streptolysin O (SLO) - mediated delivery

In this section, I present results from protein delivery trials with the pore-forming toxin Streptolysin O (SLO)[239, 240]. Cellular uptake of exogenous protein material by action of pore-forming toxins offers the possibility to deliver purified proteins into the cytoplasm of live cells without the need to couple the protein of interest to a carrier molecule such as CPP.

2.1.3.1 Optimization of SLO concentrations

For SLO-mediated protein delivery procedures, suitable SLO toxin concentrations needed to be determined for each of the targeted cell lines. On average, perforation of 60-80% of the treated cells had to be achieved for satisfactory uptake results. Similarly, membrane resealing efficiencies needed to be on the same order to maintain high cell viability after toxin treatment[241]. As different cell lines possess different tolerance levels for bacterial toxins[242], SLO was initially dissolved in HBSS buffer at 10, 20 or 50 ng/mL concentrations, which corresponded to 14, 28 and 70 U/mL of catalytic activity. No toxin was present in mock-treated samples. First, the three-step SLO procedure was performed as described in *Materials and Methods*, without cargo proteins. As expected, all cell lines displayed variable vulnerabilities in response to the different toxin levels. HeLa cells proved to be most robust, whereas HEK cells showed the highest sensitivity to increasing toxin concentrations ***(Figure 21)***. From these results final concentrations of 50 ng/mL, 10 ng/mL, and 20 ng/mL of SLO for HeLa, HEK, and RCSN3 cells, respectively, were established as the most suitable toxin concentrations and subsequently used in all further uptake experiments. Under these conditions, 5-20 % of cell death was observed.

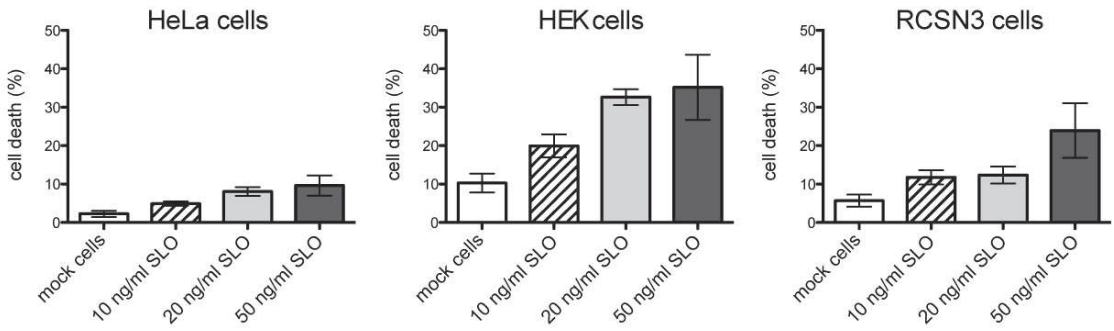

Figure 21: Optimization of SLO concentrations to be used for the different cell lines
Cell viability was tested for SLO toxin treatment studies with 10-20-50 ng/mL of the toxin, which corresponded to 14-28-70 U/mL of catalytic activity in the HeLa, HEK and RCSN3 cell samples. No SLO was added in trials of mock-treated cells. Cell death was assessed by flow cytometry by detection of the viability marker AAD 7. Graphs show mean values with SDs (n = 3).

2.1.3.2 Cell death and protein uptake using the SLO method

After these initial experiments, 50 µM of fluorescently labeled αSyn-Atto488 and GB1-Atto488 were applied onto HeLa, HEK and RCSN3 cells. The three-step SLO procedure was performed as previously described with optimized SLO concentrations for the different cell lines and in the presence of cargo proteins. 3-25% of cell death was observed in these SLO-mediated protein delivery approaches. The presence of cargo proteins did not promote higher levels of cell death. Protein uptake levels were comparable among the different cell lines. Highest uptake efficiencies were observed for HeLa cells, (~65-80 %), whereas lower uptake levels (~45-60 %) were measured for HEK and RCSN3 cells. No significant differences between the tested proteins were observed ***(Figure 22)***.

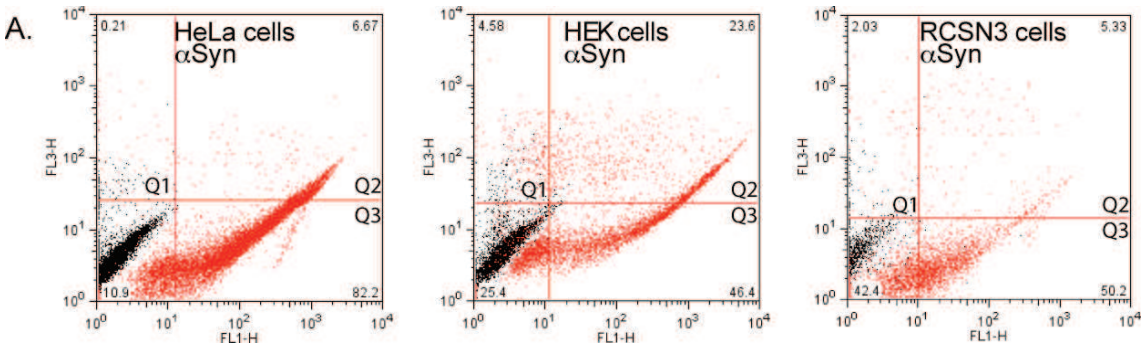

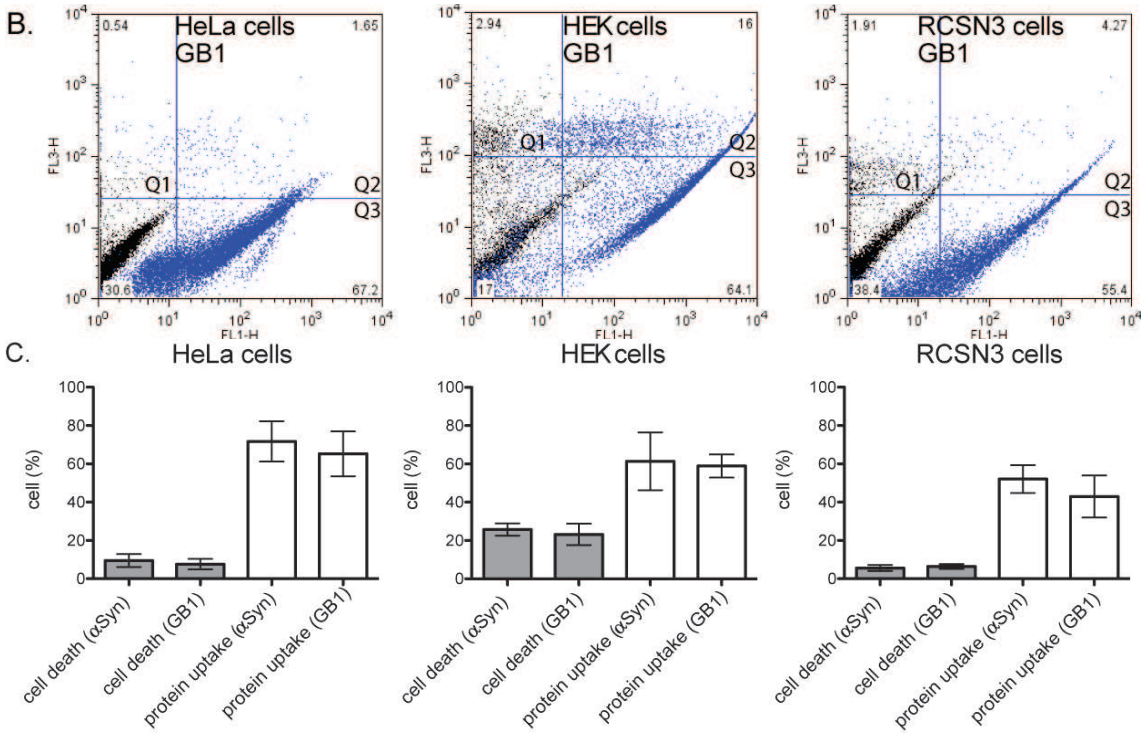

Figure 22: SLO-mediated delivery of αSyn and GB1

(A), (B) Flow cytometry dual channel analysis of mock (black), αSyn-Atto488 (red) and GB1-Atto488 (blue) treated cells. Analysis was performed by detection of AAD7 (cell viability) and Atto488. (C) Cell death and protein uptake of αSyn and GB1 by SLO-treatment. Graphs show mean values (n = 3) with SDs. 3-25% of cell death was detected among the different cell lines.

2.1.3.3 SLO - mediated protein delivery by DTT activated toxin treatment

Dithiothreitol (DTT) has been reported to further activate SLO via reducing its single cysteine residue[243]. However, addition of the reducing agent is not strictly required for SLO activity[12]. I performed SLO-mediated delivery assays with the two test proteins with, or without activation by 5 mM DTT. 50 µM of αSyn-Atto488 and histone H3-Atto488 (aa1-33) were delivered into HeLa and HEK cells by the use of optimized SLO concentrations. I observed a small (6-10%) increase in cellular uptake efficiencies, which was accompanied by a moderated increase in cell death (1-4%) ***(Figure 23)***.

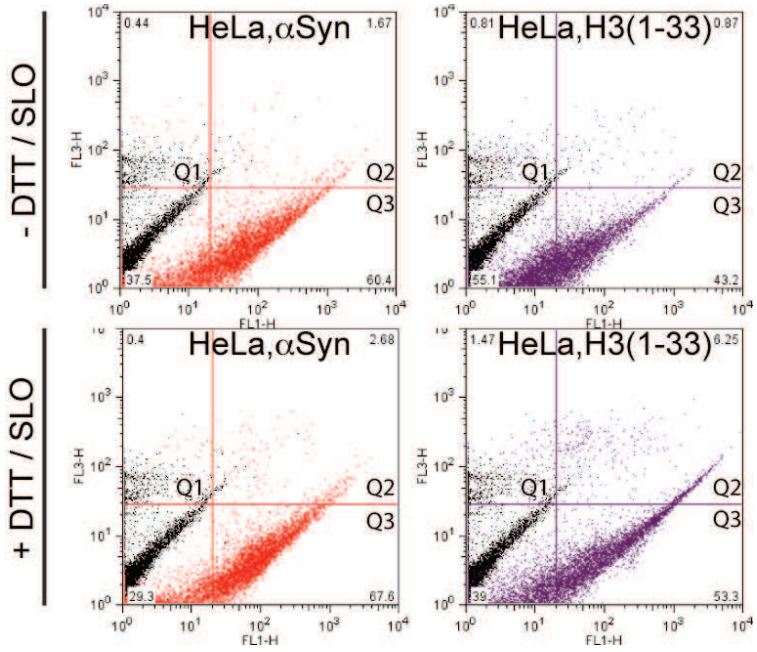

Figure 23: SLO-mediated delivery by DTT activated toxin
Dual channel flow cytometry analysis of mock (black), αSyn-Atto488 (red) and histone H3-Atto488 (purple). The toxin was applied without (top) or with (bottom) further activation by DTT.

2.1.3.4 Intracellular concentrations and distributions of SLO - delivered αSyn

As shown before, CPP-mediated delivery of αSyn resulted in low intracellular concentrations ***(Figure 20)***. To find out whether SLO-mediated protein delivery provided higher intracellular concentrations, cells were incubated with 50 µM of αSyn-Atto488. Intracellular protein concentrations were determined as average MFI values. Samples were processed in parallel and intracellular distributions were analyzed by live-cell confocal imaging. In comparison to the CPP-mediated delivery approach, higher MFI values were established for all the cell lines. The highest fluorescence signals were detected in HeLa cells (~80 MFI), whereas lower protein signals were noted for Neuro2a (~58 MFI) and RCSN3 cells (~23 MFI) ***(Figure 24)***. Confocal microscopy images revealed disperse but punctuated intracellular staining of the fluorescently labeled protein that was excluded from the cell nucleus.

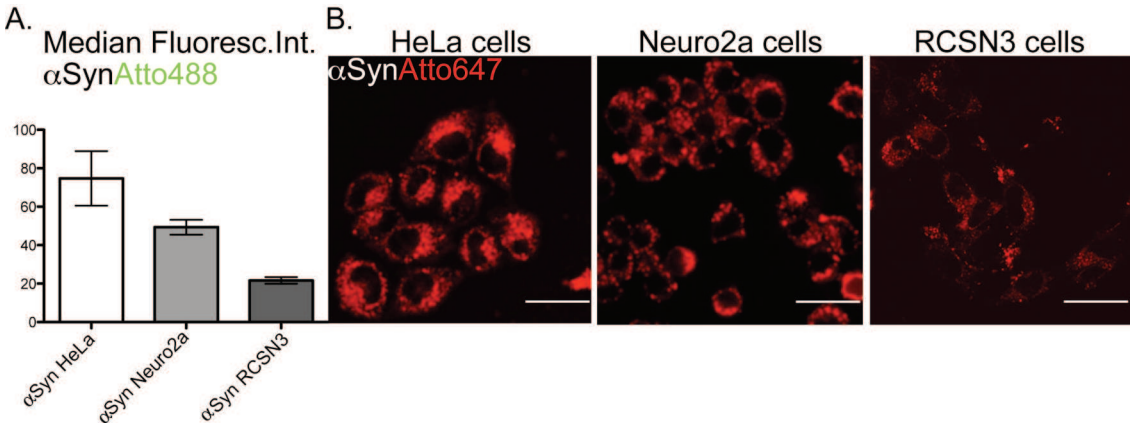

Figure 24: Intracellular concentrations and distributions of αSyn
(A) 50 µM of αSyn-Atto488 was added to cells for SLO-mediated uptake. MFI values of protein uptake are shown as bar graphs with SDs (n = 3). Highest, intermediate and lowest fluorescence intensities were observed for HeLa, Neuro2a and RCSN3 cells, respectively. (B) Live-cell confocal imaging of intracellular αSyn-Atto647.

2.1.4 Electroporation (EP) - mediated protein delivery

In the previous sections, I have described results from CPP- and SLO-mediated protein delivery assays. Both methods exhibited several drawbacks that limited their general suitability for *in-cell* NMR applications in mammalian cells. In the following section, I examine yet another protein transduction procedure: protein electroporation (EP). This method provides two main advantages over CPP- and SLO-mediated protein delivery. First, it does not require any forms of chemical modifications to proteins that are to be delivered and, second, it works without having to treat cells with potentially harmful toxins that generally lower cell viability.

2.1.4.1 Optimization of electroporation conditions

To best use the EP technique, several parameters needed to be optimized: Electroporation buffer conditions, EP pulse programs, number of EP-manipulated cells and recovery conditions. Previous experiments in our laboratory had shown that an iso-osmolar phosphate/HEPES electroporation buffer was best suited for the electroporation procedure. To evaluate the protein transduction efficiencies of different electroporation pulse programs, 3 recommended DNA electroporation programs were tested with αSyn-Atto488 on 14 different mammalian cell lines. Cell viability and protein uptake were measured and analyzed by dual channel flow cytometry. I found, that pulsing 4 million cells per reaction increased overall cell viability, but decreased

the amount of delivered protein that I detected in the cytoplasm. On average, electroporation of 2-3 million cells per reaction was found to be optimal with regard to protein uptake efficiency and cell viability. In the case of MCF7 and PC12 cells, lower cell numbers were used in each EP reaction, due to their enhanced propensities for cell-to-cell fusion. Recommended pulse programs and cell numbers are summarized in ***Table 2***.

Cell line	Cell number (10^6)	Amaxa program
A2780	2-3	B28
B65	2	G16
C6	2	G16
G261	2	G16
HeLa	2	B28
MCF7	1	B28
Neuro2a	2	T09

Cell line	Cell number (10^6)	Amaxa program
NIH-3T3	2	B28
PC12	1	T09
PC3	2	T013
RCSN3	2-3	G16
SH-SY5Y	2-3	G16
SK-N-SH	2-3	G16
U2OS	2	X001

Table 2: Summery of optimized pulse programs, and cell numbers for 14 mammalian cell lines.

Experiments showed that the total number of viable cells significantly decreased as a result of the electroporation process. This cell loss was attributed to cell lysis during the EP procedure and poor overall cell recovery. To improve these parameters, different recovery media were tested and cell loss monitored closely by counting viable and dead cells with a Trypan Blue staining protocol. HeLa, HEK and RCSN3 cells were tested in this way. After each round of the EP procedure, treated cells were transferred into different recovery media and counted after 30 min of recovery. To test whether different amounts of Ca^{2+} in the recovery media prevented or initiated higher incidents of apoptosis, commercial cell culturing media (1.5-1.8 mM Ca^{2+}), Opti-MEM (0.41 mM Ca^{2+}) and Ca^{2+}-free PBS solutions were compared. Both recovery media were supplemented with 10% of fetal bovine serum (FBS). I found that the EP procedure itself caused 15-30% of cell loss, which depended on the cell type. During the recovery time, further cell losses varied between 8-15% for the commercial cell culture medium and the Opti-MEM solution. Interestingly, higher cell loss (22-28%) ($P=0.025$, $P=0.0171$, $P=0.0217$ for HeLa, HEK and RCSN3 respectively)

occurred when cells were recovered in PBS ***(Figure 25, A)***. Further efforts were made to improve cell survival. To protect cells against metabolic exhaustion and oxidative stress during the EP process, they were manipulated in the presence of ATP and reduced glutathione (GSH). Furthermore, membrane resealing efficiencies were comparatively analyzed in recovery media that contained 0.5 mM of Poloxamer188, which had previously been reported to enhance cell viability in EP procedures[244,245]. Cell loss of electroporated HeLa cells was determined after 30 min recovery in the different cell culture media. Results showed that electroporation in the presence of ATP and GSH significantly lowered overall cell loss (P = 0.0378), whereas Poloxamer188 did not have a measurable influence on recovery efficiency ***(Figure 25, B)***.

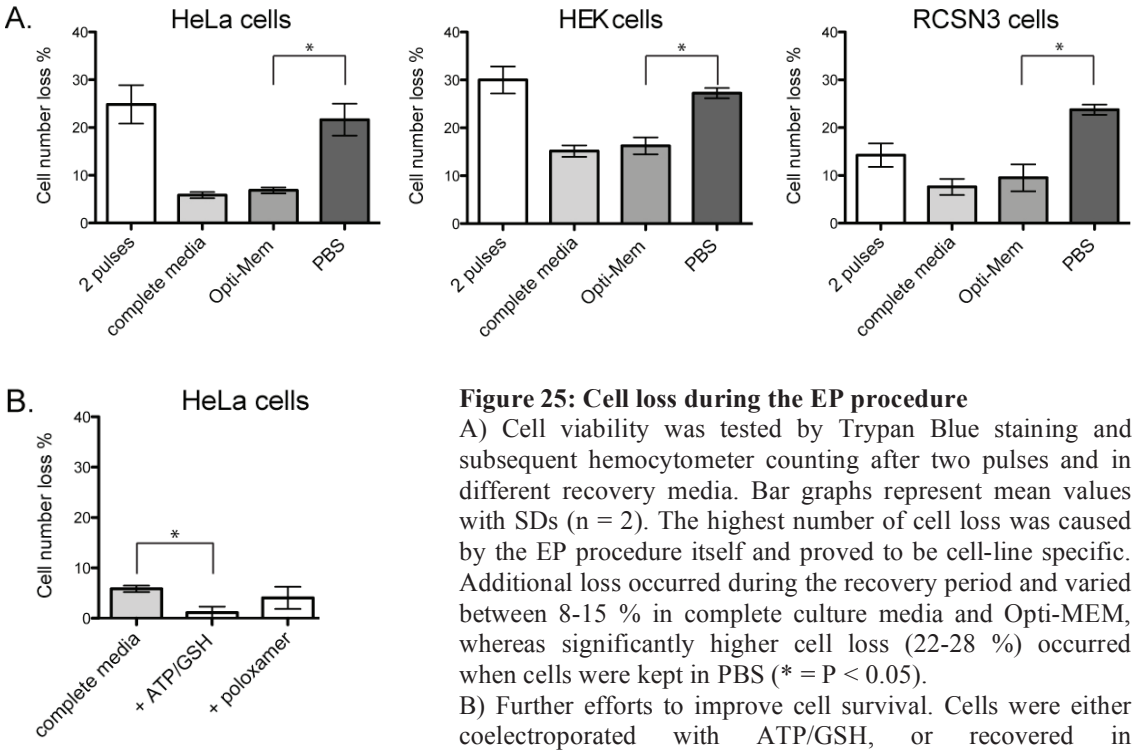

Figure 25: Cell loss during the EP procedure
A) Cell viability was tested by Trypan Blue staining and subsequent hemocytometer counting after two pulses and in different recovery media. Bar graphs represent mean values with SDs (n = 2). The highest number of cell loss was caused by the EP procedure itself and proved to be cell-line specific. Additional loss occurred during the recovery period and varied between 8-15 % in complete culture media and Opti-MEM, whereas significantly higher cell loss (22-28 %) occurred when cells were kept in PBS (* = $P < 0.05$).
B) Further efforts to improve cell survival. Cells were either coelectroporated with ATP/GSH, or recovered in Poloxamer188 containing media. Electroporation in the presence of ATP/GSH significantly lowered cell loss whereas Poloxamer188 did not improve the recovery efficiency (* = $P < 0.05$).

In a next step, I assessed the effects of using multiple EP pulses on overall cell viability. Although higher numbers of EP pulses were reported to increase the proportions of dead cells in EP mixtures, it had also been shown to result in enhanced levels of EP-mediated protein delivery[129]. To evaluate whether this was also the case for the experimental conditions that I had chosen, I electroporated HeLa, HEK and RCSN3 cells with 1, 2 or 3 EP pulses. I found that higher number of pulses led to

increased cell death in all tested cell lines. HEK cells showed the highest sensitivity, whereas RCSN3 cells proved to be the most robust ***(Figure 26)***. Cell viability altered between ~4-18% among the different cell lines when two EP pulses were applied.

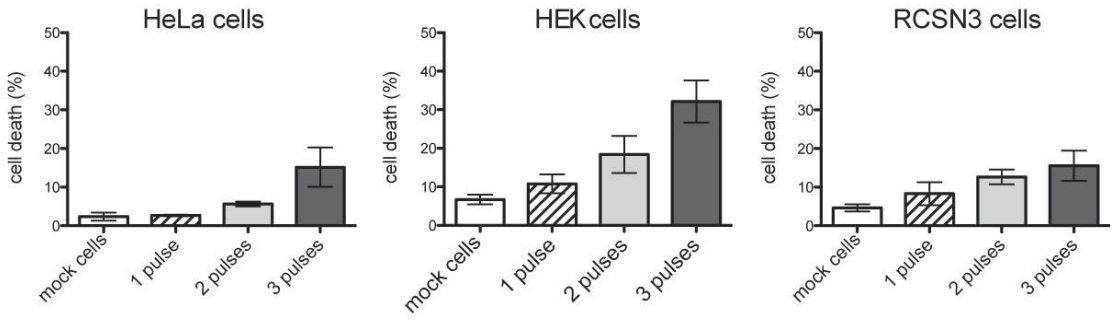

Figure 26: Effects of multiple EP pulses on overall cell viability
Electroporation of HeLa, HEK and RCSN3 cells with 1, 2 or 3 EP pulses. Cell death was assessed by flow cytometry and usage of the viability marker AAD7. Graphs indicate mean values (n = 3) with SDs.

In a second step, I electroporated HeLa cells with increasing numbers of EP pulses (1-3) to deliver 50 µM of αSyn-Atto488 to check whether multiple pulses influenced protein uptake efficiencies and intracellular protein concentrations. These experiments revealed that multiple EP pulses resulted in increased cell death, but did not significantly change protein uptake efficiencies ***(Figure 27, A)***. Slightly larger MFI values for the 3 pulse samples were detected thus indicating marginally higher intracellular protein concentrations in the surviving cell populations ***(Figure 27, B)***.

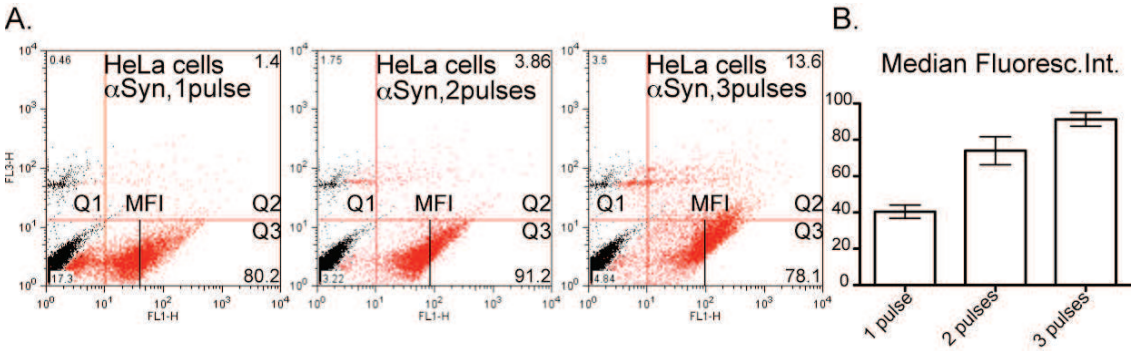

Figure 27: Effects of multiply pulses on intracellular protein concentrations
(A) Dot plot representation of EP-mediated αSyn-Atto488 delivery (red) into HeLa cells by multiple pulses. Increased cell death but no significant differences in protein uptake efficiencies were detected. (B) Bar graphs represent mean values (n=2) with SDs.

2.1.4.2 Protein uptake and cell death using the EP method

After these pilot experiments, EP-mediated delivery of 50 µM αSyn-Atto488 and GB1-Atto488 was carried out with two pulses on 2 million HeLa, HEK and RCSN3 cells. 4-22% of cell death was detected. In comparison to the pilot experiments, addition of the cargo proteins did not promote higher levels of cell death. Very promising transduction efficiencies (~60-80%) were observed for all the tested cell lines, with no significant differences between the tested proteins ***(Figure 28)***.

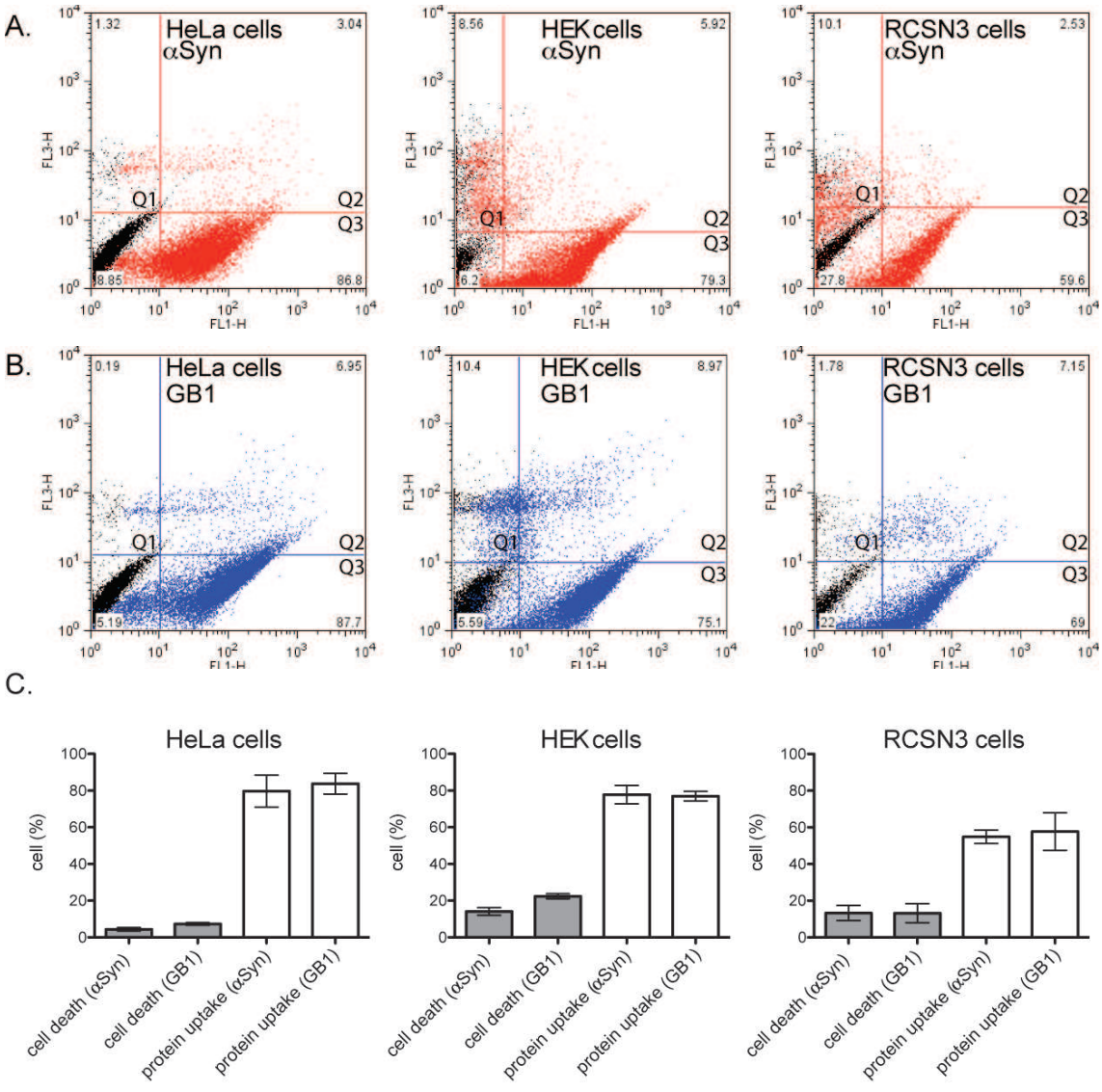

Figure 28: EP-mediated αSyn and GB1 delivery
(A), (B) Flow cytometry dual channel analysis of mock (black), αSyn-Atto488 (red) and GB1-Atto488 (blue) delivery by EP. Analysis was performed by detection of AAD7 (cell viability) and the Atto488 signals). (C) Cell death and protein uptake of αSyn and GB1 by EP. Graphs show mean values (n = 3) with SDs.

To eventually prepare high quality *in-cell* NMR samples, I needed to ensure that viable cells carrying intracellular proteins were properly separated from dead cells. As the EP protocol is executed on adherent cells that are put into suspension by mild Trypsin treatment before they are electroporated, the cellular propensities for reattachment could be exploited to select for highly viable cells. Reattachment of electroporated cells was ensured by extended recovery times during which the manipulated cells were transferred into culture flasks and returned to the CO_2-incubator. Following a 5 h recovery period, two types of cell populations were noted by bright-field light microscopy: Cells that were not attached and remained floating in the supernatant of the culture media and cells that had perfectly reattached and fully regained their individual morphologies. Overall cell viability of these two populations was separately evaluated by flow cytometry and AA7D staining (see below). The recovery properties of 14 different mammalian cell lines were independently assessed by this procedure. For this, reattached cell populations were extensively washed, harvested by 0.25% Trypsin/EDTA treatment and processed for hemocytometer-based cell counting. Additional collagen coating of the cell culture flasks improved the reattachment propensities of certain cell lines. Results are shown in ***Table 3***.

Cell line	Recovery	Remarks
A2780	~ 25-30%	Higher cell loss
B65	~ 60%	Fast recovery
C6	~ 60%	Fast recovery
G261	~ 50%	Fast recovery
HeLa	~ 40-50%	Fast recovery
MCF7	~ 50%	Collagen coat
Neuro2a	~ 50%	Collagen coat

Cell line	Recovery	Remarks
NIH-3T3	~ 30%	Collagen coat
PC12	~ 80%	Collagen coat
PC3	~ 40%	Collagen coat
RCSN3	~ 60%	Fast recovery
SH-SY5Y	~ 15-20%	Collagen coat
SK-N-SH	~ 20-30%	Collagen coat
U2OS	~ 60%	Fast recovery

Table 3: % of recovered viable cells after the reattachment period
Hemocytometer counts on 2x EP pulsed cells after re-attachment, thorough washing and Trypsin harvesting.

2.1.4.3 Cell morphology and viability

Possible cytopathological changes (swelling, blebbing, or fraying of cell membranes) in the morphology of electroporated NMR cell models (A2780, HeLa, B65, RCSN3, SK-N-SH) were followed by phase-contrast light microscopy. Cells were

electroporated with 400 μM αSyn and plated back onto cell culture flasks for recovery. The recovery process was evaluated over 1-5 hours post-electroporation. Non-pulsed control cells were plated in parallel and evaluated after 5 hours. Most cell lines reattached within one hour after the reseeding step and began to regain their individual morphologies within 2 hours. Among the tested cell lines tested, RCSN3 cells recovered the fastest, whereas A2780 cells recovered the slowest. After 4-5 hours all cell lines had perfectly regained their original morphologies ***(Figure 29)***. As has been shown previously, ~15-30% of the starting cell numbers were lost ***(Figure 25)***. Cell debris and dead cells were removed in the recovery and washing steps ***(Figure 29)***.

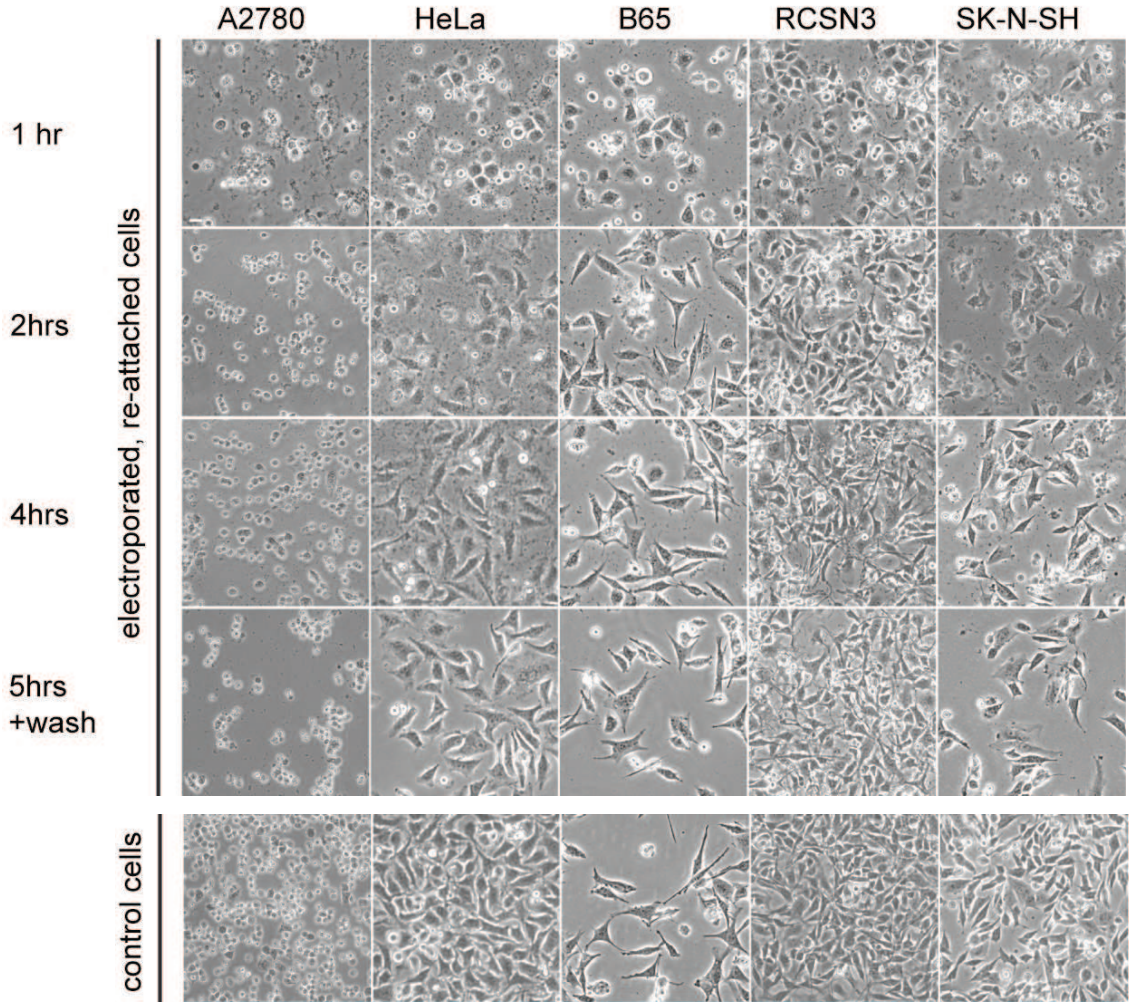

Figure 29: Reseeding, recovery and morphology of EP-treated cells
Regained morphology of the NMR cell models 1-5 hrs after electroporation, as observed by phase-contrast light microscopy. Control cells plated in parallel with the electroporated cells are shown after 5 hrs. Scale bar = 60 μm.

To evaluate whether cells that did not reattach during the recovery period displayed measurably higher levels of cell death, I EP-delivered αSyn-Atto488 and p53-Atto488 (aa1-64) into PC3 cells and allowed the cells to recover for 5 hours. Cell viability measurements of attached and non-attached cell populations revealed that attached cells showed very low numbers of dead cells (~3-6%) ***(Figure 30, top)***, whereas cells that did not attach during this recovery period contained a much larger proportion of dead cells (~25-40%) ***(Figure 30, bottom)***. Both populations exhibited similar levels of delivered, intracellular protein, which was indicated by the determined MFI values ***(Figure 30)***.

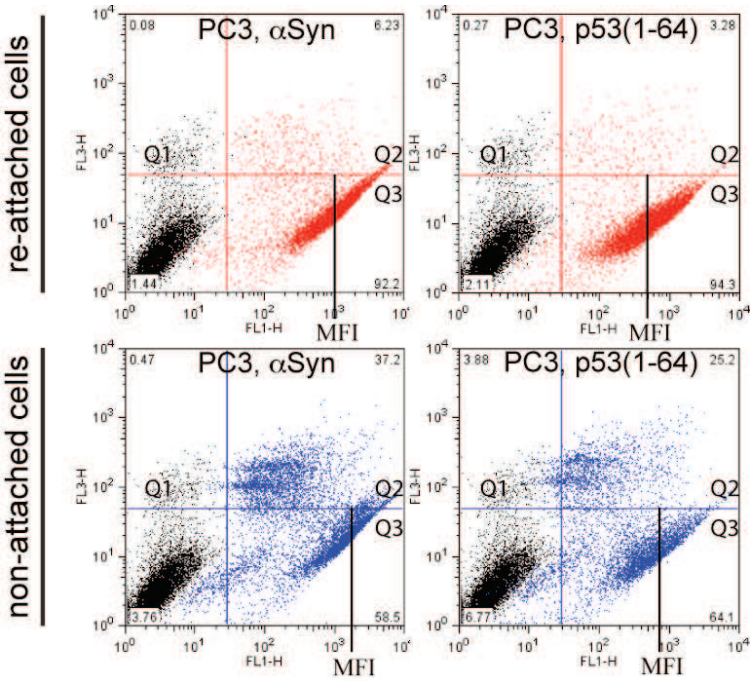

Figure 30: Viability of attached and non attached cell populations after 5 hrs of recovery
Dual channel flow cytometry analysis of mock (black), αSyn-Atto488 and p53(1-64)-Atto488 targeted PC3 cells. Attached (top, red) and non-attached cell populations (bottom, blue) were analyzed in with AAD7. High percentage of dead cells were present in the non-attached cells population, whereas both populations (attached and non-attached) contained similar levels of intracellular proteins.

2.1.4.4 Intracellular concentrations and distributions of EP - delivered αSyn

To directly compare the intracellular protein levels that could be achieved by EP- and SLO-mediated delivery schemes, I electroporated 50 µM of αSyn-Atto488 into HeLa, Neuro2a and RCSN3 cells. Identical samples were prepared with HeLa and RCSN3 cells for confocal analysis to investigate intracellular protein distributions. For all cell lines, higher MFI values were observed in EP-treated samples than for SLO-mediated delivery. The highest intracellular protein concentrations were detected in

Neuro2a cells (~150 MFI), followed by HeLa (~90 MFI) and RCSN3 cells (~50 MFI) ***(Figure 31, A)***. Delivered protein displayed cytoplasmic and nuclear distributions, with moderate levels of punctuated vesicle staining ***(Figure 31, B)***.

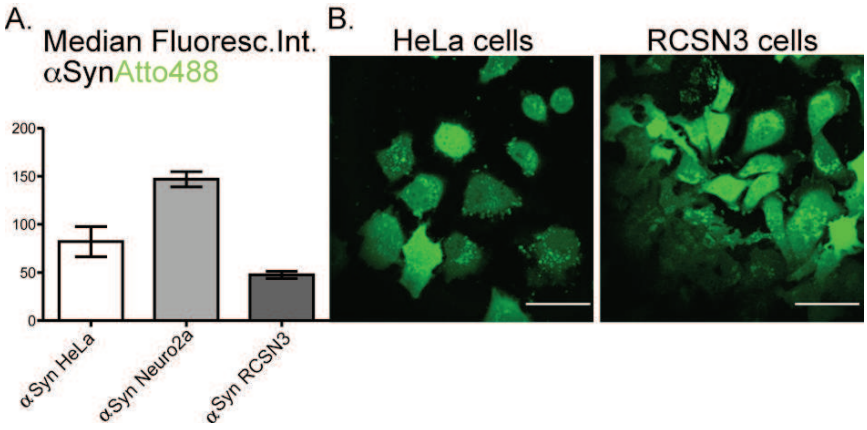

Figure 31: Intracellular concentrations and distributions of EP-delivered αSyn
(A) 50 µM of αSyn-Atto488 was delivered by EP and cells were analyzed by flow cytometry. Median fluorescence intensity values (MFI) of viable and protein positive cells are shown as bar graphs with SDs (n = 3). High fluorescence intensities were observed in HeLa and Neuro2a cells. (B) Live confocal imaging of intracellular αSyn-Atto488 distributions. Scale bar= 50 µm.

2.1.5 Comparison of CPP-, SLO-, and EP - mediated protein delivery methods

2.1.5.1 Cell death, cellular protein uptake and intracellular concentrations

The following conclusions were drawn from these comparative experiments: First, small differences in cytotoxicity were observed with the three different delivery methods. Differences in cell death levels were primarily influenced by cell type, with HEK cells showing the highest sensitivity in all cases. Second, protein uptake levels also displayed a high cell type dependency. Relatively low levels of intracellular protein concentrations were generally achieved with CPP-mediated delivery protocols. Both SLO-mediated delivery and protein EP outperformed CPP-mediated approaches in all instances. Comparable transduction levels were obtained with SLO-and EP methods, except for RCSN3 cells, which displayed lower transduction efficiencies with the SLO approach. MFI values were comparable only for HeLa cells, while higher intracellular levels of delivered proteins were achieved by EP procedures on RCSN3 and Neuro2a cells.

2.1.5.2 Titration experiments using SLO - and EP - delivery methods

To further compare the suitability of SLO- and EP-mediated delivery procedures, αSyn-Atto488 titration experiments were performed with HeLa and Neuro2a cells. Increasing amounts of protein (50-200 µM) were delivered by SLO and EP procedures. For the SLO-mediated delivery approach, the percentage of positively targeted cells (i.e. cell uptake %), as well as MFI values reached a plateau at 100 µM of applied protein ***(Figure 32, A)***. In contrast, the EP method scored consistently higher in the number of targeted cells and MFI values linearly increased with higher protein concentrations ***(Figure 32, B)***. Therefore, higher intracellular protein concentrations could be reached with EP.

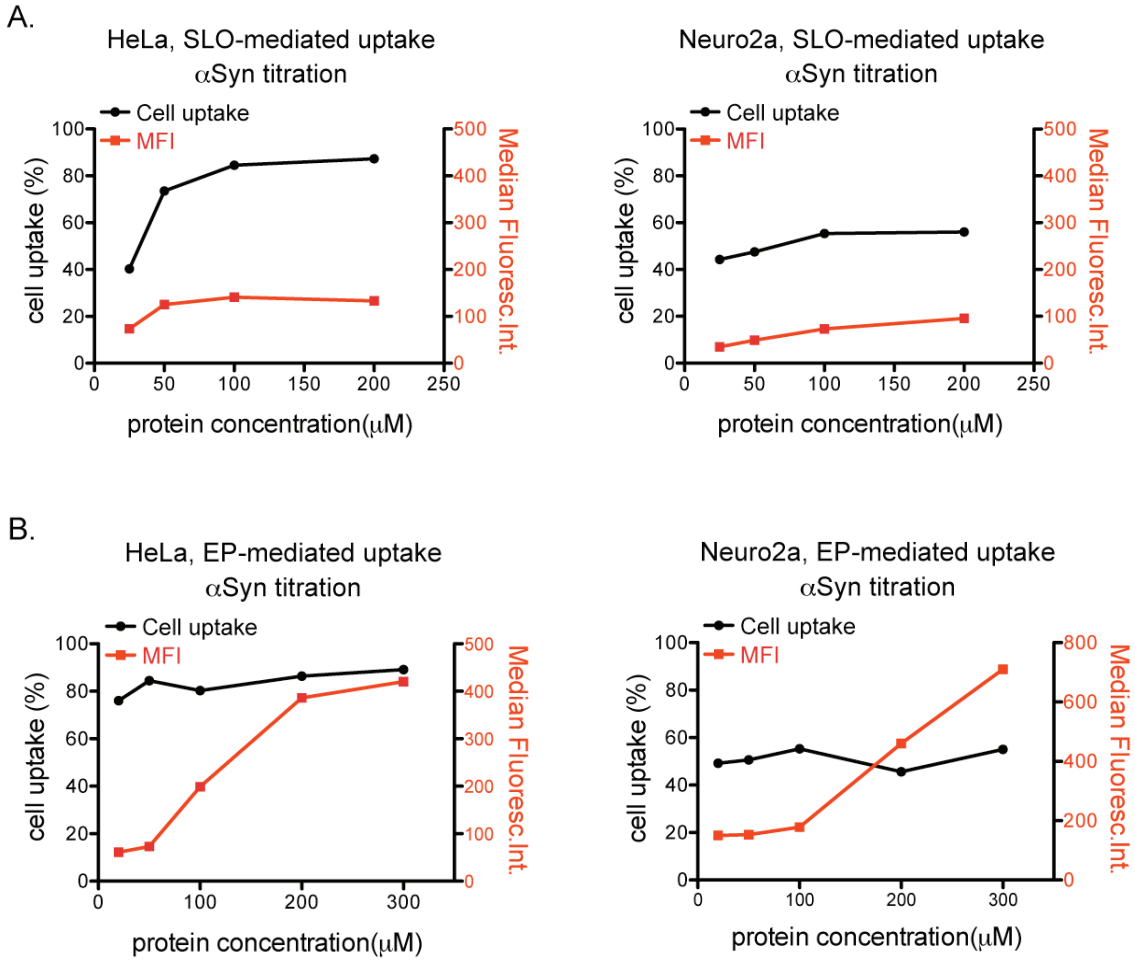

Figure 32: SLO- and EP-mediated protein uptake
Dual channel flow cytometry analysis of cellular protein uptake (left axis, black curve) and median fluorescence intensities (right axis, red curve) for SLO- (A) and EP-methods (B) on HeLa and Neuro2a cells. Uptake of αSyn-Atto488 was tested at 50-200 µM, or 50-300 µM concentrations of applied protein, respectively.

In summary, protein delivery by EP proved to constitute the most suitable approach for the preparation of mammalian *in-cell* NMR samples.

2.1.6 Range of applications of the EP method

Up until now, only a limited number of protein substrates were tested in the different delivery approaches. To evaluate the general robustness of the EP method, several additional peptides and proteins were transduced into mammalian cells ***(Figure 33)***. To this end, I sampled the widest possible range of protein sizes and charge distributions (i.e. isoelectric points, pI's). Although no further investigations were performed on these proteins and peptides, good overall transduction efficiencies were achieved in all cases.

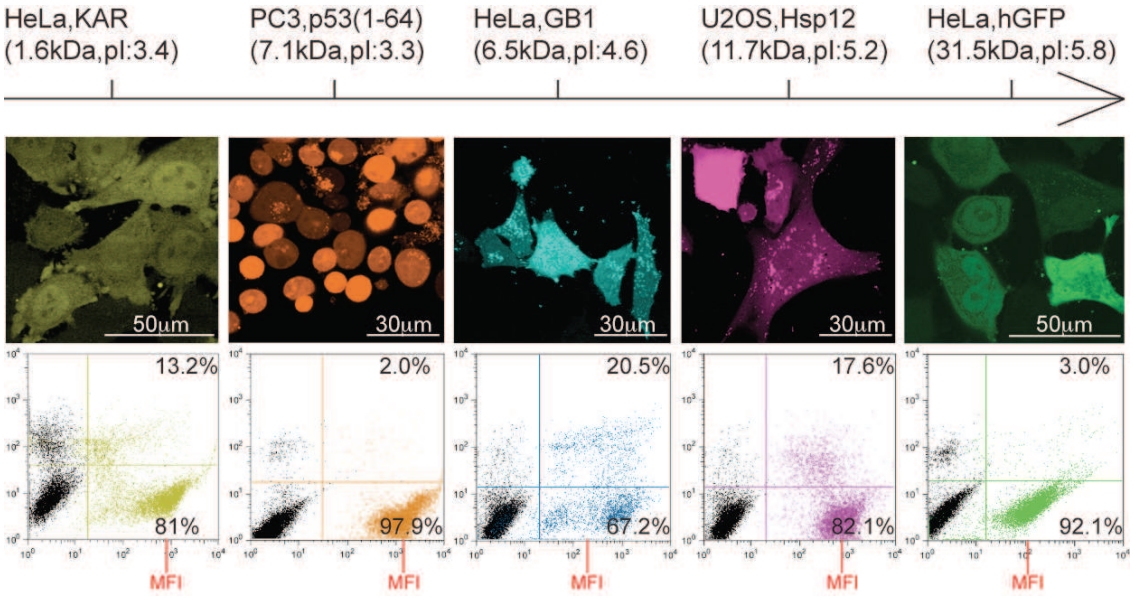

Figure 33: EP of other proteins/peptides
Live-cell imaging (top) and flow cytometry analysis (bottom) of electroporated cells.

To determine whether proteins of larger sizes could also be delivered by the EP technique, I set out to deliver αSyn fibrils[23] into HeLa cells. These fibrils had diameters of ~20 nm and lengths of 500 µm (S. Verzini, unpublished data) ***(Figure 34, A)***. I performed, small-scale electroporation trials with 250 µM of monomeric and fibrillar αSyn and HeLa cells. In comparison to monomeric αSyn (M), a much poorer overall cell recovery of fibril (F) electroporated cells was observed (i.e. low numbers of attached cells during the recovery period) ***(Figure 34, B)***. After 5 hours of recovery,

both attached and non-attached cells were harvested and lysed. 30 µg of the soluble lysates were loaded onto a native PAGE, transferred onto PVDF membranes and analyzed by Western blotting. Lower intracellular levels of αSyn fibrils were detected. In addition, substantial amounts of aggregated and partially degraded αSyn species were detected in the non-attached cell populations ***(Figure 34, C)***.

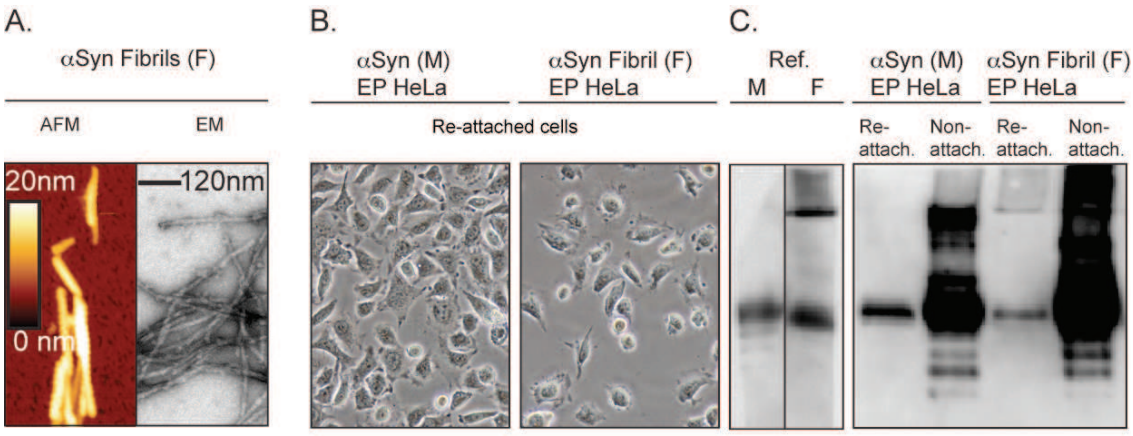

Figure 34: Electroporation of αSyn monomers and fibrils into HeLa cells
A) AFM and EM characterization of αSyn fibrils (image, courtesy of S. Verzini) B) Cell recovery after electroporation. C) Western blot analysis of electroporated cells

2.2 Part 2: Mammalian *in-cell* NMR of αSyn

Until now, I had used αSyn as a model protein to compare the suitability of different delivery methods for generating mammalian *in-cell* NMR samples. However, this choice was deliberate, as one of the specific aims of this thesis was to investigate the structural and dynamic features of this protein in different mammalian cellular environments, since intracellular aggregation of αSyn and its amyloid forming propensities are strongly related to the pathogenesis of Parkinson disease (PD)[190, 197]. PD is the second most common neurodegenerative disorder, caused by selective cell death dopaminergic neurons of the *substantia nigra*[20]. Therefore, the extended aim of this study was to delineate a first time characterization of the intracellular behaviors of αSyn in physiologically relevant environments. With this in mind, projected *in-cell* NMR analyses of αSyn in cells of non-neuronal origin i.e. A2780 and HeLa cells were meant to delineate non-disease relevant reference states of the intracellular behavior of this protein. *In-cell* NMR investigations in the dopaminergic neuronal B65, SK-N-SH and especially RCSN3[21] cells, were then meant to provide information about structural and functional alterations that are disease-relevant.

2.2.1 Endogenous αSyn levels in *in-cell* NMR cell models

For *in-cell* NMR measurements in mammalian cells, recombinantly expressed ^{15}N isotope-labeled αSyn was delivered into each of the five cell lines. To evaluate the relative amounts of successfully delivered exogenous protein, I first had to determine the relative levels of endogenous αSyn. I employed a recently published αSyn immunoblotting protocol[246] to identify endogenous αSyn in cell lysates of each cell line. According to this protocol, highly concentrated cell lysates are used (200 µg total protein) and PVDF membranes are fixed with 4 % PFA prior to immunoblotting with monoclonal, anti-full length (FL) αSyn antibodies. Surprisingly, monomeric αSyn at its expected molecular size of ~14 kDa was only detected in the three human cell lines (i.e. in A2780, HeLa and SK-N-SH cells), whereas the αSyn-specific antibody picked up a higher molecular weight protein species (~42 kDa, indicated with an asterisk) in rat B65 and RCSN3 cells ***(Figure 35, A)***. Earlier studies had identified three alternatively spliced isoforms of αSyn in rat brains[247, 248], with one of them having an apparent molecular weight of 42 kDa. To confirm that the detected high molecular weight

signals that I had detected in B65 and RCSN3 cells corresponded to this rat isoform of αSyn and not to a non-covalently aggregated form of the protein, I re-analyzed the different lysate samples after extensive boiling. This procedure did not influence the migration properties of the high and low molecular weight species ***(Figure 35, B)***. The αSyn degradation band in HeLa cells (**) will be discussed later in the text ***(Figures 59-60)***. In conclusion, all tested cell lines displayed low levels of endogenous αSyn.

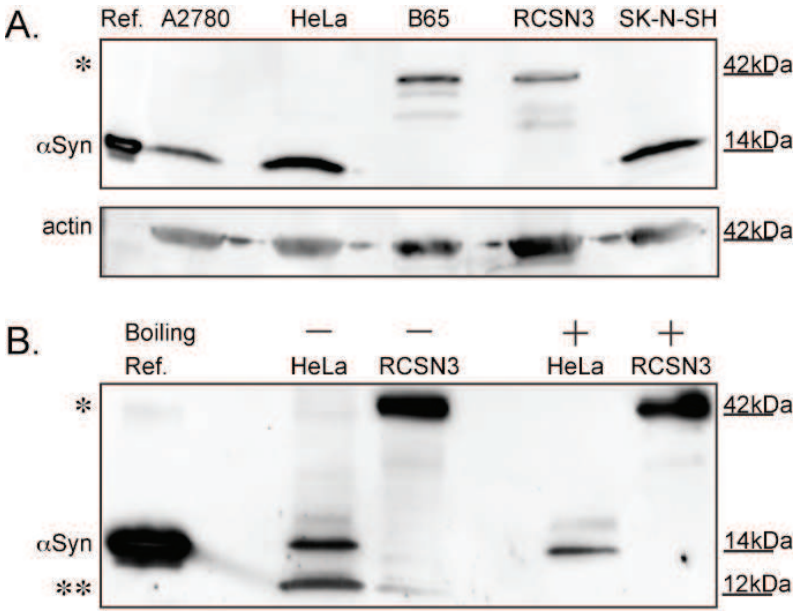

Figure 35: Endogenous levels of αSyn in different cell lines
A) Western blot analysis of αSyn. 200 µg of soluble cell lysates were separated by SDS-PAGE. Monomeric αSyn (~14 kDa) was detected in human A2780, HeLa and SK-N-SH cells. A high molecular weight species (*) (~42 kDa) was detected in B65 and RCSN3 cells, which likely corresponded to a rat-specific isoform of αSyn[247,248]. B) Western blot analysis of αSyn cell lysates before and after boiling.

2.2.2 αSyn concentrations for NMR experiments

In the first part of this study, I determined that protein electroporation constituted the most suitable method to deliver proteins into mammalian cells. As a next step, I set out to optimize the EP procedure for intracellular delivery of ^{15}N isotope-labeled αSyn for *in-cell* NMR measurements. Because NMR spectroscopy is a rather insensitive method, I initially tested conditions to deliver the highest possible amounts of recombinant αSyn, without adverse cytotoxicity effects. Based on my previous findings, the levels of delivered, intracellular proteins were directly proportional to their concentrations in the electroporation mixtures ***(Figure 32)***.

Therefore, I performed initial titration experiments with increasing amounts of isotope-labeled αSyn. MFI values in 5 different cell types that I electroporated with 200-800 µM of αSyn-Atto488 were analyzed by flow cytometry. As expected, they showed a linear increase with progressively larger αSyn concentrations in the EP mixtures. Cell type-dependent differences in uptake efficiencies, as reported previously for the initial trial studies, were similarly detected ***(Figure 36, A)***. Increased levels of cell death were observed with higher protein concentrations ***(Figure 36, B)***. To maintain high cell viability, EP procedures with maximal stock concentrations of 400 µM of αSyn were chosen in all further experiments.

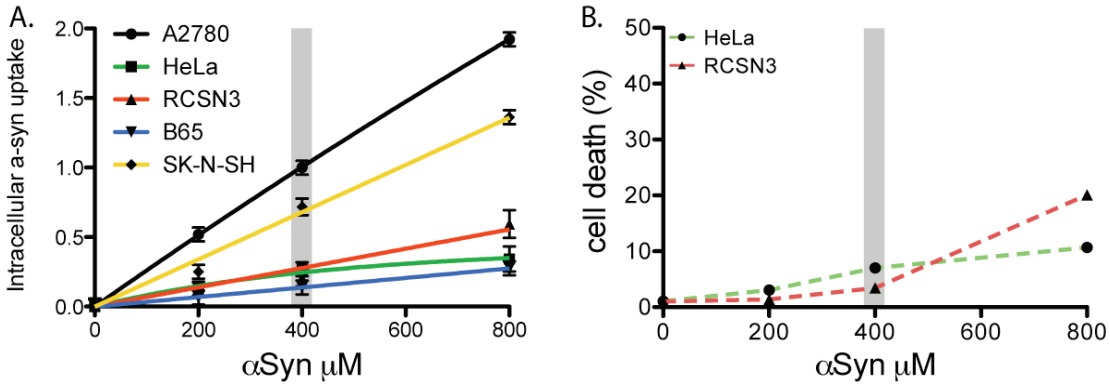

Figure 36: Optimization of αSyn concentrations for mammalian *in-cell* NMR samples
(A) Electroporation of 200-800 µM of αSyn-Atto488 into 5 different cell types. Median fluorescence values (MFI) were measured by flow cytometry and plotted against αSyn concentrations. Values were corrected for the individual cell volumes. Cell-line dependent differences in MFI values were detected Mean values are shown with SDs, n = 2. (B) Cell viability of HeLa and RCSN3 cells was assessed by ADD7 staining and quantitative analysis.

I also assessed cell viability and overall protein uptake for cells that had been electroporated with 400 µM of αSyn-Atto488. High overall cell viability (> 95%) and protein uptake efficiencies (> 97%) were detected, as was apparent from the respective flow cytometry scatter plots ***(Figure 37)***.

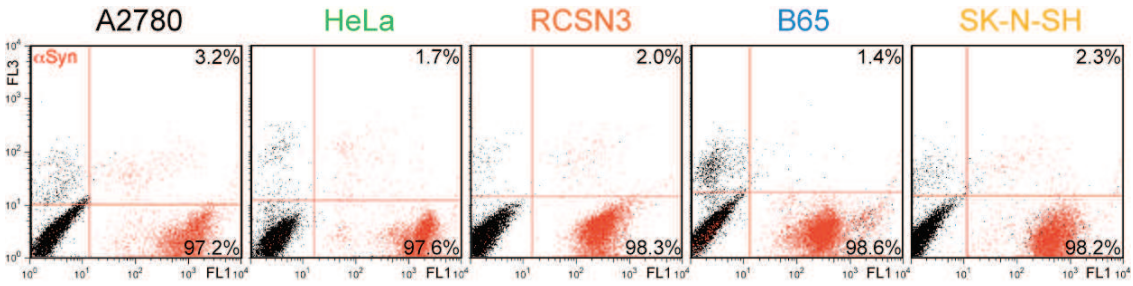

Figure 37: Electroporation of 400 µM of αSyn-Atto488.
Cell viability and protein uptake of 400 µM αSyn-Atto488 (x axis) and AAD7 staining (y axis) in 5 different mammalian cell lines.

Because structural changes of members of the *Synuclein* protein family strongly correlate with aggregation propensities, I also tested the EP delivery efficiencies of β-, and γSyn. To this end, I determined cell viability and protein uptake in samples of B65 cells that I electroporated with 400 µM of β- and γSyn-Atto488. The results indicated high overall cell viability and uptake properties that were comparable to αSyn ***(Figure 38)***.

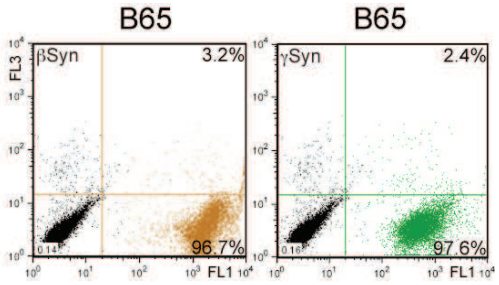

Figure 38: Electroporation of B65 cells with 400 of µM β–, and γSyn-Atto488.

2.2.3 Intracellular αSyn concentrations

Up to now, semi-quantitative MFI values were used as a proxy for the absolute amounts of delivered proteins. However, a more quantitative analysis of intracellular protein concentrations is required for accurate *in-cell* NMR analyses. This, because of two reasons: First, intracellular concentrations ($C_{int.}$) of delivered proteins must be compared to the physiological levels of endogenous αSyn in neuronal cells, or at pre-synaptic terminals[249], so as to establish the physiological relevance of the created *in-cell* NMR samples. Second, precise knowledge about intracellular protein concentrations enables quantitative deductions of effective NMR concentrations that are to be expected for each *in-cell* NMR sample. These concentrations, and whether

they are really detected by NMR spectroscopy, will determine how many of the delivered isotope-labeled protein molecules actually contribute to the NMR signal. The effective NMR concentration will be significantly lower than the intracellular protein concentration, simply because intracellular cell volumes do not translate into the packing volumes of intact cells. The result packing defects must be quantified accurately in order to derive meaningful estimates for effective NMR concentrations. Comparisons of expected and actually measured NMR signal intensities will provide important information about the extent of intracellular αSyn aggregation, membrane binding, degradation or other intracellular events that result in NMR signal deterioration. To accurately determine absolute intracellular concentrations of αSyn, small-scale experiments were carried out on 2 million cells that had been electroporated with 400 µM of αSyn. Recovered cells were washed, 0.25 % Trypsin/EDTA harvested and counted. Lysates were prepared by treatment with RIPA buffer and the soluble cell fraction from 0.13 million cells (N_{cell}) were separated on a gradient (4-18 %) SDS-PAGE. A reference series of 10-400 ng of recombinant αSyn was used to generate a calibration curve. The samples were transferred onto a PVDF membrane and αSyn was detected by Western blotting. Chemiluminescence signal intensities were quantified using the ImageLab software. Equal sample loading was confirmed via an actin loading control ***(Figure 39, A)***. Protein concentrations in the cell lyates (C_{lysate}) were determined from chemiluminescence signal intensities of intracellular αSyn in reference to the calibration curve ***(Figure 39, B)***. C_{lysate} values were converted into intracellular concentrations (C_{int}) by the use of dilution factor ($f = V_{lysate} / V_{cell\ total}$) of cells within the lysate (V_{lysate}). Total volumes of the cells ($V_{cell\ total}$) used for lysate preparations were calculated from the number of cells used and the average cell volumes. Average cell volumes were measured using a CASY Model TT cell analyzer with a 60 µmeter capillary ***(Figure 39, C)***. Intracellular αSyn concentrations inside the 5 electroporated cell types were calculated from two independent experiments ***(Figure 39, D)***. For more detailers see *Materials and Methods: Estimation of intracellular αSyn concentrations.*

Cell volume analysis revealed, that HeLa and B65 cells contained large intracellular cell volumes (~2-3 pL), whereas A2780, SK-N-SH and RCSN3 had smaller volumes (~0.6-1 pL). Calculated intracellular αSyn concentrations varied between 20-120 µM,

depending of the cell types. Intracellular concentrations were in the physiological range of αSyn at pre-synaptic termini[249].

A.

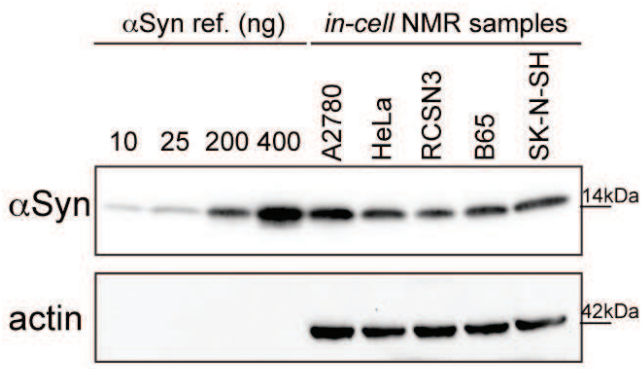

B.

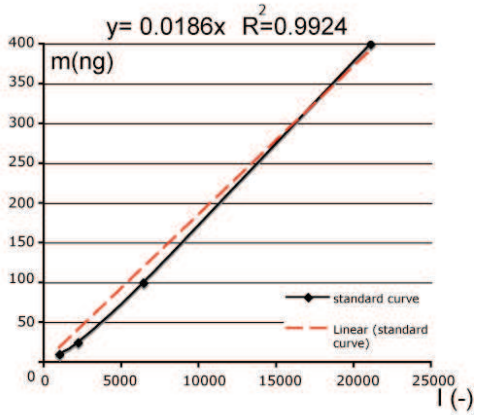

C.

Cell line	Mean cell volume (pL)	SD (pL)
A2780	1.1	0.6
HeLa	2.9	0.5
RCSN3	0.8	0.4
B65	2.3	1.3
SK-N-SH	0.6	0.3

D.

Cell line	Mean intrac. conc. (μM)	SD (μM)
A2780	88.8	6.8
HeLa	21.7	1.0
RCSN3	39.8	12.1
B65	27.0	3.3
SK-N-SH	118.5	11.5

Figure 39: Intracellular concentrations of αSyn
(A) 0.13 million cells (N_{cell}) per sample were loaded onto a gradient (4-18 %) SDS-PAGE. 10-400 ng of a recombinant αSyn reference series was used to generate the calibration curve. (B) Levels of αSyn were determined from the detected chemiluminescence signal (I), in reference to the calibration curve. Calibration curve and linear fitting (equation and R^2) shown on top. (C) The volume of a single cell was determined with a CASY Model TT cell analyzer (D) Intracellular protein concentrations of 400 μM electroporated αSyn. For (C) and (D) mean values are given with SDs, n = 2.

2.2.4 Calculating effective *in-cell* NMR concentrations

To determine αSyn concentrations in the NMR samples (effective NMR concentrations, C_{eff}), a dilution factor was applied to the intracellular αSyn concentration, as determined previously by Western blotting. Dilution factors were calculated from $N_{cell\ NMR}$ the number of cells within the NMR receiver coil, multiplied by V_{cell} the volume of a single cell determined by the CASY cell analyzer and divided by $V_{pellet\ NMR}$ the volume of the cell pellet within the NMR receiver coil volume.

Expected αSyn NMR concentrations of the 5 electroporated cell models, calculated from two independent experiments are given in ***Figure 40***. These results demonstrate that the cell volumes and packing volumes were cell-line specific.

Cell line	Expected NMR conc. (μM)	SD (μM)
A2780	12.6	2.0
HeLa	5.3	0.5
RCSN3	2.6	1.1
B65	4.4	1.5
SK-N-SH	9.6	0.3

Figure 40: Expected NMR concentrations of αSyn electroporated *in-cell* NMR samples
In order to calculate effective NMR concentration, dilution factor was applied to the intracellular concentrations determined earlier. Mean values are given with SDs, n = 2.

2.2.5 Intracellular distributions of electroporated *Synuclein*s

Whereas endogenous αSyn localizes to synaptic vesicles[161], over-expressed *Synuclein* proteins have been found in the neuronal stroma, the cell nucleus[167, 250] and at mitochondrial membranes[169, 251]. To determine the intracellular localization of EP-delivered αSyn, cells were immunostained following PFA fixation and Triton-X permeabilization. Anti-full length αSyn, anti-N-terminal αSyn, and anti-γSyn antibodies were used for αSyn-, βSyn-, and γSyn detection, respectively. Nuclear DNA was visualized by Hoechst staining. These experiments indicated that the members of the *Synuclein* family were primarily found in the cytoplasmic compartment, but also, partially, in cell nuclei. The uniform cytoplasmic staining did not indicate significant propensities for membrane association, or co-localization with intracellular vesicles ***(Figure 41)***.

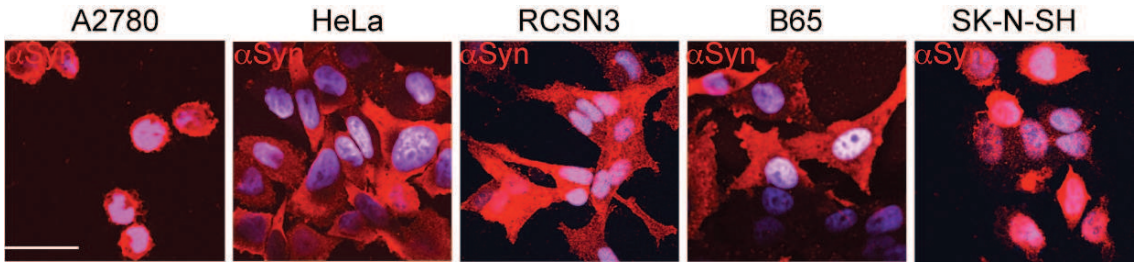

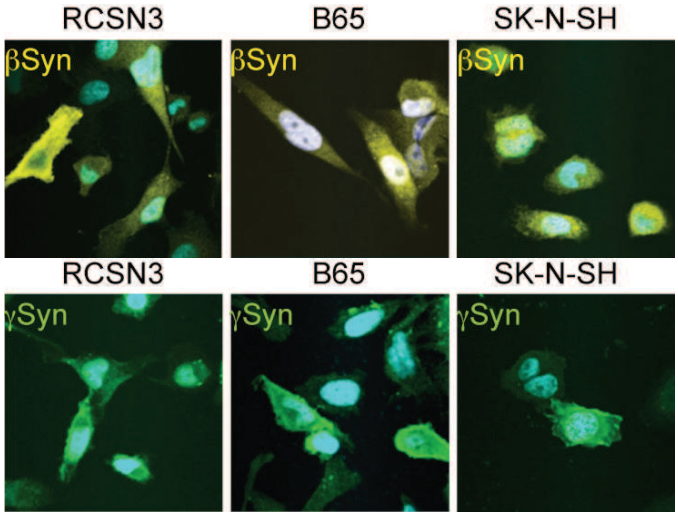

Figure 41: Intracellular localization of EP-delivered α–(red), β–(yellow) and γSyn (green)
Scale bar = 30 µm.

In vitro, members of the *Synuclein* family have been shown to bind to small unilamellar vesicles, which induces large conformational changes in the highly conserved N-terminal regions of these proteins[151, 252]. However, *in vivo* methods have failed to confirm these membrane-association induced conformational changes, although weak interactions between over-expressed αSyn and cellular lipid rafts have been reported[253]. Overexpression of αSyn has been suggested to alter the morphology of mitochondria via direct interactions with mitochondrial membranes[170, 254]. To explore potential membrane interactions of exogenously delivered αSyn, as well as to check for the intactness of cellular organelles after the EP procedure, electron microscopy experiments were performed on thin-sectioned cells that had been targeted with αSyn. Cryo-sections (60 nm) of fixed cells were immunolabeled with primary anti-FL αSyn antibodies and immunogold-labeled (12 nm) secondary antibodies. These EM images revealed no major morphological changes of organelles in EP treated cells. Cellular morphologies of mitochondria, the Golgi apparatus, the ER and the nuclear envelope appeared to be perfectly intact ***(Figure 42)***. Low levels of endogenous αSyn were detected in non-electroporated control cells. Both electroporated HeLa and RCSN3 cells displayed cytoplasmic, as well as a weak nuclear presence of αSyn. No extensive levels of membrane co-localization were detected and gold-particles distributed evenly throughout the cytoplasm ***(Figure 42 C, D)***.

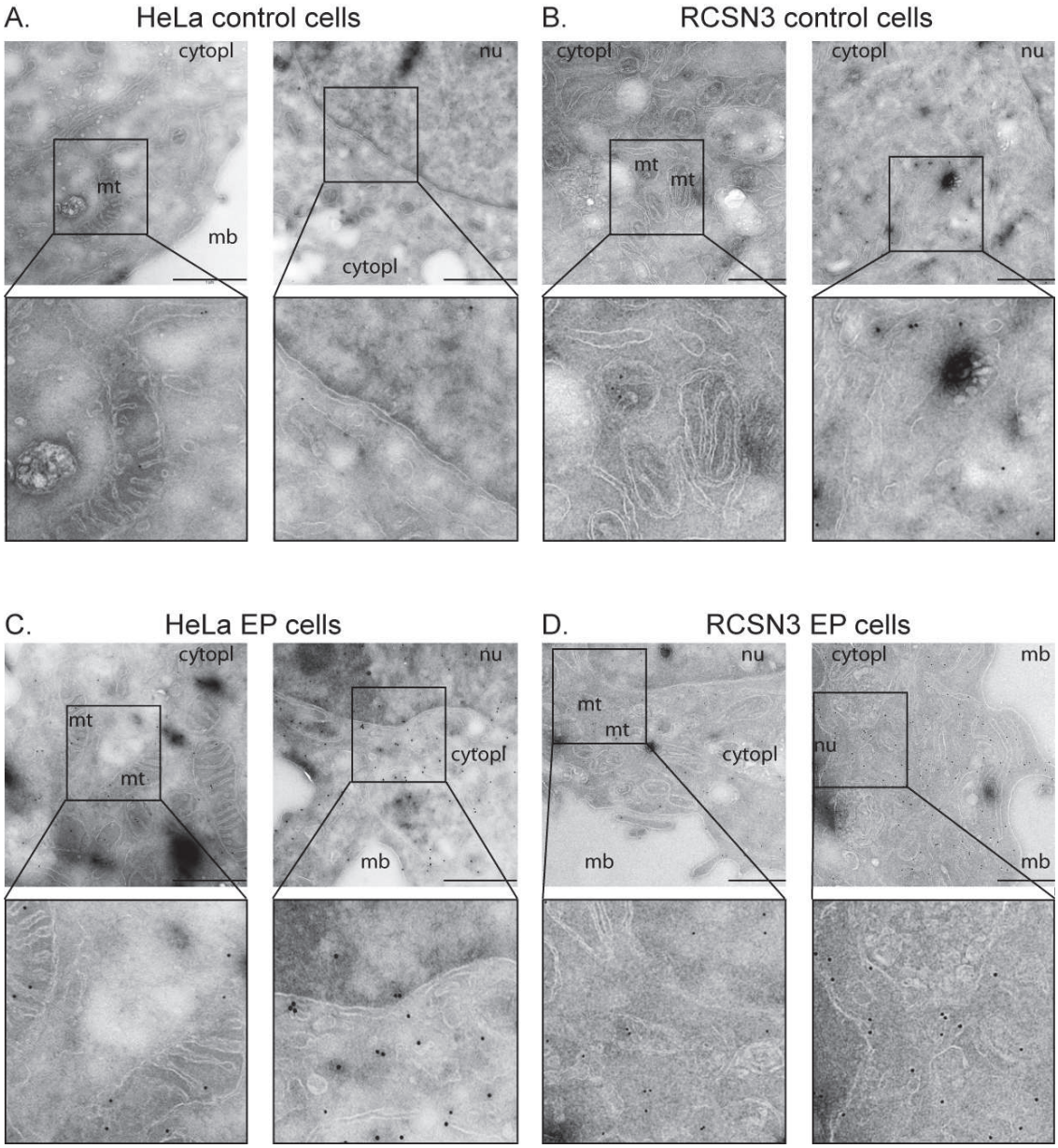

Figure 42: Immunoelectron microscopy (IEM) images of HeLa and RCSN3 cells post EP delivery of αSyn

(A, B) IEM of non-electroporated control cells. Low levels of αSyn were detected in RCSN3 cells (B). (C, D) IEM of αSyn electroporated cells. No major morphological changes of intracellular organelle structures were observed. Cytoplasmic and reduced nuclear localization of αSyn was confirmed. No specific membrane association was detected, Scale bar = 500 nm.

2.2.6 1D and 2D ^{1}H-^{15}N SOFAST-HMQC NMR experiments of αSyn in mammalian cells

Recombinantly expressed ^{15}N isotope-labeled αSyn was EP delivered into the previously outlined five cell types (400 µM). I collected the manipulated cells for pilot *in-cell* NMR experiments. Initial 1D ^{1}H-^{15}N SOFAST-HMQC spectra revealed

different NMR signal intensities of delivered αSyn (red trace) in the different cells. Similar 1D NMR spectra that were recorded on cell supernatants after the respective NMR experiments (see below) did not show any sign of protein leakage (blue trace) ***(Figure 43)***. Measured NMR intensities were translated into NMR-detected protein concentrations, which univocally demonstrated that most of the delivered *Synuclein* molecules contributed to the detected NMR signal intensities. Thus confirming that exogenously delivered αSyn tumbled freely in the cytoplasm of these cells.

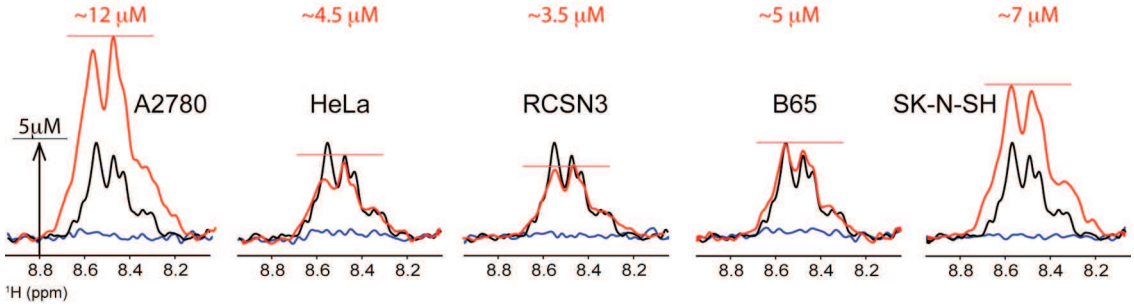

Figure 43: 1D ^{1}H-^{15}N SOFAST-HMQC *in-cell* NMR spectra of αSyn in different cell lines
In-cell NMR traces are shown in red, a 5 µM *in vitro* reference trace of pure αSyn is shown in black. The protein leakage control experiment revealed the NMR traces shown in blue. Effective NMR concentrations were calculated based in the measured *in-cell* NMR signal intensities with respect to the *in vitro* reference spectrum.

To gain atomic resolution insights into the structural properties of αSyn inside these cells, I also recorded residue-resolved 2D SOFAST-HMQC *in-cell* NMR spectra on these samples. 2D NMR spectra displayed good overall signal qualities and immediately revealed that αSyn remained mostly disordered and monomeric in all five cell types ***(Figure 44)***. Both different and congruent regions of site-selective line broadening were apparent, whereas the NMR characteristics of most αSyn signals indicated that the protein retained high degrees of internal mobility in all cells. As previously stated, αSyn has been reported to interact with lipid vesicles and cellular membranes and that this interaction occurred via the formation of an amphipathic alpha-helix within the first 100 residues of the protein[18]. This conformational change is readily detectable by high-resolution NMR spectroscopy[255]. Surprisingly, no indications for interactions with intracellular membranes were detected in any of these, and other, NMR spectra. Moreover, the fact that most of the delivered αSyn contributed to the detectable NMR signals strongly emphasized the notion that most of the protein molecules were tumbling freely in these cells. As intracellular αSyn

aggregation would lead to the formation of high molecular weight species, which do not give rise to detectable NMR signals[256], extensive levels of αSyn aggregation could be ruled out, based on the excellent overall quality of the detected NMR signals. Neither IF staining ***(Figure 41)*** nor native PAGE analysis ***(Figure 52)*** yielded any evidence for intracellular protein oligomerization. This further substantiated the notion that intracellular αSyn remained intrinsically disordered and monomeric.

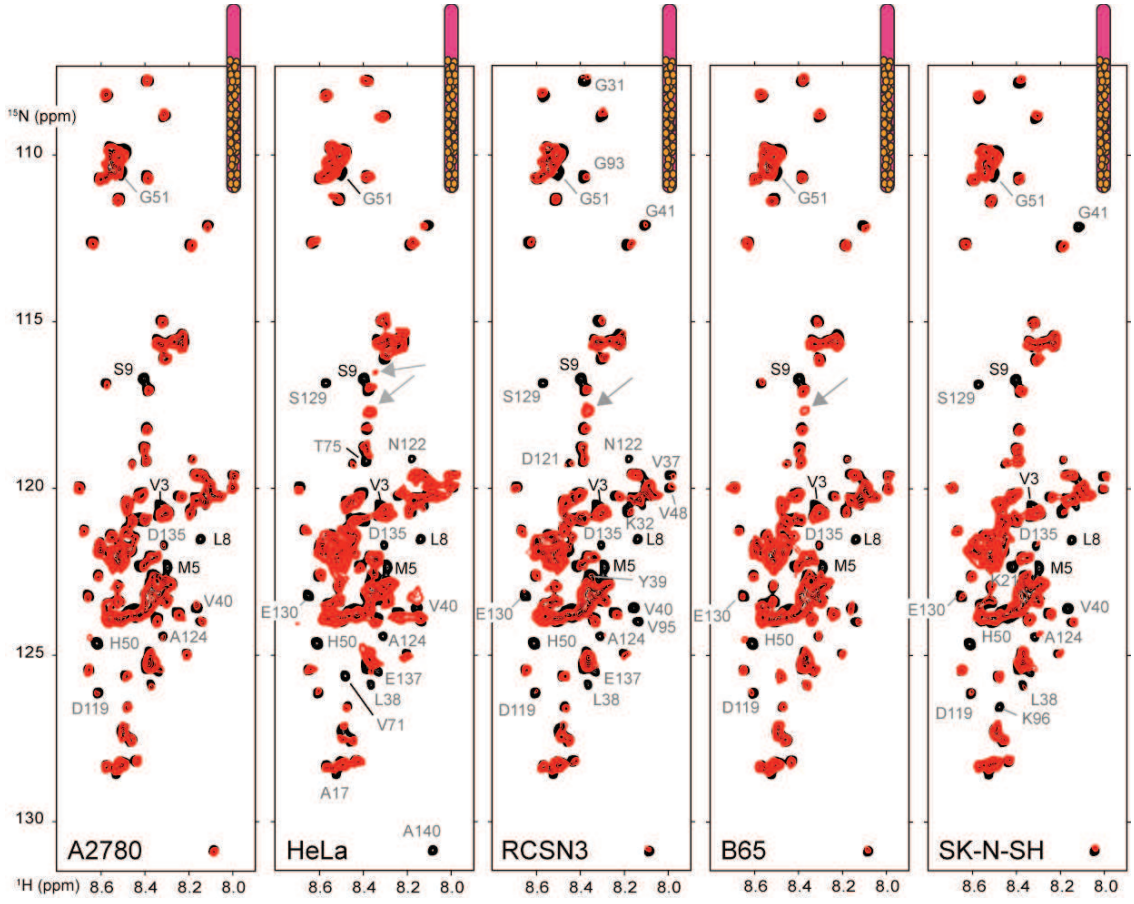

Figure 44: 2D ^{1}H-^{15}N SOFAST-HMQC *in-cell* NMR spectra of αSyn in different cell lines
Red: *In-cell* NMR spectra, black: 5 µM *in vitro* reference NMR spectra. Gray arrows indicate cell-type specific metabolite signals.

2.2.7 Site-selective line broadening of αSyn in mammalian cells

Despite the fact that αSyn remained soluble, monomeric and disordered inside these cells, regions of site-selective line broadening indicated that some portions of the protein experienced vastly different chemical- and/or conformational-exchange properties inside these cells. Significant broadening effects of N-terminal αSyn were

observed, which primarily affected the first 10 residues of the protein. Broadening of NMR signals was also detected for residues around His50, especially in HeLa, RCSN3 and SK-N-SH cells **(*Figure 45, A*)**. No obvious line broadening effects were noted for residues within the hydrophobic and aggregation prone NAC region, with the exception of a stretch of continuously broadened αSyn NMR signals (aa 93-95) in RCSN3 cells **(*Figure 45, B*)**. αSyn residues Asp119, Ala124, Gln122, Ser129, Glu130 and Glu137 in the C-terminus of the protein experienced considerable degrees of line broadening in some of the cell lines **(*Figure 45, C*)**.

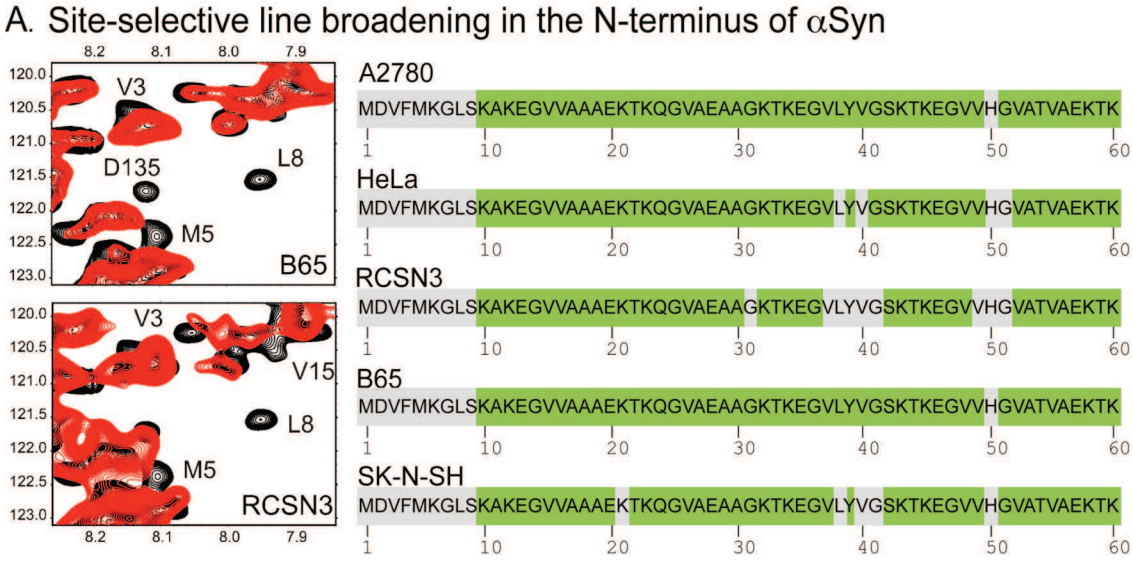

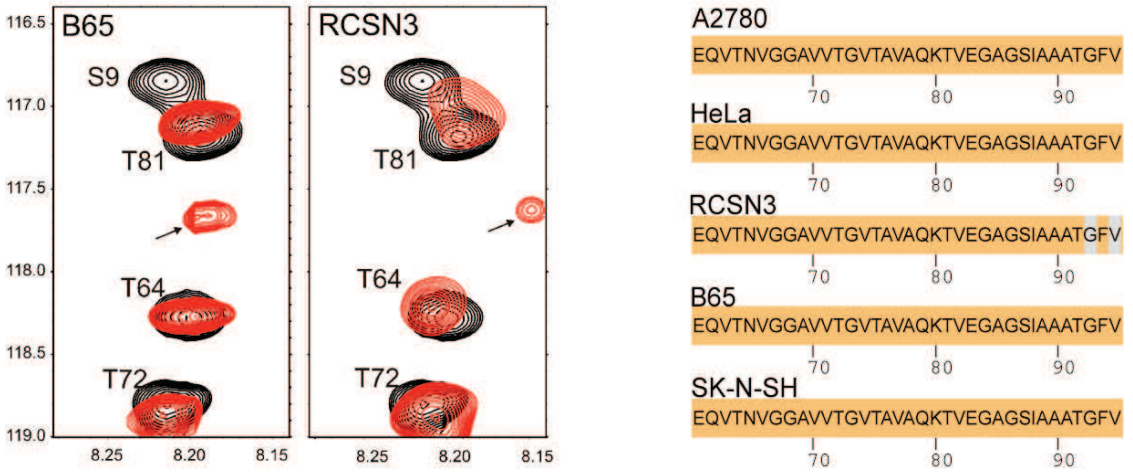

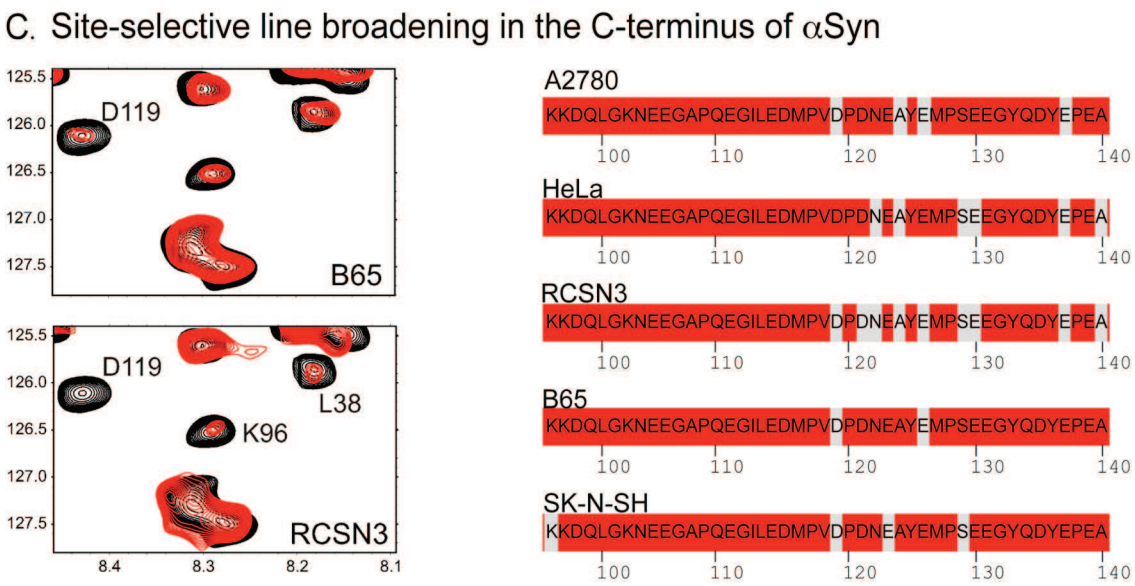

Figure 45: Regions of αSyn site-selective line broadening the different cell lines
Right panel: Selected regions of 2D SOFAST-HMQC *in-cell* NMR spectra (red). Left panel: Broadened residues are indicated in grays. A); B); C) show the N-terminal, NAC region and C-terminal region of αSyn, respectively.

2.2.8 Site-selective line broadening of βSyn and γSyn in B65 cells

β- and γSyn share a high N-terminal degree of sequence homology with αSyn but diverge at their C-termini[164]. Both βSyn and γSyn interact with lipid membranes[177], but exhibit different aggregation characteristics. βSyn is non-amyloidogenic, whereas γSyn aggregates much slower than αSyn[257]. Transient intramolecular long-range contacts as they are found in αSyn, are absent in βSyn and γSyn[186, 257]. For these reasons, βSyn and γSyn are useful models to further understand the structural properties of αSyn inside cells. To investigate whether line-broadening of N-terminal NMR resonances indicated intracellular alterations of this long-range contact network, similar *in-cell* NMR samples were also prepared with β-, and γSyn. In analogy to αSyn, β-, and γSyn remained intrinsically disordered and monomeric inside these cells, without any evidence for membrane binding ***(Figure 46)***.

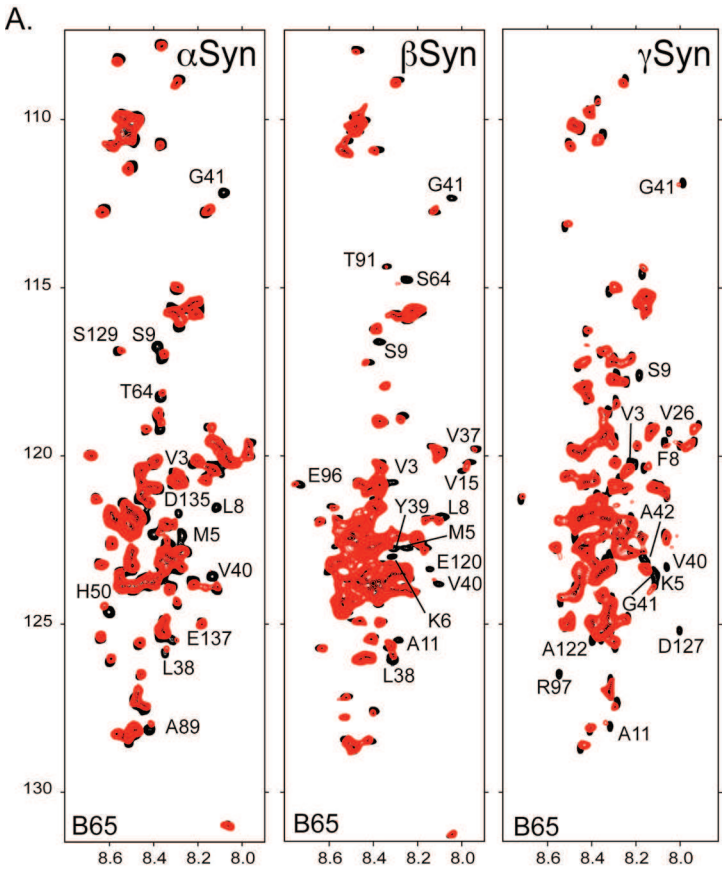

Figure 46: 2D ^{1}H-^{15}N SOFAST-HMQC *in-cell* NMR spectra of β-, and γSyn in B65 cells
Red: *In-cell* NMR spectra, black: 5 µM *in vitro* β-, and γSyn reference spectra. β-, and γSyn were present as intrinsically disordered monomers inside B65 cells.

In both β-, and γSyn, residues 1-9 were similarly broadened beyond detection. Further line broadening was observed in a region around residues 35-45, reminiscent of the same effect in αSyn ***(Figure 47, A)***. C-terminal residues of β-, and γSyn were also affected in an analogous manner ***(Figure 47, B)***.

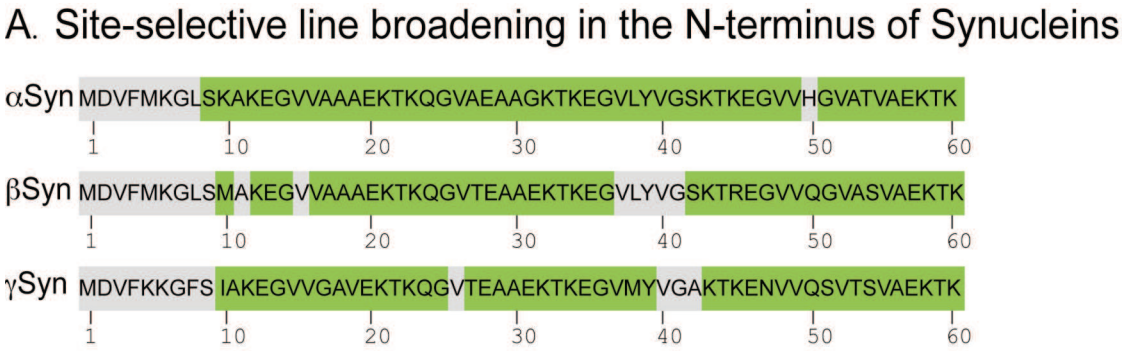

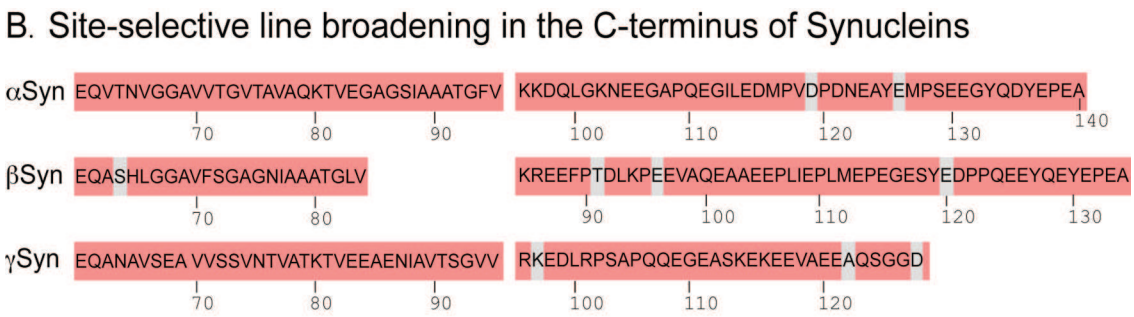

Figure 47: Site-selective line broadening of β-, and γSyn in B65 cells.
Broadened residues are indicated with a grey background. A); B) show the N-terminal and C-terminal *Synuclein* regions respectively. Significant line broadening of N-terminal resonance cross-peaks was detected.

Similar N-terminal line broadening profiles of αSyn, βSyn and γSyn suggested that all *Synuclein* isoforms experienced similar changes in chemical, and/or conformational exchange behaviors inside cells. Absence of long-range contacts in βSyn and γSyn indicated that these perturbations may arise due to local interactions/alterations that affected the N-termini of these proteins (see chapter 2.2.11 for details).

2.2.9 Dynamic properties of αSyn inside mammalian cells

To learn how these different intracellular environments influenced the dynamic properties of αSyn, longitudinal (T1) and transverse (T2) relaxation rates[258, 259] were measured by *in-cell* NMR spectroscopy. Overall, changes in fast, or intermediate internal protein motions were assessed via T1-, T2-relaxation measurements that I performed by integrating 1D-trace envelopes of ^{1}H-^{15}N SOFAST-HMQC *in-cell* NMR spectra. By comparing these *in-cell* NMR rates to *in vitro* obtained relaxation properties, I established that fast protein motions were least affected by the intracellular environment **(*Figure 48, A*)**, which argued against extensive modulations of ps time-scale protein motions inside cells. In contrast, protein motions on the ns to ms time-range were severely affected by the intracellular environment **(*Figure 48, B*)**.

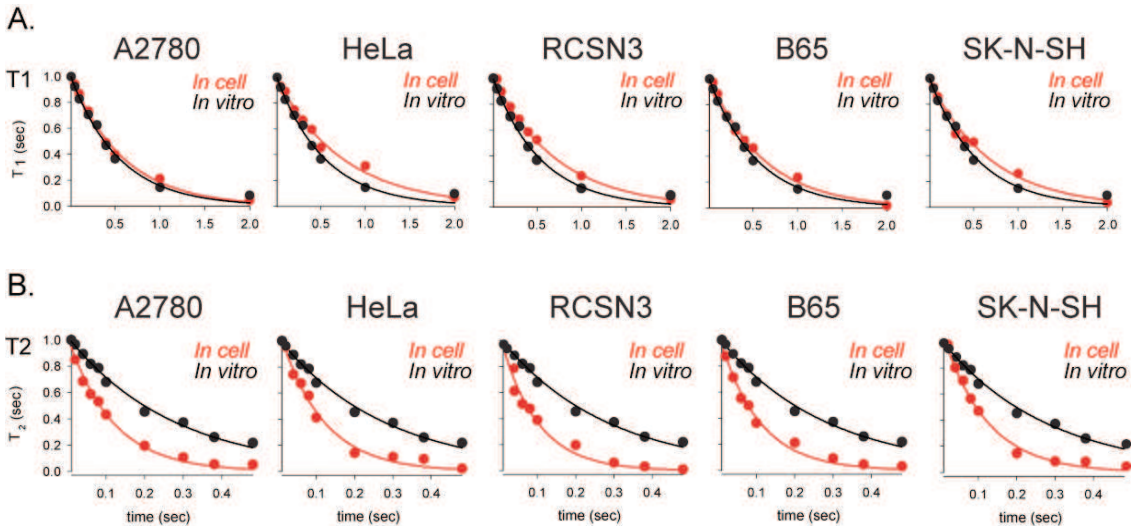

Figure 48: 1D ^{1}H-^{15}N SOFAST-HMQC relaxation rates (T1, T2) of αSyn inside different cell lines
In-cell (red) and in *in vitro* (black) measurements are compared. No significant changes in T1's (A) were observed, however much faster T2's were measured for αSyn inside cells (B). Peak intensities were taken at maximum peak height in each spectrum. Errors were evaluated using the individual signal/noise ratios. ^{15}N relaxation rates R_1 and R_2 were obtained by fitting the time dependent intensities of each peak *i* with a simple exponential equation, $I^i(t) = I^i_0 \exp(-R^i t)$ where *t* is the ^{15}N relaxation delay.

Because intermediate protein motions (i.e. T2 relaxation properties) were mainly affected inside cells, I recorded 2D residue-resolved T2 NMR experiments on αSyn in A2780 and B65 cells. Because of considerable spectral overlap of several *in-cell* NMR resonance signals (indicated by grey bars in figure 49) and because of the aforementioned line broadening characteristics of other αSyn signals (indicated by red triangles), T2 relaxation properties of only 42 (in A2780) and 21 (in B65) αSyn residues could be determined with high accuracy ***(Figure 49)***. The higher intracellular concentration of αSyn in A2780 cells permitted a more representative analysis of residue-specific relaxation properties. The fastest T2 relaxation times could be measured for the stretch of residues 30 to 45 (100 to 250 ms) and for residue 118 to 130 (100-150 ms). For residues 50 to 60, intermediate T2 values were obtained (200 ms). Astonishingly, for residues 60 to 110, encompassing the entire NAC region and a short stretch of the C-terminus of αSyn, the measured T2 relaxation times were similar to the ones obtained *in vitro*. Altogether, the determined *in-cell* dynamics of αSyn pointed to a restriction in motions of certain regions of the protein, which possibly arise due to non-specific contacts with cytosolic components and/or conformational-chemical exchange effects on the ns timescale.

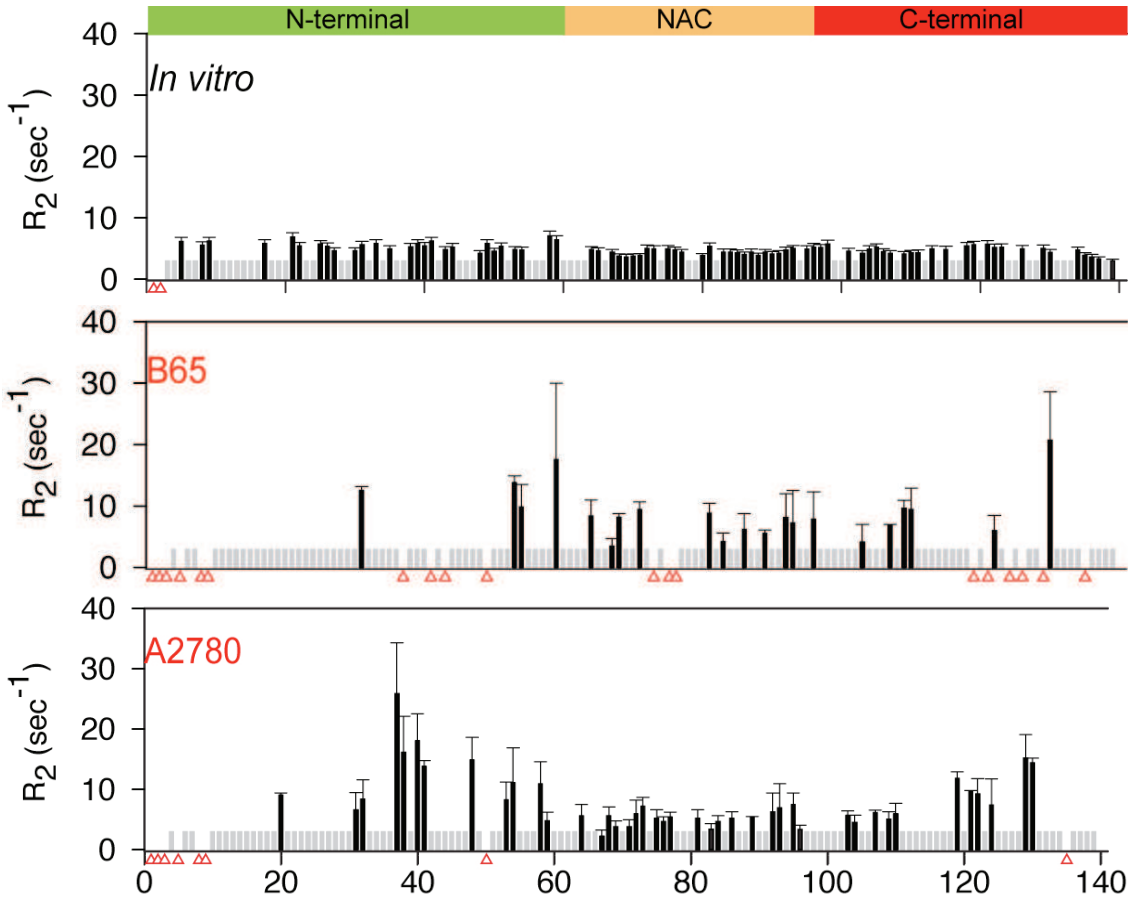

Figure 49: αSyn residue-specific R2 relaxation rates, measured by 2D ^{1}H-^{15}N SOFAST-HMQC *in-cell* and *in vitro* NMR experiments.
A) Relaxation rates of 42, or 21 αSyn residues (out of 140) were accurately determined in A2780 and B65 cells, respectively. Overlapping resonance signals that were not included in the analysis are shown as grey bars, NMR signals that were broadened beyond detection are indicated with red triangles. Fast relaxing αSyn residues localize to the N- (aa30-45) and C-terminus (aa118-130) of the protein. αSyn residues located within the NAC region (aa60-110) displayed dynamic properties that were similar to *in vitro* reference values. These relaxation rates were measured 2 or 3 times, the standard errors between these independent experiments are shown.

2.2.10 2D ^{1}H-^{15}N SOFAST-HMQC experiments of αSyn *in-cell* lysates

To lyse *in-cell* NMR specimens is known to improve the quality of the resulting NMR spectra, as has been demonstrated for bacterial[6,257], yeast[10] and *Xenopus* oocytes[43] samples. These improvements are generally caused by sample dilution and faster overall tumbling rates in these less viscous and less crowded environments. I prepared cell lysates from my *in-cell* NMR samples and similarly recorded 2D-HMQC spectra ***(Figure 50)***. Significant narrowing of the resonance line-widths indicated enhanced overall dynamics of αSyn in these lysates. Besides improvements in general spectral qualities, I further observed that N-terminal αSyn Val3, Met5, Leu8, Ser9, as well as C-terminal residues Asp119, Ala124, Glu135 and Glu137 were no longer

broadened beyond detection (labeled in green in figure 50). However, these N-terminal residues displayed substantial chemical shift changes. In addition, NMR spectra reported the presence of two new resonance signals (indicated with green arrows).

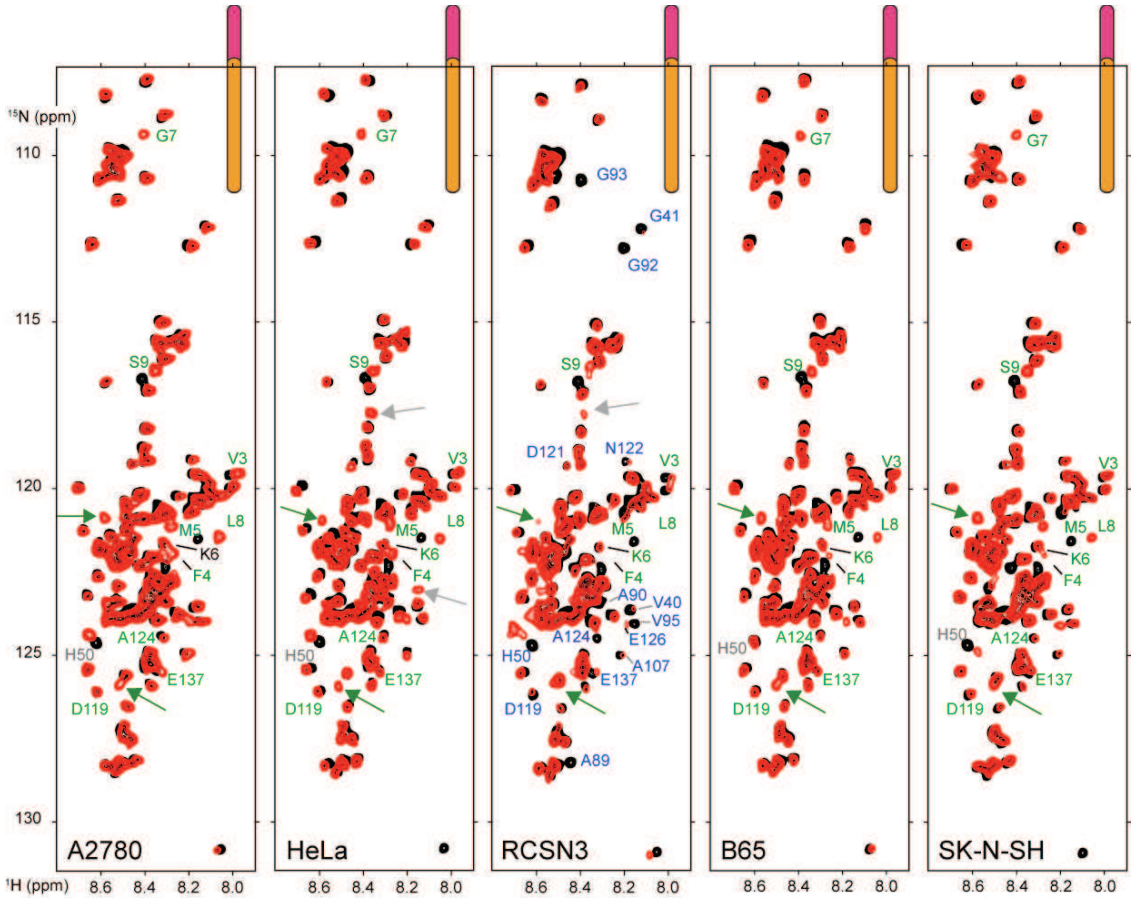

Figure 50: 2D ^{1}H-^{15}N SOFAST-HMQC NMR of αSyn *in-cell* lysates
Red: Lysate NMR spectra, black: 5µM αSyn *in vitro* reference NMR spectra. Narrowing of resonance signals indicated enhanced dynamics of αSyn. Reappearance of N- and C-terminal αSyn signals and their respective identities are indicated in green. Two newly identified cross peaks are indicated with green arrows. Only in case of RCSN3 cells, the majority of the broadened *in-cell* NMR resonance signals remained poorly detectable in the respective cell lysate (indicated in blue).

In RCSN3 cell lysates, not all of the broadened N- and C-terminal *in-cell* NMR signals were recovered (indicated in blue). In addition, line broadening was detected for some residues of the NAC region, which constituted a behavior that was not noted in any other cell type ***(Figure 51)***.

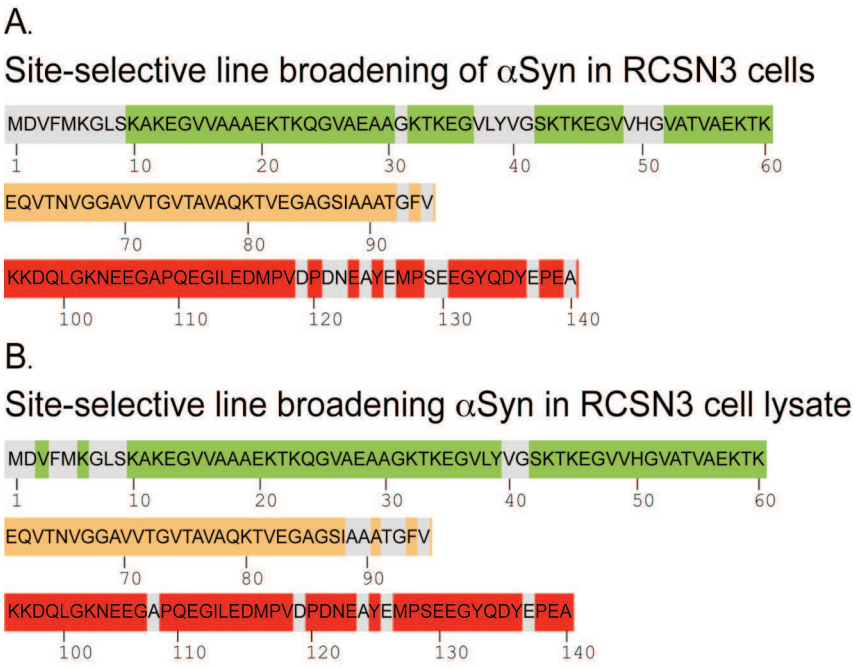

Figure 51: Site-selective line broadening of αSyn resonances in RCSN3 cells before and after lysis
A) Line broadened *in-cell* NMR residues of αSyn are indicated with grey boxes. B) Comparative outline of broadened residues in RCSN3 cell lysates.

Possible intracellular oligomerization events of αSyn could account for this behavior. I therefore analyzed RCSN3 lysates by native PAGE and Western blotting ***(Figure 52)***. Monomeric αSyn and different forms of αSyn oligomers were loaded as controls. Immunoblotting was performed with anti-Syn antibodies that had been raised against the full-length protein. No high molecular species were detected in the RCSN3 cell lysates.

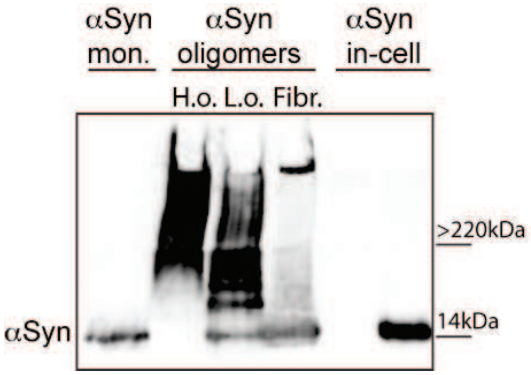

Figure 52: Native PAGE Western blot analysis on lysates of RCSN3 αSyn *in-cell* NMR samples
αSyn monomer (~14 kDa) and different forms of αSyn oligomers (H.o: High MW oligomers, L.o.: Low MW oligomers, Fibr: αSyn fibrils) were additionally analyzed.

2.2.11 Post-translational modifications of αSyn

Although many post-translational modifications (PTMs) of αSyn had been reported to occur *in vivo*, Ser and Tyr phosphorylation, nitration, ubiquitination, Met oxidation, and N-terminal acetylation are amongst the most abundant[19]. Because PTMs covalently modify certain protein residues, characteristic changes in their NMR chemical shifts are known to occur[35]. On this basis, I describe PTM studies that I carried out on *in-cell* NMR samples of electroporated αSyn.

2.2.11.1 N-terminal acetylation of αSyn

As mentioned previously, lysates of *in-cell* NMR samples displayed better spectral qualities than the *in-cell* NMR samples themselves. Two new resonance signals and substantial chemical shift changes of N-terminal αSyn residues were detected. According to earlier reports[229, 230], N-terminal acetylation of αSyn resulted in the appearance of AcMet1, and Asp2 resonances and caused chemical shift changes in the sequence 1-MDVFMKGLSKAK-12, respectively. These reports and further comparisons of *in vitro* NMR spectra of acetylated αSyn ***(Figure 53, A)*** closely matched the detected peak patterns in the *in-cell* NMR spectra ***(Figure 53, B)***, thus suggesting that N-terminal acetylation of αSyn by endogenous cellular enzymes was causing the observed effects. Similar chemical shift changes were detected when bacterially expressed unmodified αSyn was added to freshly prepared cell lysates. In addition, lysate NMR spectra of βSyn and γSyn displayed identical resonance peak displacements, which strongly suggested that these isoforms were also N-terminally acetylated by endogenous enzymes. These results established that N-terminal acetylation of the *Synuclein* family of proteins occurred inside mammalian cells.

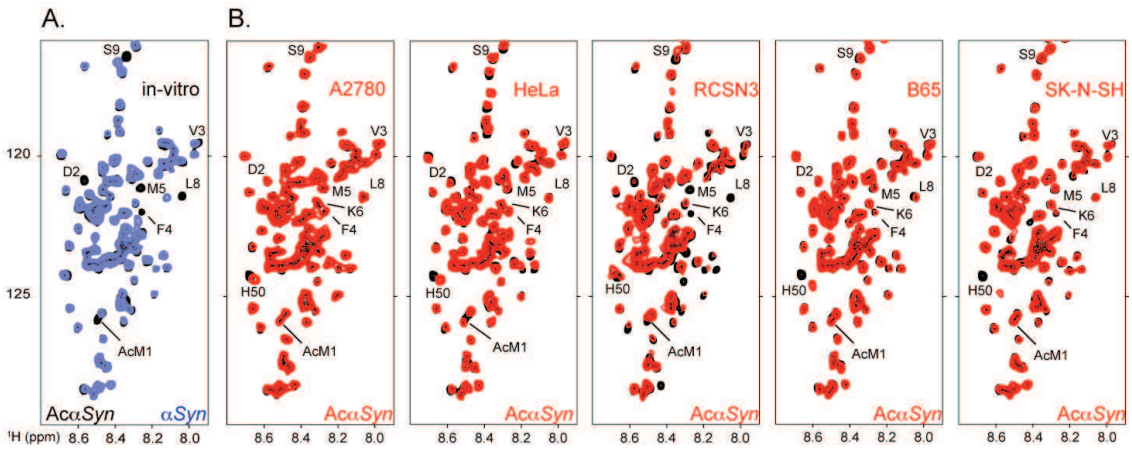

Figure 53: N-terminal acetylation of αSyn in different mammalian cell lysates
A) Comparison of 2D NMR spectra of *in vitro* acetylated αSyn (AcαSyn, blue) and of unmodified αSyn (black). Acetylation led to the appearance of Ac-Met1 and Asp2 resonance signals and substantial chemical shift changes of the following VFMKGLS residues (labeled in the respective NMR spectra). B) Similar N-terminal acetylation-induced chemical shift changes were also observed in all lysate NMR spectra of the protein

The chemical shift changes of His50 that I detected in the lysates of the different cell lines were attributed to slight changes in solution pH. This feature is a known NMR property of αSyn[260].

2.2.11.2 Ser129 phosphorylation of αSyn

Ser129 of αSyn constitutes the main phosphorylation site of this protein[19, 261]. In turn, phosphorylation of Ser129 has been strongly implicated in PD. 90% of the insoluble αSyn aggregates in Lewy bodies have been found to be phosphorylated at this site, whereas only a very small portion of monomeric, soluble αSyn (4%) is modified in this way in the brains of healthy individuals[220]. In SK-N-SY cells, very low levels of constitutive Ser129-phosphorylated αSyn have been found[262]. However, these levels increased upon addition of the generic phosphatase inhibitor okadaic acid. In my *in-cell* NMR experiments, no actions were taken to inhibit cellular phosphatase activities and Ser129 phosphorylated species were expected to most likely occur in SK-N-SH cells, because of the close relation of these two cell lines[231]. Protein phosphorylation can easily be detected by NMR spectroscopy[35, 37] provided that the levels of phosphorylated species are sufficiently high (i.e. >10% of the total isotope-labeled protein). Despite the fact that resonance signals of αSyn Ser129 were considerably broadened in most *in-cell* NMR spectra, Ser129 phospho-resonances,

which we knew from *in vitro* reference NMR spectra would resonate at 9.08 and 118.3 p.p.m. ($^{1}H/^{15}N$, respectively)[25] were not detected ***(Figure 44).***

One explanation for why I was unable to detected phosphor-Ser129 signals could be afforded by fast relaxation properties of this residue in its phosphorylated form. It could also be due to the presence of only a very small, fraction of phosphorylated αSyn. However, upon cells lysis, the Ser129 cross peak was easily detected at its 'unmodified' resonance frequency, which strongly argued against Ser129 posphorylation in these cells ***(Figure 50)***. To unambiguously determine the phosphorylation state(s) of cellular αSyn, I resorted to Western blotting using phospho-Ser129 specific antibodies ***(Figure 54)***. Detectable levels of Ser129 phosphorylation were only found in HeLa and SK-N-SH cells.

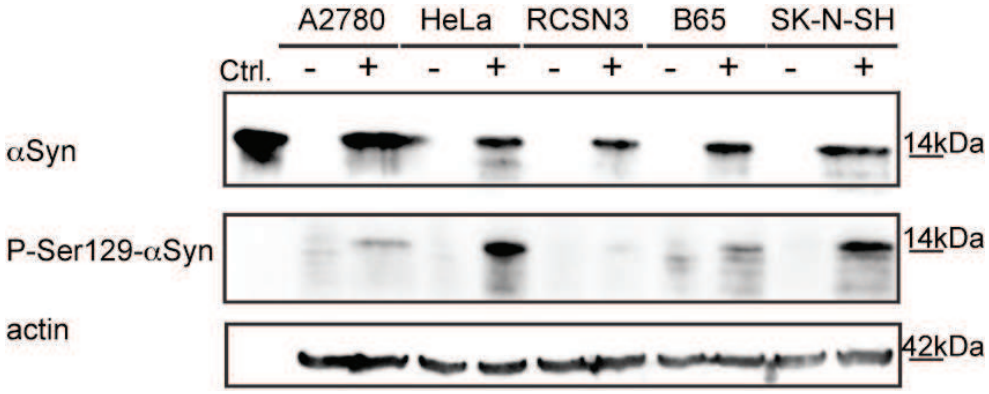

Figure 54: Western blot analysis of αSyn Ser129 phosphorylation in *in-cell* NMR samples

To investigate whether higher levels of cellular αSyn phosphorlyation could be detected by NMR spectroscopy, I transiently transfected HeLa cells with myc-tagged PLK3. PLK3 is a Ser/Thr protein kinase that has been reported to phosphorylate αSyn at Ser129[25]. I confirmed over-expression of PLK3 16 hours post transfection by Western blotting ***(Figure 55, A)***. I prepared lysates of transfected cells and added 5 µM of ^{15}N isotope-labeled αSyn for time-resolved *in situ* NMR measurements ***(Figure 55, B and C)***. These experiments clearly revealed phosphorylation of Ser129. NMR signal integration of the individual data points, for the detection of time-dependent changes in Ser129 phosphorylation states, revealed maximum phosphorylation levels at 200 min of lysate incubation (25%). At later time points, progressive reductions in phospho-Ser129 levels were noted (down to 10%). In summary, these results demonstrated that a

small portion of delivered αSyn was indeed phosphorylated in HeLa and SK-N-SH cells. This level of phosphorylation was only detected by Western blotting and not by NMR spectroscopy. Under conditions of transient PLK3 overexpression, NMR detectable phosphorylation levels indicated higher overall modification efficiencies. Even under these conditions, αSyn Ser129 modification was strongly regulated by cellular phosphastase activities.

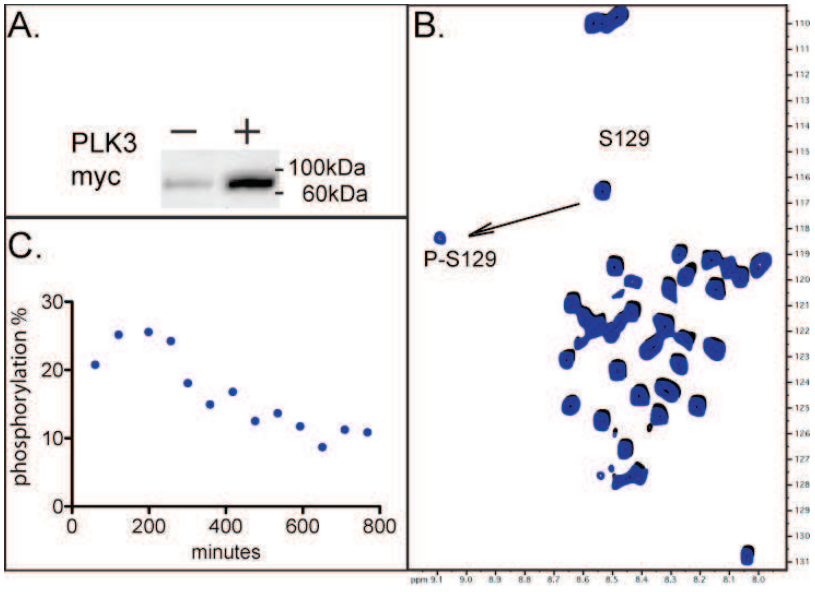

Figure 55: *In vitro* phosphorylation of αSyn in PLK3 transfected HeLa lysates
Western blot analysis on non-transfected and myc-PLK3 transfected HeLa cells. B) 2D SOFAST-HMQC NMR spectrum of the highest protein phosphorylation level that was achieved after 200 min of lysate incubation. C) Time-resolved phosphorylation profile of αSyn in lysates of myc-PLK3 transfected HeLa cells.

2.2.11.3 Other post-translational protein modifications of αSyn

My NMR data also suggested that αSyn was not subjected to other PTMs that had been reported to occur *in vivo*[263, 264,265]. PTMs such as ubiquitination and sumoylation, two PTMs that would result in apparent increases in the molecular weight of αSyn, were not detected in any of the Western blot experiments ***(Figure 59)***.

2.2.12 *In-cell* NMR quality control experiments

2.2.12.1 Identification of background NMR signals

Several *in-cell* NMR spectra displayed strong resonance signals at peak positions that had not been previously identified as characteristic for αSyn. To investigate whether these new resonances corresponded to NMR signals that did indeed originated from the delivered protein, I tested electroporated cells in the absence of protein applied in the electroporation buffer, and the different cell culture media, for the presence of background metabolite NMR resonances. Indeed, four major background signals were detected by 2D ^{1}H-^{15}N SOFAST-HMQC NMR experiments in B65, HeLa and RCSN3 cells ***(Figure 56)***. The resonance peak at 7.6 and 131.19 p.p.m. (^{1}H/^{15}N, respectively) originated from metabolites in the cell medium, whereas the remaining NMR signals originated from unidentified cellular compounds. Several minor populations of NMR-active species were additionally detected in RCSN3 cells.

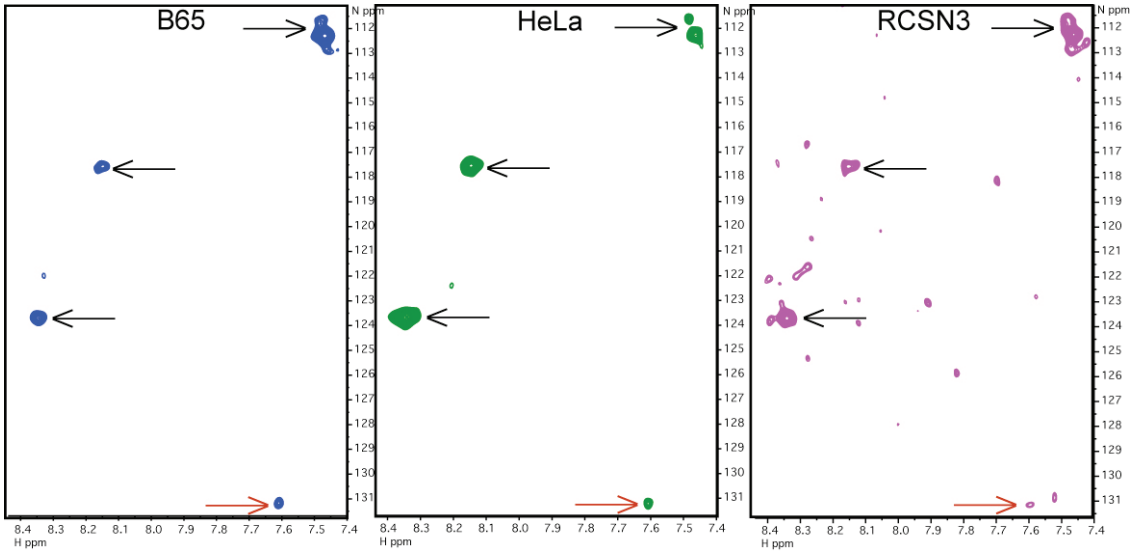

Figure 56: **Background NMR signals in B65, HeLa and RCSN3 cells**
2D ^{1}H-^{15}N SOFAST-HMQC spectra of non-electroporated control cells. Arrows indicate background NMR signals.

2.2.12.2 Cell viability and protein leakage controls

In many instances, *in-cell* NMR experiments were performed over extended periods of time and it was therefore important to develop a simple routine to quickly assess overall cell viability and protein leakage ***(Figure 57)***. After each NMR measurement, cells were taken out of the NMR tube and carefully sedimented. 5 µL of

the cell slurry was subjected to a cell viability test using the Trypan Blue staining protocol. I determined that different cell lines displayed different viability indices. Surprisingly, the highest level of cell death was detected for electroporated HeLa cells, which amounted to ~25% after NMR measurements that exceeded 9 hours. In the course of the Trypan Blue staining protocol, I also recorded 1D NMR spectra on the remaining cell supernatants, to check for the presence of delivered proteins that might have leaked out of the cells. Despite the occurrence of cell death in a fraction of the analyzed cells, no extracellular NMR signals of ^{15}N isotope-labeled αSyn were detected in any of the supernatant samples. This strongly suggested that protein leakage did not contribute to the NMR spectra that I had recorded on these *in-cell* NMR samples. Finally the recovered supernatant was added back to the cell slurry and reanalyzed by NMR spectroscopy to confirm intracellular protein localization. A flow diagram of this standard control procedure is outlined below.

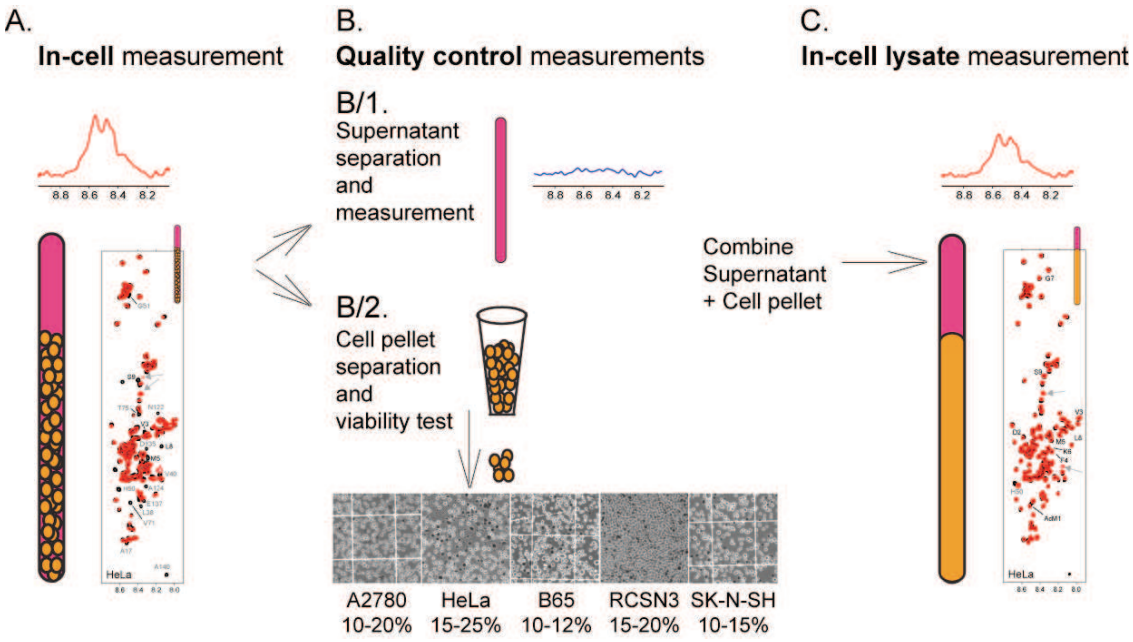

Figure 57: Flow-diagram of control experiments to assess cell viability and protein leakage
A) 1D-SOFAST and 2D-SOFAST *in-cell* NMR measurements on intact cells. B) Cells are sediment and analyzed by Trypan Blues staining. Supernatants are tested for leaked proteins by NMR spectroscopy separated. C) Supernatant is added back to intact cells of cell lysates for final rounds of NMR control experiments.

2.2.12.3 αSyn degradation

Having established that protein leakage did not contribute to the detected *in-cell* NMR signals, I set out to probe the intactness of αSyn in the *in-cell* NMR samples,

despite the fact that 2D *in-cell* NMR spectra did not provide any indication that this was in fact the case. To this end, I analyzed *in-cell* NMR samples at different time points by Western blotting using a range of commercially available anti-αSyn antibodies. Pilot tests on electroporated cells that I recovered immediately after the EP procedure confirmed previous results that showed intact monomeric αSyn ***(Figure 39, A).*** The same was true for samples that were obtained after 5 hours of recovery ***(Figure 58, A)***. Other sets of cell samples were collected every three hours after the EP procedure and after cells had been put in the NMR sample tube and incubated at 10° C, thus mimicking the exact conditions of the NMR experiments. After 0, 3, 9 and 20 hours, aliquots were removed and directly boiled in SDS sample buffer. The resulting lysates were analyzed by Western blotting. Results showed that intracellular αSyn remained intact over 20 hours under these conditions. Small amounts extracellular αSyn were detected in the supernatants of these cells after 9 hours ***(Figure 58, B)***. When cell lysate were prepared from these mock *in-cell* NMR samples, intact αSyn was similarly detected ***(Figure 58, C)***.

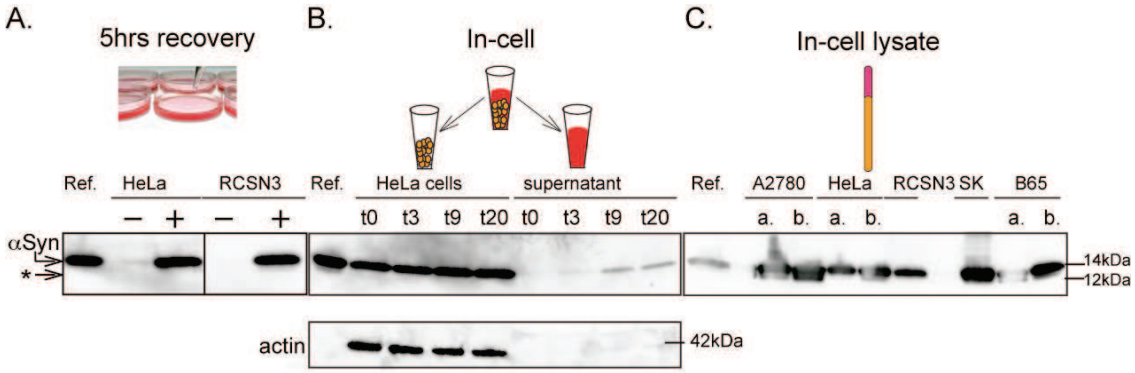

Figure 58: αSyn degradation and cell leakage control experiments
A) αSyn detection after 5 hours of recovery in electroporated HeLa and RCSN3 cells. B) *In-cell* and supernatant detection of αSyn in HeLa *in-cell* NMR samples. Small amounts of extracellular αSyn are detected after 9 hours. C) Western blot analysis of cell lysates from 5 different cell lines.

3. Discussion

The primary aims of this thesis were twofold: First, to develop a suitable method for delivering isotope-labeled proteins into mammalian cells for the purpose of generating high-quality *in-cell* NMR samples and, second, to apply this method to structurally and functionally characterize the human intrinsically disordered protein αSyn in different mammalian cells. To achieve the first goal, I comparatively analyzed three different protein transduction methods with respect to their capacities to deliver recombinantly produced proteins into mammalian cells. Cell penetrating peptide (CPP)- fusion techniques, the bacterial toxin Streptolysin O (SLO)-mediated delivery protocol, and protein transduction by electroporation (EP) were studied.

I determined that all three methods produced comparable levels of overall cell viability after the respective treatments (>80%), after initial optimization procedures. For the CPP-mediated protein delivery approach, separation of non-reacted CPP moieties proved to be essential for reducing cytotoxity, which was in agreement with previous reports[237], whereas SLO concentrations had to be carefully optimized in order to enhance cell survival after pore formation and protein delivery[12, 241, 266]. I further established that substantial differences in toxin tolerance levels existed between different cell lines, which was consistent with previous reports[266, 267]. For the electroporation routine defined phosphate/HEPES buffers turned out to provide optimal osmolarity[268] and conductivity[269] conditions. Based on knowledge from EP-mediated DNA transduction protocols, I identified suitable electroporation pulse programs for the panel of tested mammalian cells. Furthermore, I achieved significant improvements in survival rates of EP-manipulated cells, when I added ATP and reduced glutathione (GSH) to the electroporation mixtures. While overall cell viability was comparably high with all three protocols, protein uptake efficiencies varied greatly. Low uptake efficiencies were determined for all CPP-mediated delivery approaches. Although successful CPP-dependent drug delivery routines had been reported[49, 270], several other studies indicated great variations in protein uptake levels using this method[271-274]. To improve general protein transduction properties, I tested a range of additional conditions, including pre-incubation with pyrenebutyrate (PA), which had been speculated to increase the overall hydrophobicity of positively charged CPP residues[275, 276], and to thereby induce direct translocation of CPP-cargo constructs into the cytoplams[12, 71, 277]. In contrast to these published results, my data indicated that no

improvements in the uptake efficiencies could be obtained by PA treatment. These observations are in line with recent findings that suggest that PA treatment leads to increased extracellular binding, rather than to better transduction efficiencies of CPP-cargo constructs[278]. For SLO-mediated protein delivery approaches[241, 279] and EP-mediated protein transduction procedures[110, 280], cellular uptake levels were generally higher. However, I observed substantial differences in intracellular sample deposition depending on the applied sample concentrations. In case of the SLO routine, intracellular protein concentrations reached a maximum level at 100 μM of exogenously added protein, which implied that the number of pores that were formed on the cell membranes constituted a bottleneck for protein uptake efficiencies. Since these pores represent open passages between the intracellular and extracellular compartments through which proteins move in a concentration gradient-dependent manner[95, 281], higher intracellular protein concentrations could not be obtained without substantially compromising overall cell viability. This was not the case in EP-mediated protein delivery approaches, which constituted a unique advantage of the EP method.
Differences in intracellular protein localization played another important quality control parameter that I comparatively analyzed in the course of this project. Because membrane binding, or organelle/vesicle entrapment of delivered proteins limit their detectability by solution-state NMRspectroscopy[10], uniform cytoplasmic distributions needed to be achieved. Therefore, I also carefully analyzed the intracellular localization properties of αSyn that I had delivered into mammalian cells with these three methods. Using live cell imaging and confocal microscopy I found that CPP-delivered αSyn displayed a highly punctuated pattern of intracellular distribution, which suggested that the protein primarily localized to vesicle-like structures in the cytoplasms of all cells. Similar cellular distribution patterns of CPP-tagged cargo proteins had also been observed in other studies[51, 70, 75] and interpreted as endosomal inclusions[282, 283]. A more dispersed cytoplasmic staining was evident for SLO-delivered αSyn, however I confirmed partial co-localization with lyosomal vesicles, by employing a range of lysosomal markers (data not shown). In contrast to both of these methods, EP-delivered αSyn displayed an exclusive cytoplasmic distribution in all of the manipulated cell types, which was clearly advantageous for the planned *in-cell* NMR experiments.

In summary, results obtained in the first part of my thesis enabled me to identify protein electroporation (EP) as the most suitable tool to delivery proteins into cultured

mammalian cells. Together, these results provided a very positive outlook for the second part of my thesis, for which I set out to characterize the structural and functional properties of intracellular αSyn in five different mammalian cell types.

I had chosen five different mammalian cell lines for *in-cell* NMR analyses of the human amyloid protein αSyn. These were separated in reference mammalian cells of non-neuronal origins, i.e. A2780 and HeLa cells, and in cells of neuronal origins with direct relevance for Parkinson's disease, i.e. SK-N-SH[231, 284], B65[232] and RCSN3[21] cells. RCSN3 cells are immortalized rat dopaminergic neurons from the *substantia nigra pars compacta* and thus constituted the closest disease-relevant cell type. I initially evaluated the endogenous levels of αSyn in these cells by using an improved immunodetection protocol[246]. I detected low endogenous levels of αSyn in all cell types, except in rat B65 and RCSN3 cells, where I found an alternatively spliced isoform of αSyn that mostly likely corresponded to a C-terminally extended, rat-specific form of the protein[247, 248]. Upon electroporation of exogenous αSyn, I found that intracellular protein levels were in the range of 20-120 μM, which closely matched the physiological concentrations of αSyn in synaptic termini (30-60 μM[249, 285]). These results established that my anticipated *in-cell* NMR studies were to be performed at close to physiological levels of intracellular αSyn. I assessed the intracellular distributions of EP-delivered αSyn by immunostaining confocal microscopy and found that most cells contained uniform pools of cytoplasmic protein. Using immunogold-labeling and transmission electron microscopy, I further established that intracellular αSyn did not associate with intracellular membranes, or the ER[253, 286, 287], although a small fraction of protein partially co-localized with mitochondria, as has also been reported earlier[288, 289].

I recorded several types of multi-dimensional high-resolution *in-cell* NMR spectra of αSyn in these mammalian cells. In line with previous *in-cell* NMR studies in bacterial cells[6, 42, 139, 290-292], results from these experiments clearly showed that αSyn remained monomeric and intrinsically disordered in all the tested cell types. These findings confirmed earlier biochemical reports that had argued for a monomeric protein state inside mammalian cells[6] and strongly challenged a current notion of an allegedly folded, alpha-helical and tetrameric conformation of αSyn, as the physiologically

relevant protein state[293-295]. In perfect agreement with prokaryotic *in-cell* NMR studies, I did not obtain any indication for membrane association or intracellular aggregation of αSyn inside mammalian cells.

Most structural studies on the membrane binding behavior of αSyn have been performed on membrane mimics that were largely composed of mixtures of 2-3 synthetic phospholipids[18]. The membrane-bound conformations that αSyn adopted in these studies varied in response to the lipid charge states, the lipid compositions, lipid chain structures and membrane vesicle curvatures[18, 296]. Even lipid to protein ratios affected αSyn's binding behavior[297]. Therefore, it remained unclear to what extent these *in vitro* studies recapitulated cellular membrane binding. At high lipid to protein ratios, for example, all Synuclein members interacted with lipid vesicles via the formation of an amphipathic alpha-helical structure that comprised the first ~100 residues of the proteins[177, 187], which had also been suggested by a number of *in vivo* studies[252, 298, 299]. However, in my *in-cell* NMR experiments no such interactions and no such conformational rearrangements within the N-terminal portions of αSyn were detected. In contrast, upon binding to lipid vesicles at low lipid to protein ratios, it had been shown that line broadening within the first 25 residues of αSyn occurred *in vitro*[297]. It is therefore conceivable that such kinds of interactions were present inside mammalian cells. The severely line-broadened N-terminal residues of αSyn and high T2 values for residues 30 to 45, indicating severely restricted dynamic motions, could possibly indicate such binding events. However, I observed different effects after cell lysis, where attenuated NMR signals of these residues were efficiently recovered. While this may be interpreted as intracellular membrane interactions of αSyn being extremely weak and readily modulated by changes in macromolecular crowding, the process of preparing the cell lysates may itself introduce some artifacts, in terms of altering the appearance of intracellular lipid vesicles, especially with regard to their curvatures, and thereby shift cellular binding equilibria from membrane-bound to unbound states. Another important aspect to consider is the post-translational protein modifications of αSyn that may affect its lipid binding behavior. N-terminal acetylation especially, has been shown to increase the helical propensities of the N-terminus of αSyn and thereby enhance its lipid binding affinity[229, 230]. Indeed, acetylated αSyn was detected in soluble brain homogenates of PD and DLB patients[220, 228] and under

physiological conditions in non-neuronal cells that over-expressed the yeast NatB N-acetyl transferase complex[24]. My *in-cell* NMR experiments revealed that αSyn was constitutively N-terminal acetylated in all mammalian cells and that β-, and γSyn were similarly modified. Therefore, line-broadening of N-terminal αSyn resonances could suggest a superposition of two scenarios: Conformational exchange effects due to increased helical propensities of N-terminal residues in acetylated αSyn and enhanced lipid 'scanning' properties that result in weak, transient membrane interactions. Membrane binding of αSyn is also affected by other PTMs such as protein phosphorylation, which is thought to diminish lipid interactions[261, 300]. αSyn contains several Ser and Tyr phosphorylation sites[19] and phosphorylation has been strongly implicated in the pathologies of synucleinopathies[301-303]. Modification of Ser129, for instance, has been shown to constitute the most abundant αSyn PTM in Lewy bodies and other cytoplasmic lesions in human[223] and primate[224] brains. In addition, low levels of αSyn Ser129 phosphorylation were identified in primary neuronal cells[223, 224]. In my experiments, I only observed low levels of phosphorylation of exogenously delivered αSyn in HeLa and SK-N-SH cells by Western blotting. No NMR signals of Ser/Tyr modified residues[25, 35] were detected in *in-cell* NMR spectra. This can possibly be explained by a strong regulation of kinase/phosphatase activities in these cells, which is in agreement with the detected low levels of αSyn phosphorylation (~25%) in lysates of PLK3 over-expressing cells. Whereas PLK3 efficiently phosphorylated αSyn *in vitro* and has been shown to modify αSyn in cultured cells and primary neurons [25, 304], tight regulation has also been suggested in a study by Okochi *et al.,* where significant levels of αSyn phosphorylation had only been observed after the addition of phosphatase inhibitors in αSyn over-expressing K293 and PC12 cells[222]. The physiological role of αSyn Ser129 phosphorylation in not completely understood, but it has been implicated neurotoxicity[305]. Lack of this modification might indicate that cells did not experience pathological conditions in the *in-cell* NMR experiments. Another αSyn modification, methionine[306] oxidation, should also be mentioned, as this modification has been shown to result in membrane dissociation. Oxidation of Met1 and Met5 of αSyn had been analyzed *in vitro* with respect to their inhibitory effects on interactions with membranes that contained small fractions of oxidized lipids[306]. *In*

vivo, oxidation of unsaturated fatty acids to lipid hydroperoxides (LOOH) may occur under physiological cellular conditions[307], or, more prominently, under conditions of increased levels of cellular oxidative stress[308]. Although I did not observe methionine oxidation of N-terminally acetylated αSyn inside cells, or cell extracts, low levels of oxidized αSyn may have formed and remained undetected.

Besides line broadening effects in the N-terminus of intracellular αSyn, several residues in the C-terminus of the protein also displayed fast intracellular relaxation properties and high T2 values, especially around a continuous stretch of amino acids at positions 119-130. This region of αSyn has been shown to interact with divalent metals[309] and to constitute the primary binding site for positively-charged compounds such as polycationic polyamines[310]. Because attenuated NMR signals in this region of αSyn were similarly recovered after cell lysis, these broadening effects may also be caused by weak, transient interactions with cellular components[311], among which positively charged biomolecules are excellent candidates.

In most instances, cell lysis alleviated the broadening effects that I observed in *in-cell* NMR experiments. However, in RCSN3 cells this was not the case and several αSyn resonance signals remained undetected even after lysis. Although native PAGE failed to indicate strong cellular association events of αSyn in these cells, or the formation of αSyn aggregates, the possible reasons for this behavior need to be investigated further. Especially also because RCSN3 cells represent the closest, disease-relevant model in my study, with several unique features of *substantia nigra* dopaminergic neurons[312, 313], including enzymes and other cellular factors (i.e. Tyrosine hydroxilase (TH)[314], the dopamine transporter DAT[315, 316], dopamine[317, 318] and neuromelanin[319, 320]) that have all been closely associated with PD pathogenesis[284].

Finally, the intracellular aggregation behavior of αSyn in mammalian cells, or lack thereof, must be discussed. Although greatly enhanced aggregation propensities of αSyn in crowded intracellular environments had been reported[204], and are thought to play pivotal roles the pathogeneses of PD[17] and other synucleinopathies[15], α–, β– and γSyn's retained their monomeric, intrinsically disordered conformations inside mammalian cells, without displaying obvious signs of intracellular aggregation. As beta-sheet rich oligomeric intermediates and fibrils[157, 197] form during the classical *on pathway* aggregation process, an overall decrease in detected NMR signals would have

been expected for any such cellular event. However, all of my *in-cell* NMR experiments, including the extensive Western blotting routines and NMR measurements of αSyn's intracellular protein dynamics, firmly established that the protein showed no signs of aggregation, or formation of high-molecular weight structures in any of the tested cells. In line with these results, the central hydrophobic NAC region of αSyn, critically required for initial intermolecular encounters in the course of aggregate formation[321, 322], displayed intracellular dynamic properties that most closely matched its *in vitro* behavior and, thus, was least affected by any of the mammalian cellular environments. It is important to emphasize that during all procedures to generate mammalian *in-cell* NMR samples, highly stringent selection criteria for viable and healthy cells were employed and I took great care to avoid contributions that might lead to cellular stress and promote αSyn aggregation[323, 19, 324]. Therefore, I consider the *in-cell* NMR results obtained in this study as representative for the physiological reference state of αSyn in healthy mammalian cells. Given, that a generic protocol for intracellular delivery of αSyn has now been established, it is possible to move towards cellular conditions of known aggregation promoting properties. Exposure to neurotoxic agents[27], such as rotenone[29, 325], or MPTP[28], for example, or conditions of nucleation-induced αSyn aggregation[192, 212] can now be employed to trigger intracellular aggregation processes of αSyn that are relevant for PD. Similarly, different metabolic stress scenarios, via induced mitochondrial impairment[288, 289] for example, or enhanced cellular oxidative stress[326, 327], changes in cellular Ca^{2+}-levels[209, 328], dysregulation of iron metabolism[329], or acidification[330, 331] can additionally be established to study the conformational properties of αSyn under various cellular conditions by *in-cell* NMR spectroscopy. This offers unique possibilities for future research projects into the underlying cellular events that cause this devastating disease.

4. Materials and Methods

4.1 Materials

4.1.1 Equipment

1. 750 MHz Bruker Avance spectrometer
2. 3 mm, 4 mm, 5mm Shigemi NMR tubes
3. Fast protein liquid chromatography (FPLC) system
4. Sephadex 75 Gel-filtration column (GE Healthcare, USA)
5. Sephadex 30 Gel-filtration column (GE Healthcare, USA)
6. Sephadex G-25 (Sigma Aldrich, USA)
7. Anion-exchange columns (GE Healthcare, USA)
8. Cation-exchange columns (GE Healthcare, USA)
9. PCR Thermal Cycler (Bio-Rad, USA)
10. NanoPhotometer (IMPLEN, USA)
11. Ni-NTA (Qiagen, USA)
12. Hemocytometer
13. Flow cytometry equipment (BD FACSCalibur, USA)
14. Standard gel electrophoresis equipment (Bio-Rad, USA)
15. Trans-Blot® Turbo Transfer system (Bio-Rad, USA)
16. Chemo-luminescence (ECL) detection (Bio-Rad, USA)
17. Inverted phase contrast microscope (Nikon TS100-F, Japan)
18. LSM UV confocal microscope (Zeiss, Germany)
19. CO_2 incubator
20. Amaxa Nucleofector® II and electroporation cuvettes (Lonza, USA)
21. CASY Model TT cell analyzer

4.1.2 Suppliers and reagents

22. DMEM low Glucose, 5mM Glutamine (PAA Laboratories, Canada)
23. DMEM high Glucose, 5mM Glutamine (PAA Laboratories, Canada)
24. DMEM/HAM F12, 5mM Glutamine (PAA Laboratories, Canada)
25. RPMI 1640, 5mM Glutamine (PAA Laboratories, Canada)
26. McCoy's 5a, 5mM Glutamine, (PAA Laboratories, Canada)

27. Opti-MEM 1 reduced serum medium (Invitrogen, USA)
28. Leibovitz's L-15 solution (Life technologies, GB)
29. Phosphate buffered saline (PBS), cell culture grade, without Calcium/Magnesium (PAA Laboratories, Canada)
30. Fetal Bovine Serum gold (FBSg) (PAA Laboratories, Canada)
31. 6-well cell culture plates/T175 cell culture flasks/14cm cell culture plates
32. 10x Trypsin/EDTA (0,5 % / 0,2 % in DPBS) (PAA Laboratories, Canada)
33. Collagen R solution (Serva, Tübingen, Germany)
34. Microscopy glass slides 30mm x 1.5mm, live imaging (Thermo Scientific, USA)
35. Microscopy glass slides 25mm x 1mm, immunostain (Thermo Scientific, USA)
36. Microscopy cover slip 76mm x 26mm, immunostain (Thermo Scientific, USA)
37. Fluorescence Mounting Medium (Dako, Germany)
38. Gelatin from cold water fish skin (Sigma Aldrich, USA)
39. Hoechst 33342 (Invitrogen, USA)
40. Anti - actin IgM (JLA20 Bioscienes, USA)
41. Anti-αSyn full length (FL) (sc-69977 Santa Cruz Biotechnology, California)
42. Anti-αSyn N-terminal (NT) (ab51252, Abcam, USA)
43. Anti-γSyn (ab6169, Abcam, USA)
44. Anti-Protein G (GB1) (ab6678, Abcam, USA)
45. Anti – mouse IgG Peroxidase Conjugate (A9917, Sigma Aldrich, USA)
46. Anti – rabbit IgG Peroxidase Conjugate (A6667, Sigma Aldrich, USA)
47. Anti – mouse IgG Atto488 (61197, Sigma Aldrich, USA)
48. Anti – Rabbit IgG Atto647N (40839, Sigma Aldrich, USA)
49. SuperSignal West Pico Chemiluminescent Substrate (34087 Thermo Scientific, USA)
50. SuperSignal West Femto Chemiluminescent Substrate (34094 Thermo Scientific, USA)
51. Atto647 NHS succinimide ester (07376, Sigma Aldrich, USA)
52. Atto488 NHS-succinimide ester (41698, Sigma Aldrich, USA)
53. 7-Aminoactinomycin (7-AAD) (Applichem, USA)
54. Trypan Blue (Sigma Aldrich, USA)
55. 1-pyrenebutyrate (PA) (Sigma Aldrich, USA)

56. Streptolysin O (SLO) from *Streptococcus pyogenes* (Sigma Aldrich, USA)
57. GSH (G6013-10G, Sigma Aldrich, USA)
58. ATP (Thermo Fisher Scientific, Canada)
59. Protease inhibitor coctail (Roche, USA)
60. Phosphatase inhibitor coctail (Roche, USA)
61. PLK3 (pCMV6-Entry) plasmid (OriGene, USA)
62. pRSET GFP plasmid (Invitrogen, USA)
63. FuGENE HD transfection reagents (Roche, USA)
64. 15N-ammonium-chloride (Cambridge Isotope Laboratories, England)
65. Bio-Rad Protein Assay dye (Bio-Rad, Germany)
66. Coomassie brillant blue G250 (Sigma Aldrich, USA)
67. Phusion DNA polymerase (Thermo Scientific, USA)
68. Phusion HF reaction buffer (5x) (Thermo Scientific, USA)
69. dPN1 (Biolabs, England)
70. Nucleotide solution mix (Biolabs, England)
71. LB broth powder (Sigma Aldrich, USA)
72. Recombinant Tev protease
73. Amicon filter-centrifugation devices (Millipore, USA)

4.1.3 Buffers

74. NMR buffer: 20 mM Potassium Phosphate, 150 mM NaCl, pH 6.4
75. CPP coupling buffer: 20 mM Phosphate, 150 mM NaCl, pH 7.0
76. HBSS buffer: 137 mM NaCl, 5.4 mM KCl, 0.25 mM Na_2HPO_4, 0.44 mM KH_2PO_4, 4.2 mM $NaHCO_3$, 0.1 % (w/v) D-glucose, 30 mM HEPES, pH 7.2
77. Membrane re-sealing buffer: HBSS buffer + 2 mM $CaCl_2$
78. Electroporation buffer: 5 mM KCl, 15 mM $MgCl_2$, 15 mM Hepes, 100 mM Na_2HPO_4/NaH_2PO_4 buffer, pH=7.2, sterile filtered
79. RIPA buffer: 50 mM Tris, 150mM NaCl, 0.1% SDS, 0.5% Na-Deoxycholate, 1% NP40
80. Hypotonic buffer: 10 mM K-phosphate pH=7.5, 1.5 mM Mg_2Cl
81. Fixation solution: 2.5% Para formaldehyde, 100 mM Cacodylate, 100 mM Sucrose, pH: 7.6
82. Fixation for Western blot: 4% Para formaldehyde

83. Permeabilization buffer: 0.1 % Tryton-X / PBS
84. *In-cell* NMR buffer: Leibovitz's L-15 solution (Life technologies, GB), 10 % FBSg, 10 % D_2O

4.1.4 Cell lines

Cell line	Cell type/Source	Sigma Aldrich Cat.No:	Media
A2780	Human ovarian carcinoma	93112519	RPMI/ 10% FBSg
B65	Rat nervous tissue	85042305	DMEM (high glucose)/10% FBSg
C6	Rat glial tumor	AG Ketterman	DMEM (high glucose)/10% FBSg
G261	Mouse glial tumor	AG Ketterman	DMEM (high glucose)/10% FBSg
HeLa	Human cervical carcinoma	93021013	DMEM (low glucose)//10% FBSg
MCF7	Human breast adenocarcinoma	86012803	DMEM (low glucose)//10% FBSg
Neuro2a	Mouse neuroblastoma	Jan Biske	DMEM (high glucose)/10% FBSg
NIH-3T3	Mouse fibroblast	Jan Biske	DMEM (low glucose)//10% FBSg
PC12	Rat adrenal gland	Jan Biske	RPMI/ 10% FBSg
PC3	Human prostate adenocarcinoma	90112714	HAM F12/10% FBSg
RCSN3	Rat *substantia nigra*	Dr. Pablo A. Caviedes	DMEM/HAM F12/10% FBSg
SHSY-5Y	Human brain neuroblastoma	Jan Biske	DMEM/HAM F12/10% FBSg
SK-N-SH	Human neuroblastoma	86012802	DMEM/HAM F12/10% FBSg
U2OS	Human osteogenic sarcoma	92022711	McCoy 5A/ 10% FBSg

4.1.5 Proteins

Name	Mw (Da)	pI	Amino acid sequence
hGFP	31475	5.81	MRGSHHHHHH GMASMTGGQQ MGRDLYDDDD KDRWGSEFAT MVSKGEELFT GVVPILVELD GDVNGHKFSV SGEGEGDATY GKLTLKFICT TGKLPVPWPT LVTTLTYGVQ CFARYPDHMK QHDFFKSAMP EGYVQERTIF FKDDGNYKTR AEVKFEGDTL VNRIELKGID FKEDGNILGH KLEYNYNSHK VYITADKQKN GIKVNFKTRH NIEDGSVQLA DHYQQNTPIG DGPVLLPDNH YLSTQSALSK DPNEKRDHMV LLEFVTAAGI TLGMDELYK

αSynuclein (wt)	14460	4.67	MDVFMKGLSK AKEGVVAAAE KTKQGVAEAA GKTKEGVLYV GSKTKEGVVH GVATVAEKTK EQVTNVGGAV VTGVTAVAQK TVEGAGSIAA ATGFVKKDQL GKNEEGAPQE GILEDMPVDP DNEAYEMPSE EGYQDYEPEA
βSynuclein (wt)	14288	4.41	MDVFMKGLSMAKEGVVAAAEKTKQGVTEAAEKT KEGVLYVGSKTREGVVQGVASVAEKTK EQASHLGGAV FSGAGNIAAATGLVKREEFPTDLKPEEVAQ EAAEEPLIEP LMEPEGESYEDPPQEEYQEYEPEA
γSynuclein (wt)	13331	4.89	MDVFKKGFSIAKEGVVGAVEKTKQGVTEAAEKTKE GVMYVGAKTKENVVQSVTSVAEKTK EQANAVSEAVVSSVNTVATKTVEEAENIAVTSGVV RKEDLRPSAPQQEGEASKEKEEVAEEAQSGGD
Hsp12	11750	5.22	GMSDAGRKGF GEKASEALKP DSQKSYAEQG KEYITDKADK VAGKVQPEDN KGVFQGVHDS AEKGKDNAEG QGESLADQAR DYMGAAKSKL NDAVEYVSGR VHGEEDPTKK
p53 (aa1-64)	7099	3.28	MEEPQSDPSV EPPLSQETFS DLWKLLPENN VLSPLPSQAM DDLMLSPDDI EQWFTEDPGP DEA
GB1 (wt)	6408	4.46	GAMGQYKLIL NGKTLKGETT TEAVDAATAE KVFKQYANDN GVDGEWTYDD ATKTFTVTE
Histon 3 (aa1-33)	4705	11.61	GSNARTKQTA RKSTGGKAPR KQLATKAARK SAPATGLGSE NLYFQ
CKII substrate	1622	3.99	*Gac(acetyl glycine)*-RRRADDSDDD DDGGG

4.2 Methods

4.2.1 Site directed mutagenesis of αSynuclein

Site directed mutagenesis of αSynuclein (αSyn) was carried out by restriction free cloning. The pT7-7 αSyn template plasmid was used for mutagenesis. The protein coding sequence is highlighted in grey. Primers are designed as complementary sequences of the blue and black or green and black sequences located on the plasmid.

Agcgaggaagcggaagagcgcctgatgcggtattttctccttacgcatctgtgcggtatttcacaccgcataggaagatcttccggaagatcttcctatg
gtgcactctcagtacaatctgctctgatgcgctacgtgactgggtcatggctgcgccccgacacccgccaacacccgctgacgcgccctgacgggctt
gtctgctcccggcatccgcttacagacaagctgtgaccgtctccgggagctgcatgtgtcagaggttttcaccgtcatcaccgaaacgcgcgaggccca
gcgattcgaacttctgatagacttcgaaattaatacgactcactatagggagaccacaacggtttccctctagaaataatttttgtttaa**ctttaagaaggag**
atatacatatg**gatgtattcatgaaaggac**tttcaaaggccaaggagggagttgtggctgctgctgagaaaaccaaacagggtgtggcagaagcag
caggaaagacaaaagagggtgttctctatgtaggctccaaaaccaaggagggagtggtgcatggtgtggcaacagtggctgagaagaccaaagagc
aagtgacaaatgttggaggagcagtggtgacgggtgtgacagcagtagcccagaagacagtggagggagcagggagcattgcagcagccactggc
tttgtcaaaaaggaccagttgggcaagaatgaagaaggagccccacaggaaggaattctggaagatatgcctgtggatcctgacaatgaggcttatga
aatgccttctgaggaagggtat**caagactacgaacctgaagcc****taagaaatatctttgctccc**agtttcttgagatctgctgacagatgttccatccaa
gcttatcgatgataagctgtcaaacatgagaattaaatcaatctaaagtatatatgagtaaacttggtctgacagttaccaatgcttaatcagtgaggcacct
atctcagcgatctgtctatttcgttcatccatagttgcctgactccccgtcgtgtagataactacgatacgggagggcttaccatctggccccagtgctgcaa
tgataccgcgagacccacgct

Primer design

1. N-terminal cysteine mutant:

As we needed to introduce only one amino acid, the forward primer was designed to be complementary to the 5' end of the desired point of insertion on the template. The

primer contained a **24 base overlap** with the template plasmid, where the insertion occurred right after the start codon (ATG). The TGC codon (cys residue) was added to the primer, followed by a 19 base overlap on the template. The reverse primer sequence was designed accordingly.

Forward primer (5'- 3'): ctttaagaaggagatatacatatgtgcgatgtattcatgaaaggac

Reverse primer (3'- 5'): gtcctttcatgaatacatcgcacatatgtatatctccttcttaaag

2. C-terminal cysteine mutant:

Similarly, as we needed to introduce only one amino acid, the forward primer was designed to be complementary to the 3' end of the desired point of insertion on the template. The primer contained a **21 base overlap** with the template plasmid, where the insertion occurred right before the stop codon (ATG). The TGC codon (cys residue) was added to the primer, followed by a 20 base overlap on the template. The reverse primer was designed accordingly.

Forward primer (5'- 3'): caagactacgaacctgaagcc**tgc**taagaaatatctttgctccc

Reverse primer (3'- 5'): gggagcaaagatatttcttagcaggcttcaggttcgtagtcttg

PCR reaction: 50 µl PCR reaction mix was prepared using 50 ng of template plasmid, 200-200 ng of primers, 1 µL of 10 mM nucleotide solution mix, in Phusion HF reaction buffer. 1µL Phusion DNA polymerase (2.5 U/µL) was added to the solution. Hot start initiation was applied, as the polymerase enzyme was only added when the reaction temperature reached 98 °C. With this, non-specific product formation could be reduced or eliminated, before high-temperature cycling. Applied PCR conditions were: initiation: 98 °C, 2 min; denaturation: 98 °C, 30 sec; annealing: 55 °C, 1 min; elongation: 72 °C, 10 min (2 min/kb), where 35 cycles were run.

Dpn1 digestion: The double stranded PCR product was digested with restriction endonuclease (Dpn1) enzyme at 37 °C for 3-6 h. Dpn1 cleaves methylated DNA that is only present in the template plasmid.

Transformation and expression tests: 5 µL from the PCR product were transformed into ~50 µL of *E.coli* BL21(DE3)-Express electro-competent cells. Cells were plated onto antibiotic containing LB-agar pates and incubated over-night at 37 °C. Individual colonies were picked and grown separately in 1 mL antibiotic containing LB at 37 °C

until optical density at 500 nm (OD_{500}) was ~0,6-0,8. Protein expression was induced by addition of 1.0 mM isopropylthio-β-D- galactoside (IPTG) at 37 °C, for 3 h. Colonies with good expression yields were used for plasmid preparation. Mutations were confirmed by DNA sequencing (Invitek GmbH). Plasmids were stored at -20 °C in sterile, DNA free distillated water at ~100-400 ng/μL concentrations.

4.2.2 Recombinant protein expression

For recombinant protein expression, ~50 μL of *E.coli* BL21(DE3)-Express electro-competent cells were transformed with 50-100 ng protein coding plasmids by standard DNA electroporation. pT7-7 (αSyn), pET30a (β-, γSyn), pET (all GB1 constructs), pDUET (Hsp12, p53(aa1-64), H3(aa1-33), pRSET-EmGFP (GFP) plasmids were used for transformations. N-terminal acetylated αSyn (AcαSyn) was obtained by co-transformation of pT7-7 (αSyn) and pACYduet (NatB) plasmids into *E.coli* BL21(DE3)-Express cells. The pACYduet vector was a kind gift from the Mulvihill lab[332]. Cells were plated onto antibiotic containing LB-agar pates and incubated over-night at 37 °C. Colonies were picked and grown as overnight cultures typically in 20 mlL of antibiotic containing LB at 37 °C for 12-15 h.

In case of non-isotope labeled protein expression, a 10 mL overnight culture was inoculated into 500 mL antibiotic containing LB, and grown with shaking (~150 rpm) at 37 °C until an OD_{500} of ~ 0.6 - 0.8 was reached. Protein expression was induced by addition of 1 mM isopropylthio-β-D- galactoside (IPTG) at 37 °C, for 3-5 h, or - in case of the Synuclein family of proteins- overnight at 30 °C. Cells were collected by centrifugation (10 minutes, 6000 rpm, 4 °C).

For isotope labeling, a 10 mL of overnight culture was centrifuged (4000 rpm, room temperature) and re-suspended into 500 mL of isotope labeled M9 minimal medium, supplemented with ^{15}N-NH_4Cl salts. Production of AcαSyn was carried out by co-expression of both αSyn and NatB proteins as reported previously[229].

4.2.3 Recombinant protein purification

Purification of the Synuclein family of proteins (α-, β-, γSyn): Purification of recombinant Synuclein proteins, (including AcαSyn), was performed as previously reported[23, 333]. Protein samples were dissolved in NMR buffer at concentrations of ~1 mM, flash frozen and stored at -80 °C. The same protocol was applied for the

purification of cys-containing αSyn mutant in the presence of 1 mM DTT in each of the purification steps.

Synthetic Casein Kinase II (CKII) substrate peptide: A CKII substrate peptide (13 residues)[334] was purchased from Biosyntan (Berlin, Germany).

Purification of the His_6-tagged proteins (GFP, Hsp12, p53, GB1, histone H3): Hsp12, GFP, GB1 and p53 (aa1-64), histone H3 (aa1-33) proteins were expressed as N-terminal 6xHis-tag fusions, followed by a TEV protease site and purified by Ni-NTA, ion exchange (Resource Q or Resource S) and size exclusion (Superdex 75) chromatography[335]. The 6xHis-tag was removed by TEV proteolysis after the first Ni-NTA purification step. The same protocol was applied for the purification of the cys-containing GB1 constructs in the presence of 1 mM DTT in each of the purification steps. hGFP protein was purified similarly to other His6-tagged proteins, without removal of the His-tag. Ni-NTA elutes were concentrated and further purified by gel filtration (Sephadex 75). Final samples were concentrated to ~1 mM in NMR buffer.

4.2.4 CPP production by solid phase peptide synthesis

The Tat-HIV (aa47-57) peptide was produced by solid-phase peptide synthesis (SPPS) in collaboration with Dirk Schwarzer (Protein Chemistry, FMP). In order to covalently couple the CPP moiety to cargo proteins, cysteine residues were added to the N- and C-terminal positions of the original protein sequences. To enhance coupling efficiencies, cysteines of the CPPs were activated via S-3-nitro-2-pyridinesulphenyl (Npys). An additional fluorescence dye was also incorporated for in-cell detection by microscopy methods. Products were purified by reversed-phase HPLC and stored as lyophilized powders at 4 °C.

4.2.5 Covalent coupling of CPP and proteins

N-, or C-terminal cysteine-containing recombinant cargo proteins were produced (see *Recombinant protein purification*) and concentrated to ~2 mM in volumes of 2 mL.
The following cys-mutant cargo protein were employed for the respective coupling reactions:

Cargo	Amino acid sequence	Mw (kDa)	pI
N-Cys GB1	CGGQYKLILN GKTLKGETTT EAVDAATAEK VFKQYANDNG VDGEWTYDDA TKTFTVTE	6308	4.55
C-Cys GB1	QYKLILNGKT LKGETTTEAV DAATAEKVFK QYANDNGVDG EWTYDDATKT FTVTEGGC	6308	4.46
N-Cys αSyn	MCDVFMKGLS KAKEGVVAAA EKTKQGVAEA AGKTKEGVLY VGSKTKEGVV HGVATVAEKT KEQVTNVGGA VVTGVTAVAQ KTVEGAGSIA AATGFVKKDQ LGKNEEGAPQ EGILEDMPVD PDNEAYEMPS EEGYQDYEPEA	14563	4.67
C-Cys αSyn	MKGLSKAKEG VVAAAEKTKQ GVAEAAGKTK EGVLYVGSKT KEGVVHGVAT VAEKTKEQVT NVGGAVVTGV TAVAQKTVEG AGSIAAATGF VKKDQLGKNE EGAPQEGILE DMPVDPDNEA YEMPSEEGYQ DYEPEAC	14071	4.74

Lyophilized Tat-HIV peptides were dissolved in coupling buffer and the pH was re-adjusted to 7.0. CPPs were applied in 1:2 and 1:4 molar excess to perform the coupling reactions with Cys-modified GB1 and αSyn, respectively. Coupling reactions were performed in 200 µL volumes in the presence of 4 mM CPPs ($8*10^{-8}$ mol) by addition of 200 µL of 1 mM Cys-αSyn ($2*10^{-8}$ mol), or 200 µL of 2 mM Cys- GB1 ($4*10^{-8}$ mol), at room temperature, for 10 min, 30 min and 1 h of incubation times.

Samples were taken at different time points and analyzed by SDS-PAGE. Successful coupling was assessed by the appearance of the desired CPP-cargo protein band. Because CPP moieties contained fluorescence dyes, coupling efficiencies were determined by UV illumination, before the gel was stained with Coomassie. CPP-cargo, cargo-cargo, uncoupled cargo, free CPP and CPP-CPP dimer ratios were determined by their individual Coomassie/fluorescence intensities. Coupled CPP-cargo constructs were separated from unwanted species on a PD G-25 size exclusion column (Mw: 5000 Da). Fractions containing the desired CPP-cargo construct were collected and concentrated by amicon filter-centrifugation with 3000 Da cut-off membranes.

4.2.6 Fluorescence labeling of cargo proteins

Proteins of interest were recombinantly expressed and purified as outlined above. NHS ester-activated Atto fluorescence dyes were reacted with lysine primary amines of the different proteins, yielding covalently labeled cargo probes, according to manufacturers instructions (i.e. Atto488 and Atto647). Labeled products were separated from non-reacted dyes on a Sephadex G-25 column and concentrated with Millipore concentrators. Fluorescently labeled products were assessed by UV/VIS spectrophotometry considering a correction factor at 280 nm for specific absorbances

of the fluorophores ($CF_{Atto\ 488}$: 0.1, $CF_{Atto\ 647}$: 0.042).

4.2.7 Cell culture and handling

Most of the cell lines used in this study were purchased from Sigma Aldrich. RCSN3 cells were provided by Dr. Pablo A. Caviedes (Center for Clinical Research & Pharmacological Studies, Univ. of Chile). G261, C6 cell lines were obtained from Prof. Dr. Helmut Kettenmann (Max-Delbrück-Center for Molecular Medicine, Berlin). Finally, Neuro2a, NIH-3T3, PC12 and SHSY-5Y cells were kind gifts of Jan Bieschke (Max-Delbrück-Center for Molecular Medicine, Berlin). Cell lines were cultured in complete media and kept at 37 °C in 5 % CO_2 incubators. Cells were grown to 70-80 % confluence and harvested upon 0.25 % Trypsin/EDTA treatment for 5 minutes at 37 °C. Trypsin was neutralized with 5x volume of complete media and cell suspensions were further applied for sub-culturing or analysis. All cell lines were passaged no more than 6-12 times before the experiments.

4.2.8 Protein delivery techniques

Protein delivery via Cell Penetrating Peptides: Small-scale trials and sample preparations for immunofluorescence experiments were performed in 6-well plates. 2.5-3 x 10^5 cells were seeded into each well, 24 h prior to the CPP delivery experiment. Treatments were carried out at ~80 % confluence (~ 5-6 x 10^5 cells).

To determine cytotoxity levels of un-conjugated CPPs, Tat-HIV (aa47-57) peptide solutions were prepared at concentrations of 5- 10- and 50 μM in 500 μL PBS. For protein uptake experiments, 50 μM CPP-cargo solutions were prepared in 500 μL PBS.

Prior to uptake experiments, culture media were removed from cells and cultures were washed with 3 mL per well of pre-warmed PBS. Cultures were exposed to un-conjugated CPP or to 50 μM CPP-cargo solutions (500 μL) for 60 minutes at 37 ºC in a CO_2 incubator. Following this treatment, CPP, or CPP-cargo solutions were removed. Cells were washed twice with pre-warmed PBS and complete media were added to each well (2 mL per well). Cells were allowed to recover for 1 h at 37 ºC in a CO_2 incubator.

In case of 1-pyrenebutyrate (PA) pre-treatment, a 100 mM PA stock was prepared in DMSO and stored at -20 ºC. From this stock, further dilutions (1 mM) were made in PBS and stored in small aliquots at -20 ºC. 50 μM of PA was diluted into 500 μL PBS.

Cells were exposed to this solution for 10 min at 37 ºC. After this procedure, cells were washed once with pre-warmed PBS and incubated with 50 μM CPP-cargo/PBS solutions in the presence of 50 μM PA. Cells were washed again and allowed to recover for 1 h in complete media.

Following recovery, cells were washed once with pre-warmed PBS, and harvested by 0.25 % Trypsin/EDTA treatment (5 min at 37 ºC) for flow cytometry analyses (see *Imaging techniques*). In case of confocal microscopy analysis, identical treatments were performed with cells grown on 30 mm x 1.5 mm glass slides. Live imaging of treated cells was carried out after 1 h recovery period.

Protein delivery by Streptolysin O (SLO): Small-scale trials and sample preparations for immunofluorescence experiments were carried out in 6-well plates. Small-scale trials were performed with 2.5 - 3 x 10^5 cells per well, seeded into 6-well plates, 24 h prior to the SLO delivery experiment. Cells were ~80% confluent at the beginning of the experiment (~5-6 x 10^5 cells).

SLO was purchased as a lyophilized powder, prepared from 10 mM Tris, 3 mM Na-azide, 5 mM, EDTA, 1 mM PMSF solutions. The powder was directly re-suspended in distilled H_2O (0.2 μg/μL) and stored as flash frozen aliquots at -20 °C. For preparing working solutions, this stock was diluted into HBSS buffer. Dilution series of SLO toxin concentrations (10-20-50 ng/mL) corresponding to 14-28-70 U/mL of SLO were prepared in HBSS buffer in 500 μL volumes per sample. Fluorescently labeled cargo (see *Fluorescence labeling of cargo constructs*) proteins were diluted into this HBSS solution at 50-200 μM concentrations in 500 μL volumes per sample.

Prior to uptake experiments, culture media were removed from cells and cultures were washed with 3 mL per well of pre-warmed PBS and 2 x 3 mL per well of ice-cold HBSS, in order to adjust cells to the subsequent incubation routines. To initiate SLO-mediated pore formation, HBSS was discarded and SLO/HBSS solutions were added onto cells. Following 30 min incubation at 4 ºC, excess SLO was removed by washing cells with 3 mL per well of ice-cold HBSS.

Next, fluorescently labeled protein/HBSS solutions were added to cells. Cultures were transferred into a CO_2 incubator (37 ºC) for 30 min to initiate protein uptake. In case of maximum tolerable SLO concentration measurements, cells were incubated with 500 μL per well of fresh HBSS solutions in the absence of proteins.

Incubation was followed by repeated washes with HBSS (2 x 3 mL per well) and Ca^{2+} supplemented HBSS (2 x 3 mL per well), respectively. To reseal SLO pores, cells were further incubated with 2 mM Ca^{2+}/HBSS buffers for 30 min at 4 °C. Incubation was followed by a 2 mL per well pre-warmed PBS wash. Similar to the CPP-treatment, cultures were allowed to recover for 1h in fresh complete media in a CO_2 incubator.
Following recovery, cells were washed once with pre-warmed PBS and harvested by 0.25 % Trypsin/EDTA treatment (5 min at 37 ºC) for flow cytometry analyses (see *Imaging techniques*). In case of confocal microscopy analysis, identical treatments were performed with cells grown on 30 mm x 1.5 mm glass slides. Live cell imaging of treated cells was carried out after a 1 h recovery period.
For dithiothreitol (DTT) activated SLO treatments, identical procedures were performed, where SLO/HBSS incubations were done in the presence of 5 mM DTT.

Protein delivery by electroporation: Depending on the scale of the experiment, 1-6 T175 flasks of cultured cells were prepared by initially seeding 4-5 x 10^6 cells into each T175 flask, 24 h prior to the experiment. Typically 1-2 T175 flasks were prepared for small-scale experiments, 4-6 T175 flasks cells for *in-cell* NMR experiments. Treatments were carried out at ~80 % confluence (~ 0.8 – 1x10^7 cells per T175 flask).
Experiments were done using: a) fluorescently labeled (for flow cytometry analyses and live cell confocal imaging), or b) non-labeled (for Western blot analysis and immunofluorescence and immunoelectron microscopy), or c) ^{15}N isotope-labeled (for *in-cell* NMR experiments) purified, recombinant proteins.
Recombinant proteins were diluted to final concentrations between 50 µM and 800 µM in sterile filtered, freshly-prepared electroporation buffers at pH 7.2.
Cell culture dishes (6-well plates for small-scale experiments, or 14 cm diameter plates for *in-cell* NMR experiments) for cell recovery were prepared by the addition of 1 mL (for 6-well plates) or 5 mL (for 14 cm diameter plates) of complete media. Culture dishes were pre-warmed at 37 °C in CO_2 incubators.
For some cell types (see *Table 3* in *Results* section), collagen R solution coated 6-well plates/14 cm diameter plates were used for better attachment of cells. Collagen coating was performed 16-24 h prior to experiments with 0.2 mg/mL collagen solutions, diluted in 10% ethanol. Coated plates were dried at room temperature and washed 3 times with 10 mL of PBS before use.

Prior to uptake experiments, cells were harvested by 0.25 % Trypsin/EDTA treatment for 5 min, at 37 °C. Trypsin was neutralized with 5x volumes of complete medium. Cell pellets were sedimented by low speed centrifugation (~200 g for 10 min at 25 °C) and washed with 5-10 mL of pre-warmed PBS. For *in-cell* NMR experiments, ~ 15 µL samples were taken at this point for Trypan Blue viability assessments (see *Quality controls experiments for in-cell NMR samples*). Cell densities of these suspensions were adjusted to $2x10^6$ cells/mL with PBS. 1-1 mL of cell suspensions were aliquoted into multiple samples in Eppendorf tubes ($2x10^6$ cells/mL). Cells were pelleted by low speed centrifugation at ~200 g for 6 min at 25 °C and supernatants were discarded.

100 µL of the protein electroporation mixtures were added to each of the cell pellets and gently mixed with a plastic pipette. For control experiments, and to test the effects of multiply EP pulses, cells were electroporated with electroporation buffer only.

Cell suspensions were transferred into electroporation cuvettes (100 µL per cuvette) with a plastic pipette. Protein electroporation was performed with the Amaxa Nucleofector® I machine. Optimized Amaxa Nucleofector® I pulse programs were used for each cell line: Program B28 for A2780 and HeLa cells, G16 for B65, RCSN3 and SK-N-SH cells, T013 for PC3 cells, T09 for Neuro2a cells and X001 for U2OS cells. Cells were pulsed two times with gentle mixing in between pulses. Directly after electroporation, 1mL of pre-warmed (37 °C) and CO_2 saturated complete media was added to each cuvette and samples were transferred directly into the prepared cell culture dishes. Typically, 1 EP sample was placed onto each well of a 6-well plate, for small-scale experiments. For *in-cell* NMR experiments, 3-4 EP samples were applied onto one 14 cm diameter dish.

Plates were returned to CO_2 incubators for 4-5 h of recovery. During this time, recovery efficiencies and cell morphologies were assessed at regular intervals by phase-contrast light microscopy. After 2 h of recovery, additional complete media were added to the dishes, 2mL per 6-well plate, or 5 mL per 14 cm diameter plate. After 4-5 h of recovery, recovery media including the non-attached cells were removed. Cultures were washed 3 times with PBS (3 mL per well for small-scale experiments, 10 mL per 14 cm plate for *in-cell* NMR experiments) and harvested with 0.25 % Trypsin/EDTA, by incubation for 5 min, at 37 °C. Trypsin was neutralized with complete medium and cells were pelleted by low-speed centrifugation at 200 g for 6 min at 25 °C.

For small-scale experiments, cell pellets were washed once with 1 mL PBS and prepared for flow cytometry analyses (see *Imaging techniques*). For non-attached cell viability measurements (see *Cell morphology and viability*) recovery media including non-attached cells were collected. Each sample was pelleted in 15 mL Falcon tubes by low speed centrifugation at ~200 g for 6 min at 25 °C and washed 3 times with 10 mL PBS. Supernatants were discarded and cell pellets were prepared for flow cytometry analyses (see *Imaging techniques*). For live cells imaging by confocal microscopy, identically sets of treated cells were plated onto 30 mm x 1.5 mm glass slides. Live cell imaging was carried out after a 3 h recovery period (see *Imaging techniques*). For fixed cell immunofluorescense analyses, identically sets of treated cells were plated onto 25 mm x 1mm glass slides and allowed to recover for 5 h. Following this procedure, glass slides were washed with 2 mL PBS and treated briefly with 0.25 % Trypsin/EDTA for 40 s at room temperature. Trypsin was removed and 5 mL complete media were added to each well containing the glass slides. Detailed immunostaining protocols are described in the *Imaging techniques* section. For *in-cell* NMR experiments, combined cell pellets were washed with 15 mL PBS and prepared for NMR analyses (*see In-cell NMR sample preparation*).

4.2.9 Imaging techniques

Confocal microscopy: Confocal microscopy imaging was performed on live cells in the case of CPP-cargo delivery trials via detection of the CPP fluorescein fluorophores. For SLO-mediated delivery procedures and for protein electroporation, Atto647-, and Atto488-labeled recombinant proteins were visualized, respectively. Images were taken with a 100 x objective (N.A.1.3) and excitation by an argon laser working at a wavelength of 633 nm, or 488 nm, respectively, on a Zeiss LSM UV confocal microscope.

Fixed cell confocal microscopy was performed on cells electroporated with non-labeled Synuclein proteins. After electroporation, cells were allowed to recover for 5 h in a CO_2 incubator (37 °C, 5% CO_2) on 25 mm x 1mm glass slides. Cells were briefly Trypsin treated and washed with PBS, as described above. Samples were fixed with fixation solutions for 15 min and permeabilized with 0.1 % Triton-X/PBS solution, for 3 min. After extensive washing (3 times for 10 min with PBS and gentle shaking), samples were blocked with 0.13 % of gelatin from cold water fish skin for 1 h. Slides were then incubated for 2 h in 0.13 % of gelatin from cold water fish skin with 1:100

anti-αSyn FL (sc-69977) for detection of αSyn, 1:200 anti-αSyn N-terminal (ab51252) for detection of βSyn, 1:100 anti-γSyn (ab6169) for detection of γSyn. Slides were washed 3 times for 10 min with PBS and incubated with anti-mouse IgG Atto488, or Rabbit IgG Atto647N (61197/40839) for 1.5 h at 1:1000 dilutions in 0.13 % gelatin from cold water fish skin. After secondary antibody incubation, slides were washed 3 times for 10 min with PBS and stained with 2 µg/mL Hoechst 33342 in PBS for 15 min. Images were taken with a 100x objective (N.A.1.3) and with fluorophore excitation via argon lasers operating at 488 nm or 633 nm wavelengths, respectively, on a Zeiss LSM UV confocal microscope.

Immunoelectron microscopy: Immunoelectron microscopy was performed by Dr. Dorothea Lorenz (Cellular Imaging, FMP). HeLa and RCSN3 cells (control and αSynuclein electroporated), were fixed with 4 % paraformaldehyde and 0.2 % glutaraldehyde in 0.1 M phosphate buffer for 1.5 h at room temperature. After removing the fixatives, cells were washed several times with 0.1 M phosphate buffer and free aldehydes were quenched at room temperature with 100 mM glycine in 0.1 M phosphate buffer. Cells were scraped into 0.1 M phosphate buffer, centrifuged at 3500 g for 5 min and cell pellets were cryoprotected for 5 h at 37° C in a mixture of 1.8 M sucrose and 20 % polyvinylpyrrolidone (PVP) (K 25, Fluka) in 0.1 M phosphate buffer. Aliquots of 5 µL cryoprotected cells were mounted onto specimen holder pins and plunge frozen in liquid propane. Ultrathin cryosections (60 nm) were obtained according to Tokuyasu[336] using a cryo-ultramicrotome (EM FC6, Leica Microsystems). Sections were immunolabeled with αSyn FL antibody (sc-69977), 1:200 diluted in a washing phosphate buffered saline containing 1 % BSA for 1h, and subsequently with gold (12 nm) labeled goat anti-mouse IgG (Dianova, dilution 1:30) for 0.5 h according to standard procedures. Finally, cryo-sections were contrasted using a mixture of 3 % tungstosilicic acid hydrate (Fluka) and 2.5 % PVA (Sigma) according to Kargel *et al.*[337]. Cell sections were dried and viewed on a 80 kV ZEISS 902 A electron microscope (HeLa cells), or on a 200 kV Tecnai FEG F20 electron microscope (RCSN3 cells) with a Gatan 2k x 2k CCD camera.

Flow cytometry analysis: CPP-, SLO and electroporation mediated protein deliveries were carried out on 6-well plates (see *Protein delivery techniques*) with fluorescently

labeled cargo proteins. Treated cells were washed and harvested by the addition of 200 µL of 0.25 % Trypsin/EDTA solutions. Trypsin was neutralized by 5x volumes of complete media and suspensions (~1 mL) were transferred into Eppendorf tubes. Cells were sedimented by low speed centrifugation (200 g, 5 min) at 4 °C, and washed with 1 mL PBS. Cell pellets were resuspended in 500 µL, 2 µg/mL of 7-AAD (Applichem, USA)/PBS viability solutions, and kept at 4 °C for 5 min.

Dual-channel flow cytometry was performed on fluorescently labeled proteins (FL2 channel, 530 nm) and 7-AAD (FL3 channel, > 630 nm) on a FACSCalibur (BD, USA). Data were analyzed with FlowJo (version 8.8.6). Mono-labeled samples were used to define the compensation matrix.

4.2.10 Lysate preparations and Western blot analysis

Endogenous αSyn detection: 1-2 T175 flasks of cultured cells were prepared (~ 4-5 x 10^6 cells seeded into each flask) from each of the NMR cell models, 24 h prior to the experiment.

Cells were harvested by treatment with 0.25 % Trypsin/EDTA for 5 min at 37 °C. Trypsin was neutralized with complete medium and total cell counts were determined in a hemocytometer counting chamber. Depending on the cell type, 10-20 million cells were obtained and pelleted by centrifugation at 200 g for 6 min at 25 °C. Pellets were transferred into RIPA buffer with freshly added Complete Protease inhibitor cocktail (1x) and PhosphoStop phosphatase inhibitors (1x) and lysed by 4 repetitions of water-bath sonication for 20 seconds each. The lysates were cleared by centrifugation at 16800 g for 30 min at 4 °C and concentrations of soluble lysate fractions were determined by Bradford assays. 200 µg of total protein per sample were loaded onto a gradient SDS-PAGE (4-18%). Loading of 100 ng recombinant αSyn was used as a control reference. After gel electrophoresis, proteins were transferred onto PVDF membranes using the Trans-Blot® Turbo Transfer system (Bio-Rad). Membranes were fixed in 4 % PFA/PBS for 1 h and washed 2 time for 5 min in PBS and TBS. After blocking for 1 h in 5 % dry-milk/TBST, membranes were probed with either 1:100 anti-αSyn FL, or 1:5000 anti-actin IgM followed by 1:10000 anti–mouse HRP-coupled antibodies. Membranes were developed using the SuperSignal West Femto Chemiluminescent detection kit. Chemiluminescence signals were detected on a BioRad Molecular Imager.

In case of re-analyses of HeLa and RCSN3 samples, both lysates were boiled at 95 °C, for 10 min. Samples were cleared by centrifugation at 16800 g for 30 min at 4 °C and concentrations of the soluble lysate fractions were determined by Bradford assays. Western blot detection of αSyn was carried out as described earlier.

Detection of intracellular EP-delivered αSyn: Small-scale electroporation experiments were performed on 2 million cells with non-labeled protein. 400 µM of αSyn stock solutions were electroporated into mammalian cells. Cells were transferred onto 6-well plates and allowed to recover for 5 h at 37 °C under 5 % CO_2. Recovered cells were washed with PBS for 3 times (5 mL per well) before they were harvested by treatment with Trypsin/EDTA.
Total cell counts and lysate preparations were preformed as indicated above. 15-30 µg of total protein per sample were loaded onto gradient SDS-PAGE (4-18 %). A dilution series of 10-400 ng of recombinant αSyn was loaded as reference to generate the individual calibration curves. Western blot detection of αSyn was carried out as described above.

Native PAGE on RCSN3 in-cell lysates: 200 ng of monomeric αSyn and 200 ng of 'monomer equivalent' high-, and low- molecular weight αSyn oligomers and of αSyn amyloid fibrils were used as reference inputs. αSyn fibrils were prepared by the standard shaking protocol in the presence of glass beads at 37 °C for 24 h[23]. Control samples and 15 µL of the RCSN3 *in-cell* NMR lysates were mixed with bromophenol blue sample buffer and loaded onto a native PAGE (18 %). Protein transfer and detection with anti-αSyn FL antibodies was performed as described above.

Native PAGE of αSyn monomers, fibrils and electroporated HeLa cell lysates: Small-scale electroporation experiments were performed on 2 million HeLa cells with 250 µM of non isotope-labeled αSyn monomers and αSyn fibrils. Cells were transferred onto 6-well plates and allowed to recover for 5 h at 37 °C in 5% CO_2. Non-attached cells were collected and transferred into a 15 mL Falcon tube. Non-attached cells were pelleted by low-speed centrifugation (200 g) and washed 3 times with PBS (10 mL per tube) before lysate preparation. Reattached cells were washed 3 times with

PBS (3 mL per well) before being harvested by treatment with Trypsin/EDTA. Both cell populations (reattached and non-attached) were lysed in hypotonic buffer and mixed with bromophenol blue. 30 µg of total protein per sample and 200 ng of monomeric and fibril αSyn reference samples were loaded onto a native PAGE (18 %). Samples were transferred onto PVDF membranes and detected with anti-αSyn FL antibodies as described above.

***In-cell* NMR lysate preparation:** After each *in-cell* NMR experiment, sedimented cells were carefully resuspended in the remaining supernatant and transferred into a 1.5 mL Eppendorf tube. Cells were then pelleted by low-speed centrifugation (200 g) for 5 min at 4 °C. The resulting supernatant was re-analyzed by NMR spectroscopy and/or Western blotting. After these procedures, 100 µL of the supernatant was added back to the cells and samples were lysed by placing them in a water-bath sonicator for three rounds of 20 seconds ultra-sound lysis at 4 °C. The lysates were cleared by centrifugation at 16800 g for 30 min at 4 °C. Soluble fractions were returned to the NMR tube and extract NMR spectra were recorded with identical acquisition settings as for *in-cell* NMR samples.

4.2.11 Calculating intracellular αSyn concentrations

Intracellular αSyn levels of the NMR cell models, enriched by protein electroporation, were determined by semi-quantitative Western blotting. Lysates of different cell lines were made with known cell numbers (N_{cell}): $0.13x10^6$ cells per 40 µL of lysates. Lysates were separated by SDS-PAGE along with reference samples of 10-400 ng of αSyn. Gels were transferred onto PVDF membrane and probed for αSyn as described above. After ECL detection, the ImageLab quantification software was used to determine individual chemiluminescent intensities and comparatively analyzed with respect to signal intensities of reference αSyn samples (i.e. reference calibration curves). Per cell concentrations of delivered αSyn (in µg) were determined for each *in-cell* NMR sample.

αSyn concentrations in these cell lysates were calculated with the following equation: αSyn $C_{lysate} = m_{lysate} / V_{lysate}$, in which m_{lysate} is the amount of αSyn (in µg) divided by the total loaded lysate volume (V_{lysate}). To convert this ratio into an intracellular protein

concentration we had to calculate the total dilution of cells within the lysates in relation to the sums of their cellular volumes V_{cell} i.e. with the dilution factor $f = V_{lysate} / V_{cell}$ for each of the cell types. The sum of all cell volumes is given by $V_{cell} = V_{single\ cell} * N_{cell}$. $V_{single\ cell}$ and N_{cell} were experimentally determined using the CASY Model TT cell analyzer. Based on these relations final intracellular αSyn concentrations were calculated as $C_{int} = C_{lysate} * f$. From this, intracellular protein concentrations in molar terms were determined by taking into account the molecular weight of αSyn (MW =14.500 Da). Intracellular αSyn concentrations were calculated from two independent experiments. Endogenous αSyn concentrations of the NMR cell models were calculated similarly. αSyn Western blot intensities were measured in lysates of non-electroporated cells and compared to signal intensities of reference αSyn samples.

Calculating effective *in-cell* NMR αSyn concentrations:

The term effective NMR concentration (C_{eff}) denotes the sum of all NMR signals that are detected by *in-cell* NMR experiments. This concentration is based on the number of cells within the *in-cell* NMR sample that are 'seen' by the receiver coil of the NMR spectrometer (i.e. inside the volume of the receiver coil in the NMR probe) containing different levels of intracellular αSyn. A packing defect, dilution factor has to be taken into account that results from the fact that cell-type specific intracellular volumes, harboring the isotope labeled proteins do not correspond to the macroscopic volumes that individual cells take up in the NMR sample tube. This packing defect dilutes the effectively measured NMR concentration in molar terms.

As the total number of cells in each *in-cell* NMR specimen had been determined by cell counting prior to the NMR experiment and because intracellular αSyn concentrations had been evaluated for each sample, these packing-related dilution factors can be described as: $D = (N_{cell} * V_{cell}) / V_{NMR}$, where N_{cell} is the number of cells within the NMR receiver coil volume, V_{cell} is the volume of a single cell as determined with the CASY cell analyzer and V_{NMR} is the exact volume that these cells occupy in the NMR receiver coil volume. Effective NMR concentrations (C_{eff}) were calculated by multiplication of intracellular αSyn concentrations with this dilution factor.

4.2.12 αSyn phosphorylation in PLK3 over-expressing cells

PLK3 transfection: $2x10^5$ cells were seeded into 6-well plates 24 h before transient transfection to reach ~60 % confluence. 3 µg of pCMV6-Entry (PLK3) plasmid was diluted into 100 µL Opti-MEM solution and mixed with 9 µL FuGENE solution. This mixture was incubated at room temperature for 20 min before being added to cells in another 1.9 mL of Opti-MEM. Cells were returned to the CO_2 incubator for 5 h. After this time, transfection solution was removed and complete media were added.

Lysate preparation: After 18 h of transient PLK3 over-expression, cells were washed and harvested by treatment with 0.25 % Trypsin/EDTA. For lysates, cells were incubated in hypotonic buffer and water-bath sonicated 4 times (20 sec each). Cells were centrifuged at 16800 g for 30 min at 4 °C. 300 µL NMR samples at 3.7 mg/mL of total protein in the soluble cell lysates (as determined by Bradford assays), 5 µM ^{15}N isotope-labeled αSyn, 333 µM ATP, 1 mM DTT, 3 mM $MgSO_4$, 1 x protease inhibitor, 10 % D_2O were prepared. Phosphorylation was followed by time-resolved NMR experiments for 12 h.

4.2.13 *In-cell* NMR sample preparation

1-1.5 mM stock solutions of recombinantly expressed and purified ^{15}N isotope-labeled α-, β- and γSyn were diluted to 400 µM concentrations in electroporation buffer at pH 7.2.

40-60 million cells were harvested at 80 % confluence, and electroporated as described (see *Protein delivery by electroporation*). Recovered and PBS washed cells were pelleted by centrifugation at 200 g for 6 min at 25 °C and the cell pellets were re-suspended in Leibovitz's L-15 medium supplemented with 10 % FBS and 10 % D_2O. Typically 200-300 µL of fresh media were added to 15-30 million recovered cells. Cell suspensions were transferred into 3, 4 or 5 mm diameter Shigemi tubes. Cells were carefully packed by spinning the NMR tubes with a hand-cranked centrifuge. The heights of the cell slurries within the NMR tubes were measured and back calculated into specific volumes.

4.2.14 NMR experiments

***In-cell* NMR and *in-cell* NMR lysate measurements of ^{15}N isotope-labeled αSyn:** Experiments were recorded on a 750 MHz Bruker Avance spectrometer equipped with a cryogenically cooled triple resonance ^{1}H {^{13}C/^{15}N}TCI probe, at 10 °C. Depending on the volume of the samples, Shigemi tubes of either 3 mm, 4 mm or 5 mm diameters were used. All *in-cell* NMR experiments were performed on at least two independent samples. SOFAST-HMQC pulse sequences[338] were used in every NMR experiment except for ^{15}N-relaxation measurements.

1D and 2D ^{1}H-^{15}N SOFAST-HMQC experiments were recorded with interscan delays of 30 ms, a proton 120° polychromatic PC9 pulse of 2400 µs and a REBURP 180° pulse of 1600 µs[338]. ^{15}N-decoupling during the acquisition period was achieved with the Waltz-16 sequence at 1.25 kHz[339]. 1D ^{1}H-^{15}N SOFAST-HMQC spectra were recorded with 4096 scans and 1024 complex points for a sweep width of 16.6 p.p.m. 2D NMR spectra were recorded with either 512, 1024 or 2048 scans, 1024 complex points for a sweep width of 16.6 p.p.m for the ^{1}H dimension (zero-filling to 4096 points), and 128 complex points for the ^{15}N dimension and a sweep width of 26 p.p.m (zero-filling to 1024 points).

^{15}N-relaxation experiments were acquired with pulse sequences based on those described by Farrow *et al.*[258]. *In vitro* reference values were measured with AcαSyn at 50 µM concentration, dissolved in a buffered aqueous solution containing 20 mM Sodium Phosphate, 150 mM NaCl, at pH =7.0 supplemented with 10 % D_2O.

In-cell NMR spectra used for longitudinal relaxation R_1 analyses were collected using the following relaxation delays (in ms): 10, 50, 100, 200, 300, 400, 500, 1000, and 2000. Duplicate spectra were collected for experiments with 10 ms relaxation delays. Transversal relaxation was measured using a pulse sequence applying the Carr-Purcell-Meiboom-Gill pulse sequence (CPMG) pulse train with the following relaxation delays (in ms): 20, 40, 60, 100, 160, 200, 300, 380, 480. Residue-resolved *in-cell* R_2 rates were obtained using the following delays (in ms): 20, 50, 80, 120, 200. Duplicate spectra were collected for the CPMG experiments with 20 ms relaxation delays. $R_1\rho$ data were measured as previously described[340] using a spin-lock field strength of 10000 Hz with the following relaxation delays (in ms): 20, 50, 60, 120, 160, 200, 300, 380, 480. Duplicate spectra were collected for the $R_1\rho$ experiments with 20 ms

relaxation delays. 1D amide envelope spectra for measuring R_1, R_2 and $R_1\rho$ were acquired with 256 scans and 1024 complex points for a sweep width of 16.6 p.p.m for the ^{1}H dimension (zero-filling to 4096 points). 2D CMPG-HSQC experiments were recorded with 128 scans, 1024 complex points for a sweep width of 16.6 ppm for the ^{1}H dimension (zero-filling to 4096 points), and 128 complex points for the ^{15}N dimension (t1) for a sweep width of 26 p.p.m (zero-filling to 1024 points). The delays between the 180° pulses in the CPMG pulse train were 1 ms. R_1, R_2 and $R_1\rho$ rates were obtained by extracting resonance cross peak heights and plotting them as a function of the relaxation delays. Fitting to single exponential decays using the Prism software package was performed.

1D and 2D ^{15}N-edited NMR spectra were obtained from experimental data processed with Topspin 3.1 (Bruker), apodized by a cosine bell window function in both dimensions and displayed in iNMR 3.6.3. 2D NMR spectral analyses were performed in Sparky[341]. Peak intensities were taken at maximum peak heights in each NMR spectrum. Uncertainties in NMR peak intensities were evaluated using the individual signal to noise ratios (SNR). R_1, R_2 ^{15}N-relaxation rates were obtained by fitting time-dependent changes in signal intensities of each peak *i* by a simple exponential equation $I^i(t) = I_0^i \exp\left(-R^i t\right)$, where *t* is the ^{15}N-relaxation delay. These relaxation rates were measured 2 or 3 times, the standard errors between independent experiments are shown in the respective relaxation rate plots.

Reference NMR spectra for comparison and analysis of *in-cell* data were acquired with 5 μM of αSyn, βSyn, γSyn and AcαSyn samples dissolved in buffered aqueous solution containing 20 mM Sodium Phosphate, 150 mM NaCl, at pH=7.0, supplemented with 10 % D_2O. In all cases, NMR spectra were recorded matching the conditions and parameters to those used for each cell-line, i.e. same tube diameter, number of scans, increments in indirect dimensions.

Assessing effective NMR concentrations of αSyn: αSyn concentrations in *in-cell* NMR samples were determined by integration of 1D ^{1}H-^{15}N SOFAST-HMQC amide envelope spectra for each cell line and by comparison with reference αSyn samples at 5 μM in a buffered aqueous solutions containing 20 mM Potassium Phosphate, 150 mM NaCl, at pH=7.

Background NMR signals in HeLa, RCSN3 and B65 cells and extracts: 40-60 million cells were harvested at 80 % confluence and electroporated in the absence of protein (mock treatement). Sample preparation was performed as described earlier (*see In-cell NMR sample preparation*).
In-cell NMR measurements were carried out in 4 mm diameter Shigemi tubes at 10 °C, without repetitions. Spectra were required with 4096 scans, 128 complex points for the ^{15}N dimension and a sweep width of 26 p.p.m (zero-filling to 1024 points).

αSyn phosphorylation in extracts of PKL3 over-expressing HeLa cells: PLK3 transfection and lysate preparations were performed as described above (see *αSyn phosphorylation in PLK3 over-expressing cells)*. Each spectrum was recorded at 37 °C with 519 scans, and 64 complex points for the ^{15}N dimension and a sweep width of 26 p.p.m (zero-filling to 1024 points).

4.2.15 Quality control experiments for *in-cell* NMR samples

Supernatant measurements: After each *in-cell* NMR measurement, packed cells were gently brought back into suspension with the excess liquid that was present in the NMR tube and transferred into a 1.5 mL Eppendorf tube. After 5 minutes of centrifugation at 200 g, the supernatant was collected and transferred back into the same NMR tube for additional leakage measurements, using the same acquisition settings as for the *in-cell* sample.

Trypan Blue staining: After each *in-cell* NMR experiment, 5-10 µL of the centrifuged cell pellet was removed for Trypan Blue staining. Cell dilutions were adjusted to a total cell count of 100-200 cells on the hemocytometer grid. Equal volumes (5-10 µL) of 0.4% Trypan blue staining solutions were added to the pellet and thoroughly mixed.
10-20 µL of the cell suspensions were dispensed onto the counting chamber and covered with a cover slip. The numbers of viable (non-blue) and non-viable (blue) cells were counted within 5 minutes of staining on a phase-contrast microscope.

αSyn protein integrity under *in-cell* NMR conditions: To test whether αSyn was degraded inside cells during the NMR measurements, multiple electroporation samples

were prepared from 18 million HeLa cells, each electroporated with 400 µM of αSyn. Cells were recovered for 5 h on 14 cm diameter plates, washed 3 times with PBS and harvested by 0.25 % Trypsin/EDTA treatment fir 5 min, at 37 °C. Trypsin was neutralized with cell-line specific complete medium and cells were pelleted by centrifugation at 200 g fir 6 min at 25 °C. 8 million recovered cells were counted and re-suspended in 200 µL of Leibovitz's L-15 solution supplemented with 10 % FBS and 10 % D_2O. This cell suspension was aliquoted into four 1,5 mL Eppendorf tubes (2 million cells per 50 µL of solution) and kept at 10 °C. At 4 different time-points, t=0, 3, 9, 20 h, one sample was centrifuged (~100 g, 5 min) and the supernatant was discarded (~40 µL). Lysates were prepared with RIPA buffer, as outlined earlier. Lysates were clarified by centrifugation at 16800 g for 30 min at 4 °C and soluble fractions were recovered (~50-60 µL). Protein concentrations were measured by Bradford assays (4.5-5 mg/mL). To evaluate αSyn leakage, 4 µL of this supernatant, and 20 µg of the soluble cell lysate were loaded on SDS-PAGE and analyzed by Western blotting.

αSyn protein integrity in the *in-cell* NMR samples: Lysates prepared from *in-cell* NMR samples (see *In-cell NMR lysate preparation*) were flash frozen after NMR measurements and stored at -20 °C. On average 15-20 µL of these lysates were separated by SDS-PAGE and analyzed by Western blotting, as described earlier.

References

1. Miklos, A. C., Li, C., Sharaf, N. G. & Pielak, G. J. Volume exclusion and soft interaction effects on protein stability under crowded conditions. Biochemistry 49, 6984-91 (2011).
2. Dix, J. A. & Verkman, A. S. Crowding effects on diffusion in solutions and cells. Annu Rev Biophys 37, 247-63 (2008).
3. Chen, C., Loe, F., Blocki, A., Peng, Y. & Raghunath, M. Applying macromolecular crowding to enhance extracellular matrix deposition and its remodeling in vitro for tissue engineering and cell-based therapies. Adv Drug Deliv Rev 63, 277-90 (2011).
4. Maldonado, A. Y., Burz, D. S. & Shekhtman, A. In-cell NMR spectroscopy. Prog Nucl Magn Reson Spectrosc 59, 197-212 (2011).
5. Crowley, P. B., Chow, E. & Papkovskaia, T. Protein interactions in the Escherichia coli cytosol: an impediment to in-cell NMR spectroscopy. Chembiochem 12, 1043-8 (2011).
6. Binolfi, A., Theillet, F. X. & Selenko, P. Bacterial in-cell NMR of human alpha-synuclein: a disordered monomer by nature? Biochem Soc Trans 40, 950-4 (2012).
7. Banci, L., Barbieri, L., Bertini, I., Cantini, F. & Luchinat, E. In-cell NMR in E. coli to monitor maturation steps of hSOD1. PLoS One 6, e23561 (2011).
8. Hamatsu, J. et al. High-resolution heteronuclear multidimensional NMR of proteins in living insect cells using a baculovirus protein expression system. J Am Chem Soc 135, 1688-91 (2013).
9. Bodart, J. F. et al. NMR observation of Tau in Xenopus oocytes. J Magn Reson 192, 252-7 (2008).
10. Bertrand, K., Reverdatto, S., Burz, D. S., Zitomer, R. & Shekhtman, A. Structure of Proteins in Eukaryotic Compartments. Journal of the American Chemical Society 134, 12798-12806 (2012).
11. Inomata, K. et al. High-resolution multi-dimensional NMR spectroscopy of proteins in human cells. Nature 458, 106-9 (2009).
12. Ogino, S. et al. Observation of NMR signals from proteins introduced into living mammalian cells by reversible membrane permeabilization using a pore-forming toxin, streptolysin O. J Am Chem Soc 131, 10834-5 (2009).
13. Kubo, S. et al. A gel-encapsulated bioreactor system for NMR studies of protein-protein interactions in living Mammalian cells. Angew Chem Int Ed Engl 52, 1208-11 (2012).
14. Lashuel, H. A., Overk, C. R., Oueslati, A. & Masliah, E. The many faces of alpha-synuclein: from structure and toxicity to therapeutic target. Nat Rev Neurosci 14, 38-48 (2013).
15. Puschmann, A., Bhidayasiri, R. & Weiner, W. J. Synucleinopathies from bench to bedside. Parkinsonism Relat Disord 18 Suppl 1, S24-7 (2012).
16. Beyer, K. & Ariza, A. Protein aggregation mechanisms in synucleinopathies: commonalities and differences. J Neuropathol Exp Neurol 66, 965-74 (2007).

17. Breydo, L., Wu, J. W. & Uversky, V. N. Alpha-synuclein misfolding and Parkinson's disease. Biochim Biophys Acta 1822, 261-85 (2012).
18. Pfefferkorn, C. M., Jiang, Z. & Lee, J. C. Biophysics of alpha-synuclein membrane interactions. Biochim Biophys Acta 1818, 162-71 (2011).
19. Beyer, K. & Ariza, A. Alpha-Synuclein Posttranslational Modification and Alternative Splicing as a Trigger for Neurodegeneration. Mol Neurobiol (2012).
20. Fahn, S. Parkinson's disease: 10 years of progress, 1997-2007. Mov Disord 25 Suppl 1, S2-14 (2009).
21. Paris, I. et al. The catecholaminergic RCSN-3 cell line: a model to study dopamine metabolism. Neurotox Res 13, 221-30 (2008).
22. Goedert, M. Alpha-synuclein and neurodegenerative diseases. Nat Rev Neurosci 2, 492-501 (2001).
23. Hoyer, W. et al. Dependence of alpha-synuclein aggregate morphology on solution conditions. J Mol Biol 322, 383-93 (2002).
24. Fauvet, B. et al. Characterization of Semisynthetic and Naturally Nalpha-Acetylated alpha-Synuclein in Vitro and in Intact Cells: IMPLICATIONS FOR AGGREGATION AND CELLULAR PROPERTIES OF alpha-SYNUCLEIN. J Biol Chem 287, 28243-62 (2012).
25. Mbefo, M. K. et al. Phosphorylation of synucleins by members of the Polo-like kinase family. J Biol Chem 285, 2807-22 (2010).
26. Negro, A., Brunati, A. M., Donella-Deana, A., Massimino, M. L. & Pinna, L. A. Multiple phosphorylation of alpha-synuclein by protein tyrosine kinase Syk prevents eosin-induced aggregation. Faseb J 16, 210-2 (2002).
27. Cannon, J. R. & Greenamyre, J. T. Neurotoxic in vivo models of Parkinson's disease recent advances. Prog Brain Res 184, 17-33 (2010).
28. Jethva, P. N., Kardani, J. R. & Roy, I. Modulation of alpha-synuclein aggregation by dopamine in the presence of MPTP and its metabolite. Febs J 278, 1688-98 (2011).
29. Radad, K., Rausch, W. D. & Gille, G. Rotenone induces cell death in primary dopaminergic culture by increasing ROS production and inhibiting mitochondrial respiration. Neurochem Int 49, 379-86 (2006).
30. Ito, Y. & Selenko, P. Cellular structural biology. Curr Opin Struct Biol 20, 640-8 (2010).
31. Selenko, P. & Wagner, G. NMR mapping of protein interactions in living cells. Nat Methods 3, 80-1 (2006).
32. Selenko, P. & Wagner, G. Looking into live cells with in-cell NMR spectroscopy. J Struct Biol 158, 244-53 (2007).
33. Serber, Z., Corsini, L., Durst, F. & Dotsch, V. In-cell NMR spectroscopy. Methods Enzymol 394, 17-41 (2005).
34. Cai, M. et al. An efficient and cost-effective isotope labeling protocol for proteins expressed in Escherichia coli. J Biomol NMR 11, 97-102 (1998).
35. Theillet, F. X. et al. Cell signaling, post-translational protein modifications and NMR spectroscopy. J Biomol NMR (2012).
36. Theillet, F. X. et al. Site-specific mapping and time-resolved monitoring of lysine methylation by high-resolution NMR spectroscopy. J Am Chem Soc 134, 7616-9 (2012).

37. Liokatis, S. et al. Phosphorylation of histone H3 Ser10 establishes a hierarchy for subsequent intramolecular modification events. Nat Struct Mol Biol 19, 819-23 (2012).
38. Liokatis, S., Dose, A., Schwarzer, D. & Selenko, P. Simultaneous detection of protein phosphorylation and acetylation by high-resolution NMR spectroscopy. J Am Chem Soc 132, 14704-5 (2010).
39. Ellis, R. J. Macromolecular crowding: an important but neglected aspect of the intracellular environment. Curr Opin Struct Biol 11, 114-9 (2001).
40. Bernado, P., Garcia de la Torre, J. & Pons, M. Macromolecular crowding in biological systems: hydrodynamics and NMR methods. J Mol Recognit 17, 397-407 (2004).
41. Waudby, C. A. et al. Rapid distinction of intracellular and extracellular proteins using NMR diffusion measurements. J Am Chem Soc 134, 11312-5 (2012).
42. Barnes, C. O. & Pielak, G. J. In-cell protein NMR and protein leakage. Proteins 79, 347-51 (2011).
43. Selenko, P., Serber, Z., Gadea, B., Ruderman, J. & Wagner, G. Quantitative NMR analysis of the protein G B1 domain in Xenopus laevis egg extracts and intact oocytes. Proc Natl Acad Sci U S A 103, 11904-9 (2006).
44. Serber, Z. et al. Investigating macromolecules inside cultured and injected cells by in-cell NMR spectroscopy. Nat Protoc 1, 2701-9 (2006).
45. Milletti, F. Cell-penetrating peptides: classes, origin, and current landscape. Drug Discov Today 17, 850-60 (2012).
46. Gautam, A. et al. CPPsite: a curated database of cell penetrating peptides. Database (Oxford) 2012, bas015 (2012).
47. Hitsuda, T. et al. A protein transduction method using oligo-arginine (3R) for the delivery of transcription factors into cell nuclei. Biomaterials 33, 4665-72 (2012).
48. Fotin-Mleczek, M. et al. Cationic cell-penetrating peptides interfere with TNF signalling by induction of TNF receptor internalization. J Cell Sci 118, 3339-51 (2005).
49. Albani, D. et al. Protective effect of TAT-delivered alpha-synuclein: relevance of the C-terminal domain and involvement of HSP70. Faseb J 18, 1713-5 (2004).
50. Fujimoto, K. et al. Inhibition of pRb phosphorylation and cell cycle progression by an antennapedia-p16(INK4A) fusion peptide in pancreatic cancer cells. Cancer Lett 159, 151-8 (2000).
51. Saalik, P. et al. Protein cargo delivery properties of cell-penetrating peptides. A comparative study. Bioconjug Chem 15, 1246-53 (2004).
52. Zender, L., Kuhnel, F., Kock, R., Manns, M. & Kubicka, S. VP22-mediated intercellular transport of p53 in hepatoma cells in vitro and in vivo. Cancer Gene Ther 9, 489-96 (2002).
53. Zahid, M. & Robbins, P. D. Protein Transduction Domains: Applications for Molecular Medicine. Curr Gene Ther (2012).
54. Lehto, T., Kurrikoff, K. & Langel, U. Cell-penetrating peptides for the delivery of nucleic acids. Expert Opin Drug Deliv 9, 823-36 (2012).
55. Dietz, G. P. Cell-penetrating peptide technology to deliver chaperones and associated factors in diseases and basic research. Curr Pharm Biotechnol 11, 167-74 (2010).

56. Waxman, E. A. & Giasson, B. I. Characterization of kinases involved in the phosphorylation of aggregated alpha-synuclein. J Neurosci Res 89, 231-47 (2011).
57. Madani, F., Lindberg, S., Langel, U., Futaki, S. & Graslund, A. Mechanisms of cellular uptake of cell-penetrating peptides. J Biophys, 414729 (2011).
58. Ma, D. X., Shi, N. Q. & Qi, X. R. Distinct transduction modes of arginine-rich cell-penetrating peptides for cargo delivery into tumor cells. Int J Pharm 419, 200-8 (2011).
59. Kerkis, A., Hayashi, M. A., Yamane, T. & Kerkis, I. Properties of cell penetrating peptides (CPPs). IUBMB Life 58, 7-13 (2006).
60. Kaplan, I. M., Wadia, J. S. & Dowdy, S. F. Cationic TAT peptide transduction domain enters cells by macropinocytosis. J Control Release 102, 247-53 (2005).
61. Fittipaldi, A. et al. Cell membrane lipid rafts mediate caveolar endocytosis of HIV-1 Tat fusion proteins. J Biol Chem 278, 34141-9 (2003).
62. Palm-Apergi, C., Lonn, P. & Dowdy, S. F. Do cell-penetrating peptides actually "penetrate" cellular membranes? Mol Ther 20, 695-7 (2012).
63. Sauder, R., Seelig, J. & Ziegler, A. Thermodynamics of lipid interactions with cell-penetrating peptides. Methods Mol Biol 683, 129-55 (2011).
64. Foerg, C. & Merkle, H. P. On the biomedical promise of cell penetrating peptides: limits versus prospects. J Pharm Sci 97, 144-62 (2008).
65. Duchardt, F., Fotin-Mleczek, M., Schwarz, H., Fischer, R. & Brock, R. A comprehensive model for the cellular uptake of cationic cell-penetrating peptides. Traffic 8, 848-66 (2007).
66. Fischer, R., Kohler, K., Fotin-Mleczek, M. & Brock, R. A stepwise dissection of the intracellular fate of cationic cell-penetrating peptides. J Biol Chem 279, 12625-35 (2004).
67. Console, S., Marty, C., Garcia-Echeverria, C., Schwendener, R. & Ballmer-Hofer, K. Antennapedia and HIV transactivator of transcription (TAT) "protein transduction domains" promote endocytosis of high molecular weight cargo upon binding to cell surface glycosaminoglycans. J Biol Chem 278, 35109-14 (2003).
68. Bode, S. A. et al. Self-assembling mini cell-penetrating peptides enter by both direct translocation and glycosaminoglycan-dependent endocytosis. Chem Commun (Camb) 48, 7179-81 (2012).
69. Al Soraj, M. et al. siRNA and pharmacological inhibition of endocytic pathways to characterize the differential role of macropinocytosis and the actin cytoskeleton on cellular uptake of dextran and cationic cell penetrating peptides octaarginine (R8) and HIV-Tat. J Control Release 161, 132-41 (2012).
70. Richard, J. P. et al. Cell-penetrating peptides. A reevaluation of the mechanism of cellular uptake. J Biol Chem 278, 585-90 (2003).
71. Takeuchi, T. et al. Direct and rapid cytosolic delivery using cell-penetrating peptides mediated by pyrenebutyrate. ACS Chem Biol 1, 299-303 (2006).
72. Fuchs, S., Otto, H., Jehle, S., Henklein, P. & Schluter, A. D. Fluorescent dendrimers with a peptide cathepsin B cleavage site for drug delivery applications. Chem Commun (Camb), 1830-2 (2005).
73. Zhang, Y. et al. Role of furin in delivery of a CTL epitope of an anthrax toxin-fusion protein. Microbiol Immunol 45, 119-25 (2001).

74. Ogris, M., Carlisle, R. C., Bettinger, T. & Seymour, L. W. Melittin enables efficient vesicular escape and enhanced nuclear access of nonviral gene delivery vectors. J Biol Chem 276, 47550-5 (2001).
75. Wadia, J. S., Stan, R. V. & Dowdy, S. F. Transducible TAT-HA fusogenic peptide enhances escape of TAT-fusion proteins after lipid raft macropinocytosis. Nat Med 10, 310-5 (2004).
76. Kakimoto, S., Tanabe, T., Azuma, H. & Nagasaki, T. Enhanced internalization and endosomal escape of dual-functionalized poly(ethyleneimine)s polyplex with diphtheria toxin T and R domains. Biomed Pharmacother 64, 296-301 (2010).
77. Shiraishi, T., Pankratova, S. & Nielsen, P. E. Calcium ions effectively enhance the effect of antisense peptide nucleic acids conjugated to cationic tat and oligoarginine peptides. Chem Biol 12, 923-9 (2005).
78. Bekei, B. et al. In-cell NMR in mammalian cells: part 1. Methods Mol Biol 895, 43-54 (2012).
79. Ruzza, P., Biondi, B., Marchiani, A., Antolini, N. & Calderan, A. Cell-Penetrating Peptides: A Comparative study on Lipid Affinity and Cargo Delivery properties. Pharmaceuticals 3, 1045-1062 (2010).
80. Esbjorner, E. K., Lincoln, P. & Norden, B. Counterion-mediated membrane penetration: cationic cell-penetrating peptides overcome Born energy barrier by ion-pairing with phospholipids. Biochim Biophys Acta 1768, 1550-8 (2007).
81. Amand, H. L. et al. Cell surface binding and uptake of arginine- and lysine-rich penetratin peptides in absence and presence of proteoglycans. Biochim Biophys Acta 1818, 2669-78 (2012).
82. Alouf, J. E. Pore-forming bacterial protein toxins: an overview. Curr Top Microbiol Immunol 257, 1-14 (2001).
83. Parker, M. W. & Feil, S. C. Pore-forming protein toxins: from structure to function. Prog Biophys Mol Biol 88, 91-142 (2005).
84. Ichiki, Y., Kawachi, T., Miyashita, M., Nakagawa, Y. & Miyagawa, H. Isolation and characterization of a novel non-selective beta-toxin from the venom of the scorpion Isometrus maculatus. Biosci Biotechnol Biochem 76, 2089-92 (2012).
85. Wu, W. G., Tjong, S. C., Wu, P. L., Kuo, J. H. & Wu, K. Role of heparan sulfates and glycosphingolipids in the pore formation of basic polypeptides of cobra cardiotoxin. Adv Exp Med Biol 677, 143-9 (2010).
86. Iwamoto, M., Shimizu, H., Muramatsu, I. & Oiki, S. A cytotoxic peptide from a marine sponge exhibits ion channel activity through vectorial-insertion into the membrane. FEBS Lett 584, 3995-9 (2010).
87. Thompson, J. R., Cronin, B., Bayley, H. & Wallace, M. I. Rapid assembly of a multimeric membrane protein pore. Biophys J 101, 2679-83 (2011).
88. Gonzalez, M. R., Bischofberger, M., Pernot, L., van der Goot, F. G. & Freche, B. Bacterial pore-forming toxins: the (w)hole story? Cell Mol Life Sci 65, 493-507 (2008).
89. Feil, S. C., Polekhina, G., Gorman, M. A. & Parker, M. W. Proteins: membrane binding and pore formation. Introduction. Adv Exp Med Biol 677, 1-13 (2010).
90. Iacovache, I., Bischofberger, M. & van der Goot, F. G. Structure and assembly of pore-forming proteins. Curr Opin Struct Biol 20, 241-6 (2010).

91. Shatursky, O. et al. The mechanism of membrane insertion for a cholesterol-dependent cytolysin: a novel paradigm for pore-forming toxins. Cell 99, 293-9 (1999).
92. Iacovache, I. et al. A rivet model for channel formation by aerolysin-like pore-forming toxins. Embo J 25, 457-66 (2006).
93. Tweten, R. K. Cholesterol-dependent cytolysins, a family of versatile pore-forming toxins. Infect Immun 73, 6199-209 (2005).
94. Heuck, A. P., Tweten, R. K. & Johnson, A. E. Beta-barrel pore-forming toxins: intriguing dimorphic proteins. Biochemistry 40, 9065-73 (2001).
95. Geny, B. & Popoff, M. R. Bacterial protein toxins and lipids: pore formation or toxin entry into cells. Biol Cell 98, 667-78 (2006).
96. Bhakdi, S. & Tranum-Jensen, J. Damage to mammalian cells by proteins that form transmembrane pores. Rev Physiol Biochem Pharmacol 107, 147-223 (1987).
97. Giddings, K. S., Johnson, A. E. & Tweten, R. K. Redefining cholesterol's role in the mechanism of the cholesterol-dependent cytolysins. Proc Natl Acad Sci U S A 100, 11315-20 (2003).
98. Idone, V. et al. Repair of injured plasma membrane by rapid Ca2+-dependent endocytosis. J Cell Biol 180, 905-14 (2008).
99. McNeil, P. L. & Kirchhausen, T. An emergency response team for membrane repair. Nat Rev Mol Cell Biol 6, 499-505 (2005).
100. Bhakdi, S. & Tranum-Jensen, J. Membrane damage by pore-forming bacterial cytolysins. Microb Pathog 1, 5-14 (1986).
101. Bekei, B., Rose, H. M., Herzig, M. & Selenko, P. In-cell NMR in mammalian cells: part 2. Methods Mol Biol 895, 55-66 (2012).
102. Gonzalez, M. R. et al. Pore-forming toxins induce multiple cellular responses promoting survival. Cell Microbiol 13, 1026-43 (2011).
103. Huffman, D. L. et al. Mitogen-activated protein kinase pathways defend against bacterial pore-forming toxins. Proc Natl Acad Sci U S A 101, 10995-1000 (2004).
104. Ratner, A. J. et al. Epithelial cells are sensitive detectors of bacterial pore-forming toxins. J Biol Chem 281, 12994-8 (2006).
105. Gurcel, L., Abrami, L., Girardin, S., Tschopp, J. & van der Goot, F. G. Caspase-1 activation of lipid metabolic pathways in response to bacterial pore-forming toxins promotes cell survival. Cell 126, 1135-45 (2006).
106. Hamon, M. A. et al. Histone modifications induced by a family of bacterial toxins. Proc Natl Acad Sci U S A 104, 13467-72 (2007).
107. Andre, F. & Mir, L. M. DNA electrotransfer: its principles and an updated review of its therapeutic applications. Gene Ther 11 Suppl 1, S33-42 (2004).
108. Neumann, E., Schaefer-Ridder, M., Wang, Y. & Hofschneider, P. H. Gene transfer into mouse lyoma cells by electroporation in high electric fields. Embo J 1, 841-5 (1982).
109. Baron, S., Poast, J., Rizzo, D., McFarland, E. & Kieff, E. Electroporation of antibodies, DNA, and other macromolecules into cells: a highly efficient method. J Immunol Methods 242, 115-26 (2000).
110. Berglund, D. L. & Starkey, J. R. Introduction of antibody into viable cells using electroporation. Cytometry 12, 64-7 (1991).
111. Inoue, A. et al. Electro-transfer of small interfering RNA ameliorated arthritis in rats. Biochem Biophys Res Commun 336, 903-8 (2005).

112. Rui, M., Chen, Y., Zhang, Y. & Ma, D. Transfer of anti-TFAR19 monoclonal antibody into HeLa cells by in situ electroporation can inhibit the apoptosis. Life Sci 71, 1771-8 (2002).
113. Zeitelhofer, M., Vessey, J. P., Thomas, S., Kiebler, M. & Dahm, R. Transfection of cultured primary neurons via nucleofection. Curr Protoc Neurosci Chapter 4, Unit4 32 (2009).
114. Viesselmann, C., Ballweg, J., Lumbard, D. & Dent, E. W. Nucleofection and primary culture of embryonic mouse hippocampal and cortical neurons. J Vis Exp (2011).
115. Teissie, J., Golzio, M. & Rols, M. P. Mechanisms of cell membrane electropermeabilization: a minireview of our present (lack of ?) knowledge. Biochim Biophys Acta 1724, 270-80 (2005).
116. Veech, R. L., Kashiwaya, Y. & King, M. T. The resting membrane potential of cells are measures of electrical work, not of ionic currents. Integr Physiol Behav Sci 30, 283-307 (1995).
117. Valic, B. et al. Effect of electric field induced transmembrane potential on spheroidal cells: theory and experiment. Eur Biophys J 32, 519-28 (2003).
118. Hibino, M., Itoh, H. & Kinosita, K., Jr. Time courses of cell electroporation as revealed by submicrosecond imaging of transmembrane potential. Biophys J 64, 1789-800 (1993).
119. Gross, D., Loew, L. M., Ryan, T. A. & Webb, W. W. Spatially-resolved optical imaging of membrane potentials induced by applied electric fields. Prog Clin Biol Res 210, 263-70 (1986).
120. Rols, M. P. Electropermeabilization, a physical method for the delivery of therapeutic molecules into cells. Biochim Biophys Acta 1758, 423-8 (2006).
121. Kotnik, T. & Miklavcic, D. Analytical description of transmembrane voltage induced by electric fields on spheroidal cells. Biophys J 79, 670-9 (2000).
122. Teissie, J. & Rols, M. P. An experimental evaluation of the critical potential difference inducing cell membrane electropermeabilization. Biophys J 65, 409-13 (1993).
123. Rols, M. P. & Teissie, J. Electropermeabilization of mammalian cells. Quantitative analysis of the phenomenon. Biophys J 58, 1089-98 (1990).
124. Escoffre, J. M., Dean, D. S., Hubert, M., Rols, M. P. & Favard, C. Membrane perturbation by an external electric field: a mechanism to permit molecular uptake. Eur Biophys J 36, 973-83 (2007).
125. Bockmann, R. A., de Groot, B. L., Kakorin, S., Neumann, E. & Grubmuller, H. Kinetics, statistics, and energetics of lipid membrane electroporation studied by molecular dynamics simulations. Biophys J 95, 1837-50 (2008).
126. Tarek, M. Membrane electroporation: a molecular dynamics simulation. Biophys J 88, 4045-53 (2005).
127. Wang, M., Orwar, O., Olofsson, J. & Weber, S. G. Single-cell electroporation. Anal Bioanal Chem 397, 3235-48 (2010).
128. Chang, D. C. & Reese, T. S. Changes in membrane structure induced by electroporation as revealed by rapid-freezing electron microscopy. Biophys J 58, 1-12 (1990).
129. Gabriel, B. & Teissie, J. Time courses of mammalian cell electropermeabilization observed by millisecond imaging of membrane property changes during the pulse. Biophys J 76, 2158-65 (1999).

130. Klenchin, V. A., Sukharev, S. I., Serov, S. M., Chernomordik, L. V. & Chizmadzhev Yu, A. Electrically induced DNA uptake by cells is a fast process involving DNA electrophoresis. Biophys J 60, 804-11 (1991).
131. Golzio, M., Teissie, J. & Rols, M. P. Direct visualization at the single-cell level of electrically mediated gene delivery. Proc Natl Acad Sci U S A 99, 1292-7 (2002).
132. Rosazza, C., Escoffre, J. M., Zumbusch, A. & Rols, M. P. The actin cytoskeleton has an active role in the electrotransfer of plasmid DNA in mammalian cells. Mol Ther 19, 913-21 (2011).
133. Rosazza, C. et al. Cholesterol implications in plasmid DNA electrotransfer: Evidence for the involvement of endocytotic pathways. Int J Pharm 423, 134-43 (2012).
134. Mo, D. et al. Nucleofection disrupts tight junction fence function to alter membrane polarity of renal epithelial cells. Am J Physiol Renal Physiol 299, F1178-84 (2010).
135. Kanthou, C. et al. The endothelial cytoskeleton as a target of electroporation-based therapies. Mol Cancer Ther 5, 3145-52 (2006).
136. Mello de Queiroz, F., Sanchez, A., Agarwal, J. R., Stuhmer, W. & Pardo, L. A. Nucleofection induces non-specific changes in the metabolic activity of transfected cells. Mol Biol Rep 39, 2187-94 (2012).
137. Anderson, B. R., Kariko, K. & Weissman, D. Nucleofection induces transient eIF2alpha phosphorylation by GCN2 and PERK. Gene Ther (2012).
138. Korzhnev, D., Billeter, M., Arseniev, A. S. & Orekhov, V. Y. NMR studies of Brownian tumbling and internal motions in proteins. Progress in Nuclear Magnetic Resonance Spectroscopy 38 197 ± 266 (2001).
139. Li, C. et al. Differential dynamical effects of macromolecular crowding on an intrinsically disordered protein and a globular protein: implications for in-cell NMR spectroscopy. J Am Chem Soc 130, 6310-1 (2008).
140. Sibille, N. & Bernado, P. Structural characterization of intrinsically disordered proteins by the combined use of NMR and SAXS. Biochem Soc Trans 40, 955-62 (2012).
141. Felli, I. C. & Pierattelli, R. Recent progress in NMR spectroscopy: toward the study of intrinsically disordered proteins of increasing size and complexity. IUBMB Life 64, 473-81 (2012).
142. Ding, K., Louis, J. M. & Gronenborn, A. M. Insights into conformation and dynamics of protein GB1 during folding and unfolding by NMR. J Mol Biol 335, 1299-307 (2004).
143. Dunker, A. K. & Obradovic, Z. The protein trinity--linking function and disorder. Nat Biotechnol 19, 805-6 (2001).
144. Tompa, P. Intrinsically disordered proteins: a 10-year recap. Trends Biochem Sci (2012).
145. Ganguly, D. et al. Electrostatically accelerated coupled binding and folding of intrinsically disordered proteins. J Mol Biol 422, 674-84 (2012).
146. Uversky, V. N. Intrinsically disordered proteins from A to Z. Int J Biochem Cell Biol 43, 1090-103 (2011).
147. Tompa, P. The interplay between structure and function in intrinsically unstructured proteins. FEBS Lett 579, 3346-54 (2005).

148. Raychaudhuri, S., Dey, S., Bhattacharyya, N. P. & Mukhopadhyay, D. The role of intrinsically unstructured proteins in neurodegenerative diseases. PLoS One 4, e5566 (2009).
149. Eisenberg, D. & Jucker, M. The amyloid state of proteins in human diseases. Cell 148, 1188-203 (2012).
150. Jellinger, K. A. Recent advances in our understanding of neurodegeneration. J Neural Transm 116, 1111-62 (2009).
151. Perrin, R. J., Woods, W. S., Clayton, D. F. & George, J. M. Interaction of human alpha-Synuclein and Parkinson's disease variants with phospholipids. Structural analysis using site-directed mutagenesis. J Biol Chem 275, 34393-8 (2000).
152. Mucsi, Z., Hudecz, F., Hollosi, M., Tompa, P. & Friedrich, P. Binding-induced folding transitions in calpastatin subdomains A and C. Protein Sci 12, 2327-36 (2003).
153. Ganguly, D., Zhang, W. & Chen, J. Synergistic folding of two intrinsically disordered proteins: searching for conformational selection. Mol Biosyst 8, 198-209 (2012).
154. Chiti, F. & Dobson, C. M. Protein misfolding, functional amyloid, and human disease. Annu Rev Biochem 75, 333-66 (2006).
155. Dedmon, M. M., Patel, C. N., Young, G. B. & Pielak, G. J. FlgM gains structure in living cells. Proc Natl Acad Sci U S A 99, 12681-4 (2002).
156. Krebs, M. R., Morozova-Roche, L. A., Daniel, K., Robinson, C. V. & Dobson, C. M. Observation of sequence specificity in the seeding of protein amyloid fibrils. Protein Sci 13, 1933-8 (2004).
157. Fandrich, M. Oligomeric intermediates in amyloid formation: structure determination and mechanisms of toxicity. J Mol Biol 421, 427-40 (2012).
158. Bocharova, O. V., Breydo, L., Salnikov, V. V., Gill, A. C. & Baskakov, I. V. Synthetic prions generated in vitro are similar to a newly identified subpopulation of PrPSc from sporadic Creutzfeldt-Jakob Disease. Protein Sci 14, 1222-32 (2005).
159. Lavedan, C. et al. Genomic organization and expression of the human beta-synuclein gene (SNCB). Genomics 54, 173-5 (1998).
160. Lavedan, C. et al. Identification, localization and characterization of the human gamma-synuclein gene. Hum Genet 103, 106-12 (1998).
161. Yang, M. L., Hasadsri, L., Woods, W. S. & George, J. M. Dynamic transport and localization of alpha-synuclein in primary hippocampal neurons. Mol Neurodegener 5, 9 (2010).
162. Li, J. Y., Henning Jensen, P. & Dahlstrom, A. Differential localization of alpha-, beta- and gamma-synucleins in the rat CNS. Neuroscience 113, 463-78 (2002).
163. Surguchov, A., Palazzo, R. E. & Surgucheva, I. Gamma synuclein: subcellular localization in neuronal and non-neuronal cells and effect on signal transduction. Cell Motil Cytoskeleton 49, 218-28 (2001).
164. George, J. M. The synucleins. Genome Biol 3, REVIEWS3002 (2002).
165. Lavedan, C. The synuclein family. Genome Res 8, 871-80 (1998).
166. Barbour, R. et al. Red blood cells are the major source of alpha-synuclein in blood. Neurodegener Dis 5, 55-9 (2008).
167. Vivacqua, G. et al. Immunolocalization of alpha-synuclein in the rat spinal cord by two novel monoclonal antibodies. Neuroscience 158, 1478-87 (2009).
168. Specht, C. G. et al. Subcellular localisation of recombinant alpha- and gamma-synuclein. Mol Cell Neurosci 28, 326-34 (2005).

169. Devi, L., Raghavendran, V., Prabhu, B. M., Avadhani, N. G. & Anandatheerthavarada, H. K. Mitochondrial import and accumulation of alpha-synuclein impair complex I in human dopaminergic neuronal cultures and Parkinson disease brain. J Biol Chem 283, 9089-100 (2008).
170. Xie, W. & Chung, K. K. Alpha-synuclein impairs normal dynamics of mitochondria in cell and animal models of Parkinson's disease. J Neurochem (2012).
171. Zhu, M., Li, W. & Lu, C. Role of alpha-synuclein protein levels in mitochondrial morphology and cell survival in cell lines. PLoS One 7, e36377 (2012).
172. Kamp, F. & Beyer, K. Binding of alpha-synuclein affects the lipid packing in bilayers of small vesicles. J Biol Chem 281, 9251-9 (2006).
173. Nemani, V. M. et al. Increased expression of alpha-synuclein reduces neurotransmitter release by inhibiting synaptic vesicle reclustering after endocytosis. Neuron 65, 66-79 (2010).
174. Cheng, F., Vivacqua, G. & Yu, S. The role of alpha-synuclein in neurotransmission and synaptic plasticity. Journal of Chemical Neuroanatomy 42, 242-248 (2011).
175. Burre, J. et al. Alpha-synuclein promotes SNARE-complex assembly in vivo and in vitro. Science 329, 1663-7 (2010).
176. Bonini, N. M. & Giasson, B. I. Snaring the function of alpha-synuclein. Cell 123, 359-61 (2005).
177. Sung, Y. H. & Eliezer, D. Secondary structure and dynamics of micelle bound beta- and gamma-synuclein. Protein Sci 15, 1162-74 (2006).
178. Ducas, V. C. & Rhoades, E. Quantifying Interactions of beta-Synuclein and gamma-Synuclein with Model Membranes. J Mol Biol (2012).
179. Bussell, R., Jr. & Eliezer, D. A structural and functional role for 11-mer repeats in alpha-synuclein and other exchangeable lipid binding proteins. J Mol Biol 329, 763-78 (2003).
180. Chandra, S., Chen, X., Rizo, J., Jahn, R. & Sudhof, T. C. A broken alpha -helix in folded alpha -Synuclein. J Biol Chem 278, 15313-8 (2003).
181. Giasson, B. I., Murray, I. V., Trojanowski, J. Q. & Lee, V. M. A hydrophobic stretch of 12 amino acid residues in the middle of alpha-synuclein is essential for filament assembly. J Biol Chem 276, 2380-6 (2001).
182. Biere, A. L. et al. Parkinson's disease-associated alpha-synuclein is more fibrillogenic than beta- and gamma-synuclein and cannot cross-seed its homologs. J Biol Chem 275, 34574-9 (2000).
183. Hoyer, W., Cherny, D., Subramaniam, V. & Jovin, T. M. Impact of the acidic C-terminal region comprising amino acids 109-140 on alpha-synuclein aggregation in vitro. Biochemistry 43, 16233-42 (2004).
184. Bertoncini, C. W. et al. Release of long-range tertiary interactions potentiates aggregation of natively unstructured alpha-synuclein. Proc Natl Acad Sci U S A 102, 1430-5 (2005).
185. Dedmon, M. M., Lindorff-Larsen, K., Christodoulou, J., Vendruscolo, M. & Dobson, C. M. Mapping long-range interactions in alpha-synuclein using spin-label NMR and ensemble molecular dynamics simulations. J Am Chem Soc 127, 476-7 (2005).
186. Sung, Y. H. & Eliezer, D. Residual structure, backbone dynamics, and interactions within the synuclein family. J Mol Biol 372, 689-707 (2007).

187. Ulmer, T. S., Bax, A., Cole, N. B. & Nussbaum, R. L. Structure and dynamics of micelle-bound human alpha-synuclein. J Biol Chem 280, 9595-603 (2005).
188. Giasson, B. I., Uryu, K., Trojanowski, J. Q. & Lee, V. M. Mutant and wild type human alpha-synucleins assemble into elongated filaments with distinct morphologies in vitro. J Biol Chem 274, 7619-22 (1999).
189. Hashimoto, M. et al. Human recombinant NACP/alpha-synuclein is aggregated and fibrillated in vitro: relevance for Lewy body disease. Brain Res 799, 301-6 (1998).
190. Conway, K. A., Harper, J. D. & Lansbury, P. T. Accelerated in vitro fibril formation by a mutant alpha-synuclein linked to early-onset Parkinson disease. Nat Med 4, 1318-20 (1998).
191. Giehm, L., Lorenzen, N. & Otzen, D. E. Assays for alpha-synuclein aggregation. Methods 53, 295-305 (2011).
192. Waxman, E. A. & Giasson, B. I. A novel, high-efficiency cellular model of fibrillar alpha-synuclein inclusions and the examination of mutations that inhibit amyloid formation. J Neurochem 113, 374-88 (2010).
193. Stefanova, N., Klimaschewski, L., Poewe, W., Wenning, G. K. & Reindl, M. Glial cell death induced by overexpression of alpha-synuclein. J Neurosci Res 65, 432-8 (2001).
194. Hanson, J. C. & Lippa, C. F. Lewy body dementia. Int Rev Neurobiol 84, 215-28 (2009).
195. Jellinger, K. A. Formation and development of Lewy pathology: a critical update. J Neurol 256 Suppl 3, 270-9 (2009).
196. Waxman, E. A. & Giasson, B. I. Molecular mechanisms of alpha-synuclein neurodegeneration. Biochim Biophys Acta 1792, 616-24 (2009).
197. Cremades, N. et al. Direct observation of the interconversion of normal and toxic forms of alpha-synuclein. Cell 149, 1048-59 (2012).
198. Comellas, G., Lemkau, L. R., Zhou, D. H., George, J. M. & Rienstra, C. M. Structural intermediates during alpha-synuclein fibrillogenesis on phospholipid vesicles. J Am Chem Soc 134, 5090-9 (2012).
199. Celej, M. S. et al. Toxic prefibrillar alpha-synuclein amyloid oligomers adopt a distinctive antiparallel beta-sheet structure. Biochem J 443, 719-26 (2012).
200. Reynolds, N. P. et al. Mechanism of membrane interaction and disruption by alpha-synuclein. J Am Chem Soc 133, 19366-75 (2011).
201. Pacheco, C., Aguayo, L. G. & Opazo, C. An extracellular mechanism that can explain the neurotoxic effects of alpha-synuclein aggregates in the brain. Front Physiol 3, 297 (2012).
202. Stockl, M. T., Zijlstra, N. & Subramaniam, V. alpha-Synuclein Oligomers: an Amyloid Pore? : Insights into Mechanisms of alpha-Synuclein Oligomer-Lipid Interactions. Mol Neurobiol (2012).
203. Ferrer, I. Early involvement of the cerebral cortex in Parkinson's disease: convergence of multiple metabolic defects. Prog Neurobiol 88, 89-103 (2009).
204. Uversky, V. N., E, M. C., Bower, K. S., Li, J. & Fink, A. L. Accelerated alpha-synuclein fibrillation in crowded milieu. FEBS Lett 515, 99-103 (2002).
205. Conway, K. A., Rochet, J. C., Bieganski, R. M. & Lansbury, P. T., Jr. Kinetic stabilization of the alpha-synuclein protofibril by a dopamine-alpha-synuclein adduct. Science 294, 1346-9 (2001).

206. Dalfo, E. & Ferrer, I. Early alpha-synuclein lipoxidation in neocortex in Lewy body diseases. Neurobiol Aging 29, 408-17 (2008).
207. Li, J. et al. Neuromelanin enhances the toxicity of alpha-synuclein in SK-N-SH cells. J Neural Transm 119, 685-91 (2012).
208. Nath, S., Goodwin, J., Engelborghs, Y. & Pountney, D. L. Raised calcium promotes alpha-synuclein aggregate formation. Mol Cell Neurosci 46, 516-26 (2011).
209. Bellucci, A. et al. Alpha-synuclein aggregation and cell death triggered by energy deprivation and dopamine overload are counteracted by D2/D3 receptor activation. J Neurochem 106, 560-77 (2008).
210. Wood, S. J. et al. alpha-synuclein fibrillogenesis is nucleation-dependent. Implications for the pathogenesis of Parkinson's disease. J Biol Chem 274, 19509-12 (1999).
211. Nonaka, T., Watanabe, S. T., Iwatsubo, T. & Hasegawa, M. Seeded aggregation and toxicity of {alpha}-synuclein and tau: cellular models of neurodegenerative diseases. J Biol Chem 285, 34885-98 (2010).
212. Luk, K. C. et al. Exogenous alpha-synuclein fibrils seed the formation of Lewy body-like intracellular inclusions in cultured cells. Proc Natl Acad Sci U S A 106, 20051-6 (2009).
213. Lee, H. J. et al. Dopamine promotes formation and secretion of non-fibrillar alpha-synuclein oligomers. Exp Mol Med 43, 216-22 (2011).
214. Danzer, K. M. et al. Exosomal cell-to-cell transmission of alpha synuclein oligomers. Mol Neurodegener 7, 42 (2012).
215. Steiner, J. A., Angot, E. & Brundin, P. A deadly spread: cellular mechanisms of alpha-synuclein transfer. Cell Death Differ 18, 1425-33 (2011).
216. Olanow, C. W. & Prusiner, S. B. Is Parkinson's disease a prion disorder? Proc Natl Acad Sci U S A 106, 12571-2 (2009).
217. Clayton, D. F. & George, J. M. Synucleins in synaptic plasticity and neurodegenerative disorders. J Neurosci Res 58, 120-9 (1999).
218. Uversky, V. N. et al. Biophysical properties of the synucleins and their propensities to fibrillate: inhibition of alpha-synuclein assembly by beta- and gamma-synucleins. J Biol Chem 277, 11970-8 (2002).
219. Hashimoto, M., Rockenstein, E., Mante, M., Mallory, M. & Masliah, E. beta-Synuclein inhibits alpha-synuclein aggregation: a possible role as an anti-parkinsonian factor. Neuron 32, 213-23 (2001).
220. Anderson, J. P. et al. Phosphorylation of Ser-129 is the dominant pathological modification of alpha-synuclein in familial and sporadic Lewy body disease. J Biol Chem 281, 29739-52 (2006).
221. Oueslati, A., Fournier, M. & Lashuel, H. A. Role of post-translational modifications in modulating the structure, function and toxicity of alpha-synuclein: implications for Parkinson's disease pathogenesis and therapies. Prog Brain Res 183, 115-45 (2010).
222. Okochi, M. et al. Constitutive phosphorylation of the Parkinson's disease associated alpha-synuclein. J Biol Chem 275, 390-7 (2000).
223. Fujiwara, H. et al. alpha-Synuclein is phosphorylated in synucleinopathy lesions. Nat Cell Biol 4, 160-4 (2002).
224. Eslamboli, A. et al. Long-term consequences of human alpha-synuclein overexpression in the primate ventral midbrain. Brain 130, 799-815 (2007).

225. Yamada, M., Iwatsubo, T., Mizuno, Y. & Mochizuki, H. Overexpression of alpha-synuclein in rat substantia nigra results in loss of dopaminergic neurons, phosphorylation of alpha-synuclein and activation of caspase-9: resemblance to pathogenetic changes in Parkinson's disease. J Neurochem 91, 451-61 (2004).
226. Paleologou, K. E. et al. Phosphorylation at S87 is enhanced in synucleinopathies, inhibits alpha-synuclein oligomerization, and influences synuclein-membrane interactions. J Neurosci 30, 3184-98 (2010).
227. Nonaka, T., Iwatsubo, T. & Hasegawa, M. Ubiquitination of alpha-synuclein. Biochemistry 44, 361-8 (2005).
228. Ohrfelt, A. et al. Identification of novel alpha-synuclein isoforms in human brain tissue by using an online nanoLC-ESI-FTICR-MS method. Neurochem Res 36, 2029-42 (2011).
229. Kang, L. et al. N-terminal acetylation of alpha-synuclein induces increased transient helical propensity and decreased aggregation rates in the intrinsically disordered monomer. Protein Sci 21, 911-917 (2012).
230. Maltsev, A. S., Ying, J. & Bax, A. Impact of N-terminal acetylation of alpha-synuclein on its random coil and lipid binding properties. Biochemistry 51, 5004-13 (2012).
231. Biedler, J. L., Roffler-Tarlov, S., Schachner, M. & Freedman, L. S. Multiple neurotransmitter synthesis by human neuroblastoma cell lines and clones. Cancer Res 38, 3751-7 (1978).
232. Schubert, D. et al. Clonal cell lines from the rat central nervous system. Nature 249, 224-7 (1974).
233. Paris, I. et al. Copper neurotoxicity is dependent on dopamine-mediated copper uptake and one-electron reduction of aminochrome in a rat substantia nigra neuronal cell line. J Neurochem 77, 519-29 (2001).
234. Dagnino-Subiabre, A. et al. Angiotensin receptor II is present in dopaminergic cell line of rat substantia nigra and it is down regulated by aminochrome. Mol Cell Biochem 212, 131-4 (2000).
235. Heitz, F., Morris, M. C. & Divita, G. Twenty years of cell-penetrating peptides: from molecular mechanisms to therapeutics. Br J Pharmacol 157, 195-206 (2009).
236. Deshayes, S., Morris, M., Heitz, F. & Divita, G. Delivery of proteins and nucleic acids using a non-covalent peptide-based strategy. Adv Drug Deliv Rev 60, 537-47 (2008).
237. Maiolo, J. R., Ferrer, M. & Ottinger, E. A. Effects of cargo molecules on the cellular uptake of arginine-rich cell-penetrating peptides. Biochim Biophys Acta 1712, 161-72 (2005).
238. Guterstam, P. et al. Elucidating cell-penetrating peptide mechanisms of action for membrane interaction, cellular uptake, and translocation utilizing the hydrophobic counter-anion pyrenebutyrate. Biochim Biophys Acta 1788, 2509-17 (2009).
239. Clark, R. E. et al. Clinical use of streptolysin-O to facilitate antisense oligodeoxyribonucleotide delivery for purging autografts in chronic myeloid leukaemia. Bone Marrow Transplant 23, 1303-8 (1999).
240. Spiller, D. G., Giles, R. V., Grzybowski, J., Tidd, D. M. & Clark, R. E. Improving the intracellular delivery and molecular efficacy of antisense oligonucleotides in chronic myeloid leukemia cells: a comparison of

streptolysin-O permeabilization, electroporation, and lipophilic conjugation. Blood 91, 4738-46 (1998).
241. Walev, I. et al. Delivery of proteins into living cells by reversible membrane permeabilization with streptolysin-O. Proc Natl Acad Sci U S A 98, 3185-90 (2001).
242. Thompson, A., Halbert, S. P. & Smith, U. The toxicity of streptolysin O for beating mammalian heart cells in tissue culture. J Exp Med 131, 745-63 (1970).
243. Alouf, J. E. Streptococcal toxins (streptolysin O, streptolysin S, erythrogenic toxin). Pharmacol Ther 11, 661-717 (1980).
244. Burgess, S. E., Zhao, Y., Sen, A. & Hui, S. W. Resealing of electroporation of porcine epidermis using phospholipids and poloxamers. Int J Pharm 336, 269-75 (2007).
245. Lee, R. C., Hannig, J., Matthews, K. L., Myerov, A. & Chen, C. T. Pharmaceutical therapies for sealing of permeabilized cell membranes in electrical injuries. Ann N Y Acad Sci 888, 266-73 (1999).
246. Lee, B. R. & Kamitani, T. Improved immunodetection of endogenous alpha-synuclein. PLoS One 6, e23939 (2011).
247. Maroteaux, L. & Scheller, R. H. The rat brain synucleins; family of proteins transiently associated with neuronal membrane. Brain Res Mol Brain Res 11, 335-43 (1991).
248. McLean, P. J. & Hyman, B. T. An alternatively spliced form of rodent alpha-synuclein forms intracellular inclusions in vitro: role of the carboxy-terminus in alpha-synuclein aggregation. Neurosci Lett 323, 219-23 (2002).
249. Iwai, A. et al. The precursor protein of non-A beta component of Alzheimer's disease amyloid is a presynaptic protein of the central nervous system. Neuron 14, 467-75 (1995).
250. Huang, Z., Xu, Z., Wu, Y. & Zhou, Y. Determining nuclear localization of alpha-synuclein in mouse brains. Neuroscience 199, 318-32 (2011).
251. Shavali, S., Brown-Borg, H. M., Ebadi, M. & Porter, J. Mitochondrial localization of alpha-synuclein protein in alpha-synuclein overexpressing cells. Neurosci Lett 439, 125-8 (2008).
252. Davidson, W. S., Jonas, A., Clayton, D. F. & George, J. M. Stabilization of alpha-synuclein secondary structure upon binding to synthetic membranes. J Biol Chem 273, 9443-9 (1998).
253. Fortin, D. L. et al. Lipid rafts mediate the synaptic localization of alpha-synuclein. J Neurosci 24, 6715-23 (2004).
254. Nakamura, K. et al. Direct membrane association drives mitochondrial fission by the Parkinson disease-associated protein alpha-synuclein. J Biol Chem 286, 20710-26 (2011).
255. Ulmer, T. S. & Bax, A. Comparison of structure and dynamics of micelle-bound human alpha-synuclein and Parkinson disease variants. J Biol Chem 280, 43179-87 (2005).
256. Binolfi, A. et al. Bioinorganic Chemistry of Parkinson's Disease: Structural Determinants for the Copper-Mediated Amyloid Formation of Alpha-Synuclein. Inorganic Chemistry 49, 10668-10679 (2010).
257. Bertoncini, C. W. et al. Structural characterization of the intrinsically unfolded protein beta-synuclein, a natural negative regulator of alpha-synuclein aggregation. Journal of Molecular Biology 372, 708-722 (2007).

258. Farrow, N. A., Zhang, O., Forman-Kay, J. D. & Kay, L. E. Characterization of the backbone dynamics of folded and denatured states of an SH3 domain. Biochemistry 36, 2390-402 (1997).
259. Bussell, R., Jr. & Eliezer, D. Residual structure and dynamics in Parkinson's disease-associated mutants of alpha-synuclein. J Biol Chem 276, 45996-6003 (2001).
260. Croke, R. L., Patil, S. M., Quevreaux, J., Kendall, D. A. & Alexandrescu, A. T. NMR determination of pKa values in alpha-synuclein. Protein Sci 20, 256-69 (2011).
261. Kuwahara, T., Tonegawa, R., Ito, G., Mitani, S. & Iwatsubo, T. Phosphorylation of alpha-synuclein protein at Ser-129 reduces neuronal dysfunction by lowering its membrane binding property in Caenorhabditis elegans. J Biol Chem 287, 7098-109 (2012).
262. Chau, K. Y., Ching, H. L., Schapira, A. H. & Cooper, J. M. Relationship between alpha synuclein phosphorylation, proteasomal inhibition and cell death: relevance to Parkinson's disease pathogenesis. J Neurochem 110, 1005-13 (2009).
263. Chung, K. K. K. et al. Parkin ubiquitinates the alpha-synuclein-interacting protein, synphilin-1: implications for Lewy-body formation in Parkinson disease. Nature Medicine 7, 1144-1150 (2001).
264. Krumova, P. et al. Sumoylation inhibits alpha-synuclein aggregation and toxicity. Journal of Cell Biology 194, 49-60 (2011).
265. Zhou, W. B. et al. Methionine oxidation stabilizes non-toxic oligomers of alpha-synuclein through strengthening the auto-inhibitory intra-molecular long-range interactions. Biochimica Et Biophysica Acta-Molecular Basis of Disease 1802, 322-330 (2010).
266. Brito, J. L., Davies, F. E., Gonzalez, D. & Morgan, G. J. Streptolysin-O reversible permeabilisation is an effective method to transfect siRNAs into myeloma cells. J Immunol Methods 333, 147-55 (2008).
267. Husmann, M. et al. Elimination of a bacterial pore-forming toxin by sequential endocytosis and exocytosis. FEBS Lett 583, 337-44 (2009).
268. Golzio, M. et al. Control by osmotic pressure of voltage-induced permeabilization and gene transfer in mammalian cells. Biophys J 74, 3015-22 (1998).
269. Pucihar, G., Kotnik, T., Kanduser, M. & Miklavcic, D. The influence of medium conductivity on electropermeabilization and survival of cells in vitro. Bioelectrochemistry 54, 107-15 (2001).
270. Recchia, A. et al. Generation of a alpha-synuclein-based rat model of Parkinson's disease. Neurobiol Dis 30, 8-18 (2008).
271. Violini, S., Sharma, V., Prior, J. L., Dyszlewski, M. & Piwnica-Worms, D. Evidence for a plasma membrane-mediated permeability barrier to Tat basic domain in well-differentiated epithelial cells: lack of correlation with heparan sulfate. Biochemistry 41, 12652-61 (2002).
272. Trehin, R. et al. Cellular internalization of human calcitonin derived peptides in MDCK monolayers: a comparative study with Tat(47-57) and penetratin(43-58). Pharm Res 21, 33-42 (2004).
273. Kramer, S. D. & Wunderli-Allenspach, H. No entry for TAT(44-57) into liposomes and intact MDCK cells: novel approach to study membrane permeation of cell-penetrating peptides. Biochim Biophys Acta 1609, 161-9 (2003).

274. Koppelhus, U. et al. Cell-dependent differential cellular uptake of PNA, peptides, and PNA-peptide conjugates. Antisense Nucleic Acid Drug Dev 12, 51-63 (2002).
275. Perret, F. et al. Anionic fullerenes, calixarenes, coronenes, and pyrenes as activators of oligo/polyarginines in model membranes and live cells. J Am Chem Soc 127, 1114-5 (2005).
276. Nishihara, M. et al. Arginine magic with new counterions up the sleeve. Org Biomol Chem 3, 1659-69 (2005).
277. Liu, B. R., Huang, Y. W., Winiarz, J. G., Chiang, H. J. & Lee, H. J. Intracellular delivery of quantum dots mediated by a histidine- and arginine-rich HR9 cell-penetrating peptide through the direct membrane translocation mechanism. Biomaterials 32, 3520-37 (2011).
278. Jablonski, A. E., Kawakami, T., Ting, A. Y. & Payne, C. K. Pyrenebutyrate Leads to Cellular Binding, Not Intracellular Delivery, of Polyarginine-Quantum Dots. J Phys Chem Lett 1, 1312-1315 (2010).
279. Fu, H., Ding, J., Flutter, B. & Gao, B. Investigation of endogenous antigen processing by delivery of an intact protein into cells. J Immunol Methods 335, 90-7 (2008).
280. Lukas, J., Bartek, J. & Strauss, M. Efficient transfer of antibodies into mammalian cells by electroporation. J Immunol Methods 170, 255-9 (1994).
281. Bischofberger, M., Iacovache, I. & van der Goot, F. G. Pathogenic pore-forming proteins: function and host response. Cell Host Microbe 12, 266-75.
282. Raagel, H., Saalik, P., Hansen, M., Langel, U. & Pooga, M. CPP-protein constructs induce a population of non-acidic vesicles during trafficking through endo-lysosomal pathway. J Control Release 139, 108-17 (2009).
283. Drin, G., Cottin, S., Blanc, E., Rees, A. R. & Temsamani, J. Studies on the internalization mechanism of cationic cell-penetrating peptides. J Biol Chem 278, 31192-201 (2003).
284. Biedler, J. L., Helson, L. & Spengler, B. A. Morphology and growth, tumorigenicity, and cytogenetics of human neuroblastoma cells in continuous culture. Cancer Res 33, 2643-52 (1973).
285. Ellis, R. J. & Minton, A. P. Protein aggregation in crowded environments. Biol Chem 387, 485-97 (2006).
286. Thayanidhi, N. et al. Alpha-synuclein delays endoplasmic reticulum (ER)-to-Golgi transport in mammalian cells by antagonizing ER/Golgi SNAREs. Mol Biol Cell 21, 1850-63 (2010).
287. Cooper, A. A. et al. Alpha-synuclein blocks ER-Golgi traffic and Rab1 rescues neuron loss in Parkinson's models. Science 313, 324-8 (2006).
288. Santos, D. & Cardoso, S. M. Mitochondrial dynamics and neuronal fate in Parkinson's disease. Mitochondrion 12, 428-37 (2012).
289. Esteves, A. R., Arduino, D. M., Silva, D. F., Oliveira, C. R. & Cardoso, S. M. Mitochondrial Dysfunction: The Road to Alpha-Synuclein Oligomerization in PD. Parkinsons Dis 2011, 693761 (2011).
290. McNulty, B. C., Young, G. B. & Pielak, G. J. Macromolecular crowding in the Escherichia coli periplasm maintains alpha-synuclein disorder. J Mol Biol 355, 893-7 (2006).
291. Croke, R. L., Sallum, C. O., Watson, E., Watt, E. D. & Alexandrescu, A. T. Hydrogen exchange of monomeric alpha-synuclein shows unfolded structure

persists at physiological temperature and is independent of molecular crowding in Escherichia coli. Protein Sci 17, 1434-45 (2008).
292. Barnes, C. O., Monteith, W. B. & Pielak, G. J. Internal and global protein motion assessed with a fusion construct and in-cell NMR spectroscopy. Chembiochem 12, 390-1 (2011).
293. Wang, W. et al. A soluble alpha-synuclein construct forms a dynamic tetramer. Proc Natl Acad Sci U S A 108, 17797-802 (2011).
294. Dettmer, U., Newman, A. J., Luth, E. S., Bartels, T. & Selkoe, D. In vivo crosslinking reveals principally oligomeric forms of alpha-synuclein and beta-synuclein in neurons and non-neural cells. J Biol Chem.
295. Bartels, T., Choi, J. G. & Selkoe, D. J. alpha-Synuclein occurs physiologically as a helically folded tetramer that resists aggregation. Nature 477, 107-10 (2011).
296. Bartels, T. et al. The N-terminus of the intrinsically disordered protein alpha-synuclein triggers membrane binding and helix folding. Biophys J 99, 2116-24 (2010).
297. Bodner, C. R., Dobson, C. M. & Bax, A. Multiple tight phospholipid-binding modes of alpha-synuclein revealed by solution NMR spectroscopy. J Mol Biol 390, 775-90 (2009).
298. Jo, E., McLaurin, J., Yip, C. M., St George-Hyslop, P. & Fraser, P. E. alpha-Synuclein membrane interactions and lipid specificity. J Biol Chem 275, 34328-34 (2000).
299. Chen, R. H. et al. alpha-Synuclein membrane association is regulated by the Rab3a recycling machinery and presynaptic activity. J Biol Chem (2013).
300. Visanji, N. P. et al. Effect of Ser-129 phosphorylation on interaction of alpha-synuclein with synaptic and cellular membranes. J Biol Chem 286, 35863-73 (2011).
301. Zhou, J. et al. Changes in the solubility and phosphorylation of alpha-synuclein over the course of Parkinson's disease. Acta Neuropathol 121, 695-704 (2011).
302. Sato, H., Kato, T. & Arawaka, S. The role of Ser129 phosphorylation of alpha-synuclein in neurodegeneration of Parkinson's disease: a review of in vivo models. Rev Neurosci, 1-9 (2013).
303. McCormack, A. L., Mak, S. K. & Di Monte, D. A. Increased alpha-synuclein phosphorylation and nitration in the aging primate substantia nigra. Cell Death Dis 3, e315 (2012).
304. Seeburg, D. P., Pak, D. & Sheng, M. Polo-like kinases in the nervous system. Oncogene 24, 292-8 (2005).
305. Sato, H., Kato, T. & Arawaka, S. The role of Ser129 phosphorylation of alpha-synuclein in neurodegeneration of Parkinson's disease: a review of in vivo models. Rev Neurosci, 1-9 (2012).
306. Maltsev, A. S., Chen, J., Levine, R. L. & Bax, A. Site-Specific Interaction between alpha-Synuclein and Membranes Probed by NMR-Observed Methionine Oxidation Rates. J Am Chem Soc (2013).
307. Girotti, A. W. Lipid hydroperoxide generation, turnover, and effector action in biological systems. J Lipid Res 39, 1529-42 (1998).
308. Ruiperez, V., Darios, F. & Davletov, B. Alpha-synuclein, lipids and Parkinson's disease. Prog Lipid Res 49, 420-8 (2010).

309. Binolfi, A. et al. Interaction of alpha-synuclein with divalent metal ions reveals key differences: a link between structure, binding specificity and fibrillation enhancement. J Am Chem Soc 128, 9893-901 (2006).
310. Fernandez, C. O. et al. NMR of alpha-synuclein-polyamine complexes elucidates the mechanism and kinetics of induced aggregation. Embo J 23, 2039-46 (2004).
311. Wang, Q., Zhuravleva, A. & Gierasch, L. M. Exploring weak, transient protein--protein interactions in crowded in vivo environments by in-cell nuclear magnetic resonance spectroscopy. Biochemistry 50, 9225-36 (2011).
312. Sulzer, D. Multiple hit hypotheses for dopamine neuron loss in Parkinson's disease. Trends Neurosci 30, 244-50 (2007).
313. Chan, C. S. et al. 'Rejuvenation' protects neurons in mouse models of Parkinson's disease. Nature 447, 1081-6 (2007).
314. Li, Y. H. et al. Alpha-synuclein functions as a negative regulator for expression of tyrosine hydroxylase. Acta Neurol Belg 111, 130-5 (2011).
315. Swant, J. et al. alpha-Synuclein stimulates a dopamine transporter-dependent chloride current and modulates the activity of the transporter. J Biol Chem 286, 43933-43 (2011).
316. Oaks, A. W. & Sidhu, A. Synuclein modulation of monoamine transporters. FEBS Lett 585, 1001-6 (2012).
317. Gandhi, S. et al. Dopamine induced neurodegeneration in a PINK1 model of Parkinson's disease. PLoS One 7, e37564 (2012).
318. Munoz, P., Huenchuguala, S., Paris, I. & Segura-Aguilar, J. Dopamine oxidation and autophagy. Parkinsons Dis 2012, 920953 (2012).
319. Halliday, G. M. et al. Alpha-synuclein redistributes to neuromelanin lipid in the substantia nigra early in Parkinson's disease. Brain 128, 2654-64 (2005).
320. Pan, T., Zhu, J., Hwu, W. J. & Jankovic, J. The role of alpha-synuclein in melanin synthesis in melanoma and dopaminergic neuronal cells. PLoS One 7, e45183 (2012).
321. Iwai, A., Yoshimoto, M., Masliah, E. & Saitoh, T. Non-A beta component of Alzheimer's disease amyloid (NAC) is amyloidogenic. Biochemistry 34, 10139-45 (1995).
322. Waxman, E. A., Mazzulli, J. R. & Giasson, B. I. Characterization of hydrophobic residue requirements for alpha-synuclein fibrillization. Biochemistry 48, 9427-36 (2009).
323. Liu, Y., Qiang, M., Wei, Y. & He, R. A novel molecular mechanism for nitrated {alpha}-synuclein-induced cell death. J Mol Cell Biol 3, 239-49 (2011).
324. Zhou, W. et al. Methionine oxidation stabilizes non-toxic oligomers of alpha-synuclein through strengthening the auto-inhibitory intra-molecular long-range interactions. Biochim Biophys Acta 1802, 322-30 (2011).
325. Xiong, N. et al. Mitochondrial complex I inhibitor rotenone-induced toxicity and its potential mechanisms in Parkinson's disease models. Crit Rev Toxicol 42, 613-32.
326. Perfeito, R., Cunha-Oliveira, T. & Rego, A. C. Revisiting oxidative stress and mitochondrial dysfunction in the pathogenesis of Parkinson disease-resemblance to the effect of amphetamine drugs of abuse. Free Radic Biol Med 53, 1791-806 (2012).

327. Dasuri, K., Zhang, L. & Keller, J. N. Oxidative stress, neurodegeneration, and the balance of protein degradation and protein synthesis. Free Radic Biol Med (2012).
328. Goodwin, J., Nath, S., Engelborghs, Y. & Pountney, D. L. Raised calcium and oxidative stress cooperatively promote alpha-synuclein aggregate formation. Neurochem Int (2013).
329. Oshiro, S., Morioka, M. S. & Kikuchi, M. Dysregulation of iron metabolism in Alzheimer's disease, Parkinson's disease, and amyotrophic lateral sclerosis. Adv Pharmacol Sci 2011, 378278 (2011).
330. Cho, M. K. et al. Structural characterization of alpha-synuclein in an aggregation prone state. Protein Sci 18, 1840-6 (2009).
331. Cole, N. B., Dieuliis, D., Leo, P., Mitchell, D. C. & Nussbaum, R. L. Mitochondrial translocation of alpha-synuclein is promoted by intracellular acidification. Exp Cell Res 314, 2076-89 (2008).
332. Johnson, M., Coulton, A. T., Geeves, M. A. & Mulvihill, D. P. Targeted amino-terminal acetylation of recombinant proteins in E. coli. PLoS One 5, e15801 (2010).
333. Hoyer, W., Cherny, D., Subramaniam, V. & Jovin, T. M. Rapid self-assembly of alpha-synuclein observed by in situ atomic force microscopy. J Mol Biol 340, 127-39 (2004).
334. Kuenzel, E. A., Mulligan, J. A., Sommercorn, J. & Krebs, E. G. Substrate specificity determinants for casein kinase II as deduced from studies with synthetic peptides. J Biol Chem 262, 9136-40 (1987).
335. Dose, A., Liokatis, S., Theillet, F. X., Selenko, P. & Schwarzer, D. NMR profiling of histone deacetylase and acetyl-transferase activities in real time. ACS Chem Biol 6, 419-424 (2011).
336. Tokuyasu, K. T. Immunochemistry on ultrathin frozen sections. Histochem J 12, 381-403 (1980).
337. Kargel, E. et al. Candida maltosa NADPH-cytochrome P450 reductase: cloning of a full-length cDNA, heterologous expression in Saccharomyces cerevisiae and function of the N-terminal region for membrane anchoring and proliferation of the endoplasmic reticulum. Yeast 12, 333-48 (1996).
338. Schanda, P., Kupce, E. & Brutscher, B. SOFAST-HMQC experiments for recording two-dimensional heteronuclear correlation spectra of proteins within a few seconds. J Biomol NMR 33, 199-211 (2005).
339. Shaka, A. J., Keeler, J. & Freeman, R. Evaluation of a new broadband decoupling sequence: WALTZ-16. J. Mag. Res. 52, 335-338 (1983).
340. Dayie, K. T. & Wagner, G. Relaxation-Rate Measurements for N-15-H-1 Groups with Pulsed-Field Gradients and Preservation of Coherence Pathways. Journal of Magnetic Resonance Series A 111, 121-126 (1994).
341. Goddard, T. D. & Kneller, D. G. Sparky 3 (San Francisco: University of California). 2002.

Acknowledgements

I wish to acknowledge the great help provided by my research group.
I am particularly fortunate to be guided and work with Honor May Rose, and to be helped by Andres Binolfi and Francois Theillet with the NMR experiments.

I would like to express my deep appreciation and gratitude to my advisor Dr. Philipp Selenko for the patient guidance and mentorship he provided to me.

Finally, I would also like to thank to M., who has been there for me and gave his support and encouragement.